Western Graduate&PostdoctoralStudies

Western University
Scholarship@Western

Electronic Thesis and Dissertation Repository

6-9-2022 2:00 PM

Carbon Nanotube-based Microscale Capacitive Flow Sensors

Nathaniel Holmes, *The University of Western Ontario*

Supervisor: Boutilier, Michael, *The University of Western Ontario*

A thesis submitted in partial fulfillment of the requirements for the Master of Engineering Science degree in Mechanical and Materials Engineering

© Nathaniel Holmes 2022

Follow this and additional works at: https://ir.lib.uwo.ca/etd

 Part of the Aerodynamics and Fluid Mechanics Commons, and the Nanoscience and Nanotechnology Commons

Recommended Citation

Holmes, Nathaniel, "Carbon Nanotube-based Microscale Capacitive Flow Sensors" (2022). *Electronic Thesis and Dissertation Repository*. 8849.
https://ir.lib.uwo.ca/etd/8849

This Dissertation/Thesis is brought to you for free and open access by Scholarship@Western. It has been accepted for inclusion in Electronic Thesis and Dissertation Repository by an authorized administrator of Scholarship@Western. For more information, please contact wlswadmin@uwo.ca.

Abstract

Micro-scale flow sensors present several advantages over traditional flow sensing methods, including minimal flow disruption, high spatial resolution, and low unit cost. Many existing micro-scale thermal and piezo flow sensors struggle with temperature drift and require complicated fabrication processes. This thesis details the development of a 60 µm by 60 µm by 50 µm drag-based capacitive flow sensor constructed from vertically aligned carbon nanotube forests. The construction of a thermal chemical vapour deposition system for sensor synthesis is also detailed. Manual manipulation of the sensor with an atomic force microscope probe was found to produce a full scale signal of ∼30 fF, measured by an AD7746 integrated circuit. A flow experiment producing wall shear stresses from 1 to 95 Pa did not produce a measurable output. With more development, such a sensor would provide a low-cost, highly configurable device for all manner of flow sensing applications.

Keywords: flow sensing, capacitive flow sensor, carbon nanotube, vertically aligned carbon nanotube forest, micro-electromechanical system, chemical vapour deposition.

Summary for Lay Audience

Flow sensors measure the speed and direction of fluid movement and have a variety of important applications, such as meteorological measurements, industrial processes, and in biomedical devices. The advent of the microchip in the late 20th century heralded an era of miniaturization. Micro-scale flow sensors offer several advantages over traditional devices. Firstly, their small size means that they do not disturb the fluid flow they seek to measure. Second, their compatibility with widely available manufacturing methods used for microchip production makes them cheap to produce in large numbers. Finally, their small size means they provide flow measurements at a very precise location. Unfortunately, current micro-scale flow sensors suffer from temperature drift, and require complicated manufacturing processes, hampering widespread adoption.

This work outlines the development of a micro-scale flow sensor 60 µm by 60 µm by 50 µm in size. The flow sensor is constructed from forests of vertically aligned carbon nanotubes grown in a custom, purpose-built chemical vapour deposition system. Discrete forests form the structural components of the sensor. When fluid flows over the sensor, the drag force bends the forests over, closing the gap between them. This movement can be measured by a change in electric charge stored in adjacent structures. The signal is measured with an off-the-shelf integrated circuit used primarily in the automotive industry. The sensor was tested by physically poking the carbon nanotube forests with the probe on an atomic force microscope, and found to produce a discernible signal of $\sim$30 fF. A flow experiment that followed using a blower connected to a 16 mm by 16 mm square channel showed no signal. It is posited that a poor understanding of the stiffness of the sensor structure led to a flow experiment with insufficient flow rates to properly actuate the sensor.

While the produced flow sensor is not ready for real-world applications, this project

fulfilled its objective as a first-generation proof of concept. Sensitivity of the device may be increased in subsequent work by refining the sensor geometry, and better understanding the material properties. The resulting sensor will be simpler and cheaper than existing micro-scale flow sensing options.

Acknowledgments

I would like to express my sincere gratitude to Dr. Michael Boutilier for welcoming me to his group a year into my degree, and providing me with the support I needed to complete this work on an accelerated schedule. Without him this project would not have been possible.

I would also like to thank Mr. Tim Goldhawk and Dr. Todd Simpson for their training and support at the Western Nanofabrication facility, and to the late Yves Rambour for his work on the custom quartz sample holder.

Finally, I would like to thank my wife Hailey for her unending patience and support through the duration of this work, and to my family for their consistent words of encouragement.

Contents

List of Tables

List of Figures

List of Acronyms

ADC	analogue to digital converter.
AFM	atomic force microscope.
CMOS	complementary metal-oxide semiconductor.
CNC	computer numerical control.
CNT	carbon nanotube.
CVD	chemical vapour deposition.
EMI	electromagnetic interference.
FIFO	first in, first out.
GUI	graphical user interface.
IC	integrated circuit.
ID	inside diameter.
LCR	inductance, capacitance, resistance.
LED	light emitting diode.
MEMS	micro-electromechanical system.
MFC	mass flow controller.
MIT	Massachusetts Institute of Technology.
MWCNT	multi-wall carbon nanotube.
PCB	printed circuit board.

PDMS	polydimethylsiloxane.
PVD	physical vapour deposition.
PVDF	polyvinyledenedifluoride.
PZT	lead zirconate titanate.
sccm	standard cubic centimetres per minute.
SEM	scanning electron microscope.
SWCNT	single-wall carbon nanotube.
TOF	time of flight.
UMS	University Machine Services.
USB	universal serial bus.
VACNTF	vertically aligned carbon nanotube forest.

List of Symbols

α	Thermal diffusivity.
δ	Deflection.
$\delta_{sublayer}$	Viscous sublayer thickness.
ϵ	Surface roughness.
ϵ_0	Permittivity of free space.
η	Blasius' self-similar variable.
μ	Dynamic viscosity.
ν	Kinematic viscosity.
ρ	Density.
σ	Normal stress.
τ_w	Wall shear stress.
ψ	Stream function.
A_c	Capacitor plate area.
AR	Aspect ratio.
A_s	Surface area.
A_w	Wetted area.
A_x	Cross-sectional flow area.
C	Capacitance.
C_d	Drag coefficient.
C_f	Skin friction drag coefficient.
c_p	Specific heat capacity.
d	Capacitor plate separation.
D	Diameter.

d_h Hydraulic diameter.

E Young's modulus or elastic modulus.

f Darcy friction factor.
F Force.
$f(\eta)$ Normalized stream function.

g Standard acceleration due to gravity.

h_{ext} External convective heat transfer coefficient.
h_f Friction head.
h_{int} Internal convective heat transfer coefficient.
h_p Pump head.
h_t Turbine head.

I Second moment of area.

k Thermal conductivity.

L Quartz rod length.

M Bending moment.
$\dot{m}$ Mass flow rate.

N_D Nusselt number.

P Pressure.
Pr Prandlt number.

r Radius.
Ra_D Rayleigh number for internal flows.
Re_D Reynolds number for internal flows.

s_g Sensor element gap.

s_h	Sensor height.
s_t	Sensor sensing element thickness.
s_w	Sensor sensing element width.
ΔT	Temperature difference.
ΔT_{lm}	Logarithmic mean temperature difference.
T_f	Film temperature.
T_i	Inlet temperature.
T_∞	Ambient temperature.
T_{lm}	Logarithmic mean temperature.
T_o	Oulet temperature.
u	Horizontal velocity component.
U	Free stream velocity.
u_*	Friction velocity.
u_{avg}	Bulk flow velocity for internal flow.
$\overline{U}$	Overall heat transfer coefficient.
v	Vertical velocity component.
$\dot{V}$	Volume flow rate.
w	Flow channel width.
x	Cartesian coordinate.
x_s	Sensor leading edge offset.
y	Cartesian coordinate.
z	Cartesian coordinate.

Chapter 1

Introduction

Flow sensors measure the speed and direction of fluid movement, and are used in the measurement of flow rates, the determination of flow patterns and the evaluation of fluid properties. Flow sensing has innumerable applications, with examples in industrial process control, environmental monitoring, and the regulation of biological systems.

With burgeoning research into micro-electromechanical system (MEMS) devices and micro- and nanofluidics, micro-scale flow sensors have received increasing attention over the last two decades [1]. Such sensors are required for measuring the extremely small fluid flows in micro-fluidic systems. The variety of potential applications for flow sensing in micro-fluidic systems is broad, but the biomedical field hosts some particularly intriguing applications, where such devices may enable precise pharmaceutical dosing, "lab on a chip" diagnostic systems [2] and even be integrated into medical implants [3].

The benefits of micro-scale flow sensors extend beyond the nano- and micro-scale to measuring macroscopic flows. Micro-scale sensors present a number of advantages over traditional flow sensing devices, namely low-cost, high spatial resolution, and minimal disruption to fluid flow [1]. The merits of micro-scale flow sensors for measuring macroscopic flows are evidenced by the natural world, where Mexican blind fish use specialized organs to measure flow for navigation [4], caterpillars use flow sensitive hairs to detect and evade predatory wasps [5], and bats monitor the flow conditions around their wings with arrays of purpose-built hairs [6].

The majority of micro-scale flow sensors that have been developed are thermal

flow sensors, or strain based sensors using piezoresistive or piezoelectric materials [1]. Thermal and piezo flow sensors suffer from an undesirable dependence on fluid temperature [7], and often require complex fabrication processes. In general, capacitive flow sensors exhibit a weaker temperature dependence, making them an attractive transduction mechanism for micro-scale flow sensing research.

Dr. Michael Boutilier is to be credited with the inspiration for this work. During his time working in the Mechanosynthesis Group at the Massachusetts Institute of Technology (MIT), he worked with patterned vertically aligned carbon nanotube forests (VACNTFs), exploring applications in electroadhesion and micro-scale printing. After working with individually electronically addressable VACNTFs, Dr. Boutilier recognized the potential for these structures as electrodes for a capacitive micro-scale flow sensor. The primary advantage of such a device would be reduced complexity of synthesis by employing well established photolithography techniques to produce the catalyst patterns from which the VACNTFs grow.

The objective of this work was to develop a first-generation micro-scale capacitive flow sensor constructed from patterned VACNTFs. Chapter 2 presents a detailed literature review on the topics of micro-scale flow sensing and VACNTFs. Chapter 3 presents the design, construction and testing of a thermal chemical vapour deposition (CVD) system for carbon nanotube (CNT) synthesis. Chapter 4 details the design and fabrication of the micro-scale flow sensors. Chapter 5 covers the testing and characterization of the produced sensor. Chapter 6 summarizes the experimental results and suggests promising avenues for future work.

Chapter 2

Literature Review

2.1 MEMS Flow Sensors

2.1.1 Thermal Flow Sensors

Of the different categories of MEMS flow sensors, thermal flow sensors are the most studied, accounting for approximately 50% of research [1]. Thermal flow sensors are uniquely suited to micro-scale devices, as the large surface area to volume ratio results in rapid heat transfer and short equilibration times. MEMS thermal flow sensors are further categorized by their physical configuration. Common configurations include hot wire sensors, hot film sensors, calorimetric sensors and time of flight (TOF) sensors. MEMS thermal flow sensors may also be characterized by the temperature transduction mechanism [8]. Categories include thermoresistive, thermoelectric and thermoelectronic, where the temperature transduction is through a change in resistance, a produced voltage, and a change in the forward bias voltage respectively.

Thermal hot wire sensors measure the convective heat transfer from a heated wire suspended in the working fluid and use it to deduce information about the fluid flow. Thermal hot film sensors differ only in geometry, heating a film rather than a wire. Hot wire/film sensors may use constant current heating and measure the temperature change, or they may control the heating power to maintain a constant temperature. Both schemes take advantage of the temperature dependence of the the resistivity of the hot wire material, measuring and controlling the applied

voltage to achieve the desired function [9]. Some of the earliest work on MEMS thermal hot wire/film sensors was by van Oudheusden et al. who used a thermally isolated floating silicon membrane, electrically heated to 17 K above ambient temperature. The flow velocity magnitude and direction could be calculated with temperature measurements from eight thermocouples situated around the membrane perimeter [10]. Silicon based MEMS thin film thermal sensors continue to be an active area of research for their ease of fabrication, mechanical robustness, temperature and chemical resistance, and simple operation [11].

As an interesting recent example of a MEMS hot wire flow sensor, Sadeghi et al. used a commercially available wire bonding machine for integrated circuit manufacturing to create loops of wire for the sensor [12]. Aluminum and platinum wires were tested and showed very good accuracy (0.06% for the platinum wire at low flow velocities). Hot wire sensors featuring freely suspended wires offer good heating uniformity due to the thermal isolation from the substrate, but are inherently fragile. Various techniques for simultaneous thermal isolation and physical stabilization have recently been investigated, with most involving embedding the wires in an insulating material on the substrate [8].

Thermal calorimetric flow sensors measure the temperature of the working fluid around a heating element, rather than monitoring the temperature or power to the heating element itself. Calorimetric flow sensors generally show better performance than hot wire/film sensors at low flow velocities, but tend to saturate at higher flow velocities [13]. Some of the earliest work with MEMS calorimetric flow sensors focused on bio-medical applications where the sensitivity at low flow rates was desirable. Ernst et al. demonstrated sensitivity down to $100\,\mathrm{nL\,h^{-1}}$ in a 1 mm by 100 µm channel with a sensor deposited on a silicon nitride membrane covered in a 700 nm nitride layer [14]. Later work focused on miniaturisation of the technique, achieving stability down to flow rates of $40\,\mathrm{nL\,min^{-1}}$ in a channel with a 15 µm by 80 µm cross-section [15].

Recent studies have looked to combine the unique advantages of hot wire flow sensors with those of calorimetric flow sensors [16]. Ahmed et al. developed a hybrid “system on chip" thermoresisitive micro-calorimetric flow sensor that uses hot-wire thermal transduction at high flow velocities, and calorimetric measurements at low flow velocities [17]. Li et al. developed a five wire sensor using one heater wire surrounded by four sensing wires (shown in Figure 2.1) to produce a calorimetric flow sensor with directionality and low speed sensitivity [18].

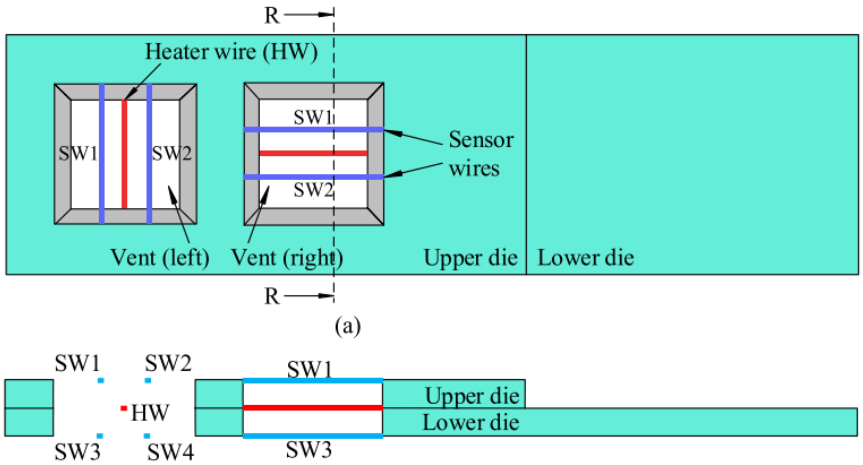

Figure 2.1: From Li et al. [18]. Four sensing wires (SW) surround one heating wire (HW) to produce a directional calorimetric flow sensor.

Thermal TOF flow sensors function by injecting a thermal tracer upstream of a temperature sensor and measuring the transit time. Thermal TOF sensors display excellent linearity, as the thermal tracer is a heated pocket of the working fluid itself, and is therefore a very direct measurement of fluid velocity. Unfortunately, these sensors are slow to respond, with response times on the order of seconds common for typical applications [19]. These sensors also exhibit a weak dependency on the specific heat capacity of the working fluid, and generally struggle to achieve good sensitivity and accuracy [19]. At extremely low flow rates, more complex thermal models are required to account for thermal diffusion [20]. The thermal TOF technique is uniquely suited to micro-scale devices, as the small transit distance and fast thermal dynamics speed up the system response.

2.1.2 Piezoresistive Flow Sensors

Flow sensors operating on the piezoresistive principle are the second most commonly studied MEMS flow sensor [1]. These flow sensors are often categorized based on their physical structure, with cantilever and diaphragm being the most common forms. Piezoresistivity is a material property defined by a change in resistivity when strained.

Many diaphragm MEMS flow sensors are inspired by biological structures, the inner ear hairs and lateral lines on fish being notable examples [1]. Most diaphragm MEMS flow sensors make use of a hair-like structure connected to a diaphragm

at its base. As the flow deflects the hair, the movement is translated to the diaphragm, where any number of transduction mechanisms (including piezoresistive transduction) translate the movement into a signal [21].

Silicon is one of the most common diaphragm materials due to the plethora of compatible low-cost fabrication processes and well established techniques for creating micro-scale strain gauges. Work by Chen et al. is a good example, placing a rigid epoxy hair on a silicon paddle outfitted with a number of strain gauges [22]. This sensor exhibited a linear response down to flow velocities of $0.7\,\mathrm{mm\,s^{-1}}$ in water and displayed an angular resolution of $\sim 3^{\circ}$. Various strategies to increase the sensitivity of such a system have been tested, including encapsulation of the hair-like structure in hydrogel to increase the fluid drag acting on it [23].

Diaphragm material is not limited to silicon, and polymer diaphragm materials have been shown to provide notable advantages in terms of durability and sensitivity [24]. In 2006, Engel et al. demonstrated an artificial hair sensor made entirely from polymer materials, with a polyurethane hair and an engineered piezoresistive membrane made from polyurethane impregnated with conductive carbon [25]. More recent work using piezoresistive polymer diaphragms has taken inspiration from the canal neuromast structures in the lateral-line organs of fish [26]. Such structures effectively provide flow signal frequency filtering by surrounding the flow sensing elements with a physical structure that damps the flow before it reaches the sensor.

In one notable exception to the combined use of artificial hair cell sensors with diaphragm structures, Maschmann et al. produced a flow sensor using a glass fibre coated in CNTs and inserted into a glass micro-capillary [21]. The CNT coating is piezoresistive [27], and when fluid drag creates a bending moment in the hair, the CNT coating is compressed, changing the resistance between the capillary electrodes.

Cantilever flow sensors sense the deflection of a cantilever beam structure caused fluid drag. Early work with MEMS cantilever flow sensors by Svedin et al. used symmetric airfoil plates connected by a centre support beam [28]. Fluid flow caused deflection of the plates that was measurable with 500 nm thick polysilicon piezoresistive strain gauges. Subsequent work introduced a paddle shaped cantilever geometry with a planar sensor oriented perpendicular to the flow [29]. Five years later, Wang et al. displayed an interesting variation on the paddle shaped

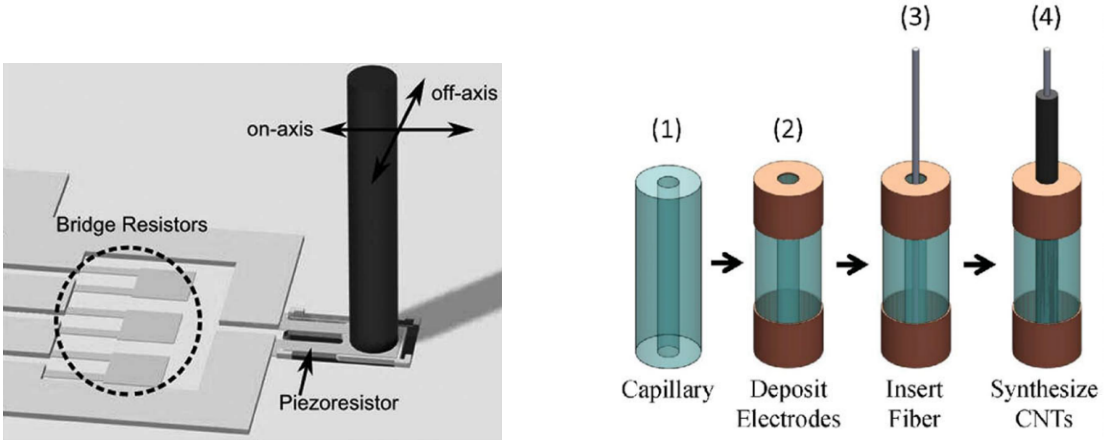

(a) (b)

Figure 2.2: Piezoresistive artificial hair cell flow sensors. *(a)*: from Chen et al. [22]. An illustration of an artificial hair cell flow sensor using a silicon diaphragm with piezoresistive transduction. *(b)*: from Maschmann et al. [21]. A glass fibre artificial hair cell flow sensor using a layer of CNTs as a piezoresistive coating to sense hair movement.

cantilever MEMS flow sensor using a nitride layer on a silicon beam [30]. Residual stress from fabrication, induced by different coefficients of thermal expansion of the constituent materials, caused the beam to bend out from the substrate surface and into the flow (shown in Figure 2.3). A platinum layer deposited on the beam served as the piezoresistive sensing element.

Recently, Tian et al. performed a study to optimize the shape of cantilever MEMS flow sensors, finding an inverted trapezoid shape (narrow at the base) to be optimal in the flow velocity range from $0.3\,\mathrm{m\,s^{-1}}$ to $3.5\,\mathrm{m\,s^{-1}}$ [32]. Another notable aspect of this study was that it used an array of eight cantilevers. Using multiple sensors operating in parallel multiplies the magnitude of the signal produced, and is one strategy to combat the problems arising from the small magnitude signals inherent to micro-scale sensing devices.

Takahashi et al. recently presented a cantilever style piezoresistive MEMS flow sensor that housed the cantilever within a tight fitting opening to operate as a differential pressure sensor [31]. The MEMS device was inspired by a pitot tube, with openings facing parallel and perpendicular to the flow. The differential pressure between the stagnation point and the side of the device is used to calculate the external flow velocity. The device stands out as a robust MEMS flow sensor owing to the protection provided by the device housing, allowing it to measure air

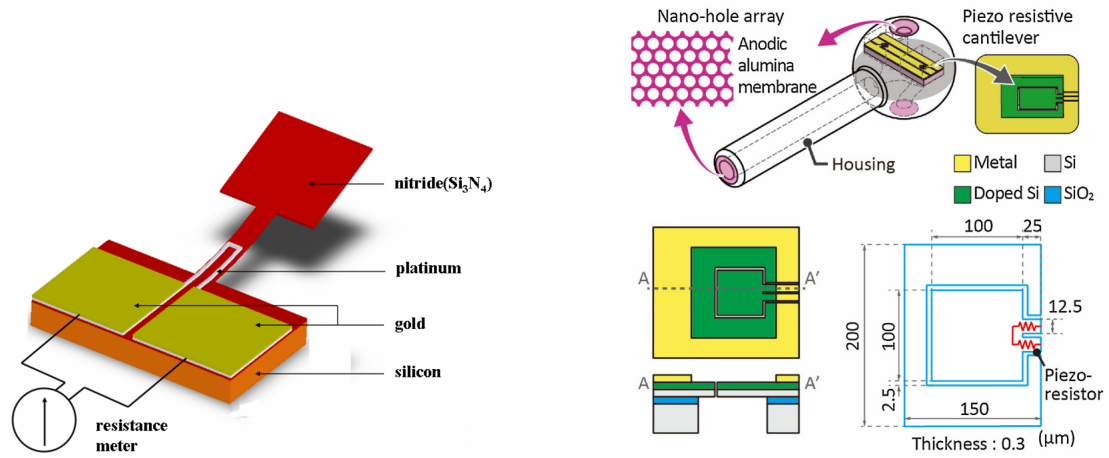

(a) (b)

Figure 2.3: Piezoresistive cantilever MEMS flow sensors. *(a)*: from Wang et al. [30]. A schematic illustration of a drag based, paddle-shaped, cantilever MEMS flow sensor using piezoresistive transduction. *(b)*: from Takahashi et al. [31]. A robust, pitot tube inspired, cantilever, piezoresistive flow sensor for measuring the airspeed of seabirds.

flows on seabirds while being impervious to submersion in sea water.

2.1.3 Piezoelectric Flow Sensors

The piezoelectric effect is the property of certain materials to develop a non-uniform surface distribution of electric charge when mechanical loads are applied. One of the biggest advantages of piezoelectric flow sensors is that this effect may be used to power the device, eliminating the need for an external power source [33]. The two most common piezoelectric materials used in MEMS flow sensors are polyvinyledenedifluoride (PVDF) and lead zirconate titanate (PZT) [1].

PVDF is a popular piezoelectric material choice for MEMS flow sensors for its low stiffness, low density and biocompatibility [34]. This makes it a good choice for medical applications, with flow sensors for veins and catheters previously studied [35, 36]. Other studies were inspired by the mechanosensor ciliary bundles of fish, using bundles of polydimethylsiloxane (PDMS) pillars connected at the tips by piezoelectric electrospun PVDF nanofibres [37]. The bundles were encapsulated in a hydrogel cupula to increase fluid drag and protect the fibres. As the bundle is deflected, the distance between the PDMS pillar tips changes, straining the

PVDF nanofibres and producing a signal. The sensor demonstrated a threshold detection limit of only $8.24\,\mu m\,s^{-1}$, which is comparable to the biological systems by which it was inspired. Below $8.24\,\mu m\,s^{-1}$, the signal becomes noisy as the output approaches the noise floor.

PZT is another common material choice for piezoelectric MEMS flow sensors due to its good piezoelectric properties and high Curie temperature [38]. Kottapelli et al. used a PZT sensing base for a piezoelectric flow sensor inspired by the whiskers of harbor seals [39]. The device featured a micro-whisker with a unique elliptical cross-section fabricated by stereolithography. Experiments showed a reduction in vortex induced vibrations when compared to a cylindrical whisker, while maintaining sensitivity to lower frequency flow signals of interest.

While less common, piezoelectric MEMS flow sensors based on other materials have also been explored. One notable example uses a novel operating principle whereby a metallic post transmits fluid drag forces through a two-stage micro-lever mechanism acting on a pair of resonators to shift their natural frequency [40]. The micro lever mechanism was fabricated by lithographic patterning and deep reactive ion etching. The resultant sensor showed a sensitivity of $5.26\,Hz\,m^{-2}\,s^{2}$ across a range of $\pm 8\,m\,s^{-1}$.

2.1.4 Capacitive Flow Sensors

MEMS flow sensors operating using capacitive transduction are of particular interest in this review. Capacitive transduction was the principle envisioned in the initial project concept due to its compatibility with the physical operating mechanism of variable spacing of adjacent, electrically isolated structures. Advantages of capacitive flow sensors include better temperature independence when compared to piezo materials, and no need to heat potentially sensitive process gases as is the case with thermal sensors [41]. The development of micro-scale capacitive flow sensors can be traced back to work on capacitive pressure sensors in the 1970s. At this time there was a need for a capacitive pressure transducer due to the susceptibility of then current piezoresistive devices to sensor drift due to temperature changes [42]. A silicon device developed by Sander et al. was millimeter scale and tested from 0 to 40 kPa, producing a 4 pF full-scale output measured by a custom, on-chip, Schmitt trigger type oscillator.

Silicon-based capacitive pressure transducers continued to be studied through the 1980s before being adapted for flow sensing [43]. In 1992, Cho et al. sought to measure process gas flows less than 1 standard cubic centimetres per minute (sccm) with a capacitive MEMS flow sensor [41]. The produced sensor used a 2 mm by 2 mm by 3 µm thick silicon membrane connected to a micro-machined flow channel to measure the pressure differential between the inlet and outlet. The sensor exhibited a resolution of 0.1 Pa and a capacitance change of 1 pF was measured with an inductance, capacitance, resistance (LCR) meter over a 107 Pa pressure range.

Many early capacitive MEMS flow sensors continued to rely on the measurement of a pressure differential to deduce flow characteristics. Inspired by the Prandtl tube, Berberig et al. designed one of the first capacitive MEMS devices intended to measure flow in a free stream [44]. The device featured a wet etched silicon structure and a thin silicon membrane. Membrane movement due to the differential pressure between the stagnation point ahead of the sensor and the static pressure on the side of the device moved the capacitor's detection electrode to generate a signal. The device used a diode-quad bridge circuit inspired by the work of Harrison et al. to measure the capacitance signal [45]. The circuit sensitivity was $6.8\,\mathrm{V\,pF^{-1}}$, and the sensor produced a 0.1 V signal at $22\,\mathrm{m\,s^{-1}}$.

Jang et al. developed a capacitive flow sensor intended to more accurately measure microscale flows [46]. The sensor used two 30 µm thick, 1.5 mm square silicon membrane capacitive pressure transducers to measure the pressure differential across a 5.7 mm long channel fabricated by wet etching. Unique to this sensor was the attention to developing a straight, smooth flow channel. Such a channel makes it easier to analyse microscale flow behaviours by accounting for the slip that occurs at gas-solid interfaces at this scale. The sensor produced a capacitance signal of 5 pF for a mass flow rate of $4 \times 10^{-10}\,\mathrm{kg\,s^{-1}}$.

Van Baar et al. were some of the earliest to experiment with drag based capacitance MEMS flow sensors [47]. Nitride and SU-8 photoresist hair-like structures were fabricated using a sacrificial silicon moulding process and standard photolithography techniques respectively. The hair-like structures were up to 0.5 mm tall and fixed at their base to a mobile silicon-rich nitride membrane. Using an impedance analyzer, the full scale capacitance signal was found to be 0.8 pF. Flow testing used oscillatory acoustic flows at frequencies up to 100 Hz and the signal found to be comparable to that produced by a microflown.

As an example of a flow sensor utilizing a less common flow sensing mechanism, Haneveld et al. developed a microscale Coriolis mass flow sensor with capacitive readout [48]. Coriolis flow meters are typically reserved for measuring flows at a larger scale due to the inherent difficulty measuring the weak Coriolis force, however the combination of a flexible silicon nitride tube for the sensor and a unique comb-like capacitive transducer yielded success. The capacitive sensor used two meshing comb-like silicon structures whereby the capacitance was reduced when they were separated out of plane. The capacitance signal was measured by energizing the electrodes with a 1.4 MHz signal and monitoring the amplitude of a 1.4 MHz output from connected charge amplifiers. The sensor demonstrated excellent linearity and an error of 2% of full-scale.

André et al. present an interesting integrated complementary metal-oxide semiconductor (CMOS) circuit and MEMS with their out of plane cantilever flow sensor [49] (shown in Figure 2.4). The sensor consisted of SiO_2/Al bilayer cantilevers 1.15 µm thick, 100-200 µm long and 10-30 µm wide. Residual stresses in the bilayer cantilevers from different thermal expansion coefficients and the high temperature synthesis processes bend the cantilevers up out of plane and into the flow. The simulated capacitance change for a sensor with 20 interwoven fingers in a $120\,\mathrm{m\,s^{-1}}$ flow was ∼30 fF. The capacitance signal was read with an integrated CMOS circuit comprised of a five stage ring capacitance to frequency converter oscillator. The sensor output was highly non-linear due to the inherent non-linearity of the beam deflection sensing mechanism. At the full scale flow velocity of $120\,\mathrm{m\,s^{-1}}$, the oscillation frequency was reduced by $\sim 10\%$ from the baseline no-flow value.

A significant disadvantage of the bilayer out of plane cantilever design [30, 49], is the susceptibility to temperature induced drift. Nguyen et al. set out to address the issue of temperature drift while reducing cost with a design for a capacitive MEMS drag-based paddle flow sensor. The in-plane sensor consisted of an interdigiated comb structure with 282 fingers 10 µm wide and spaced 10 µm apart. Drag acts on a 2 mm by 4 mm cantilevered paddle that flexes the capacitor comb structure, producing a capacitance change of 2 pF at a velocity of $19\,\mathrm{m\,s^{-1}}$. The sensor output temperature drift was measured to be less than 0.5 % with a 20 °C temperature change. In this experiment the capacitance measurements were taken with a precision LCR meter, however the authors suggest that an Analog Devices 7747 integrated circuit could be used for practical applications due to its low cost and suitable measurement range.

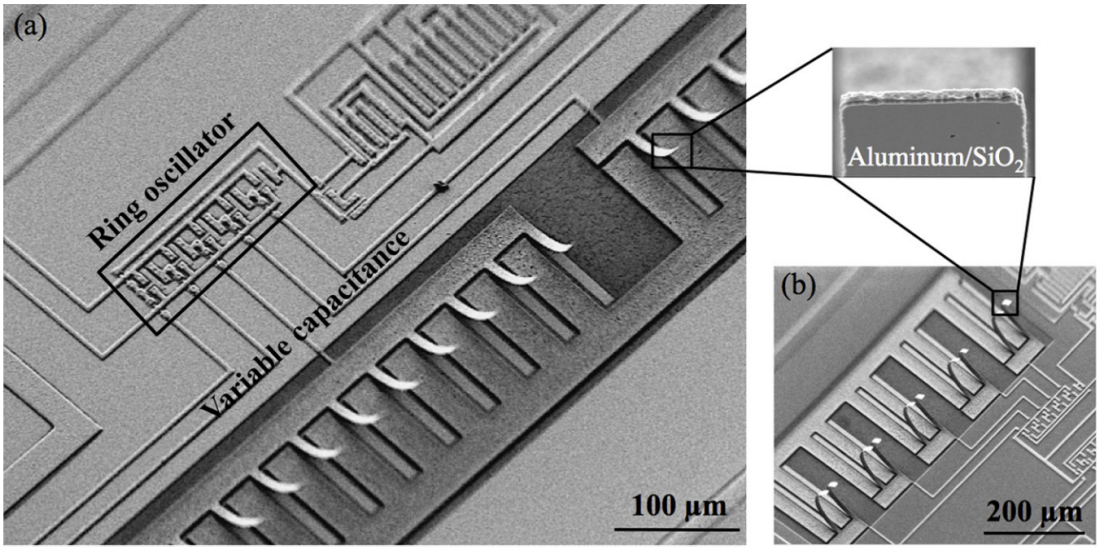

Figure 2.4: From André et al. [49]. Out-of-plane cantilever MEMS flow sensor using capacitive transduction.

2.2 Carbon Nanotubes

2.2.1 Synthesis and Characterization

Hollow carbon filaments with nano-scale diameter (carbon nanotubes) were discovered by Radushkevich and Lukyanovich in 1952 [50, 51]. Early experiments in the late 1950s used diffraction studies to characterize the structure of CNTs [52] with later experiments laying to rest debates about the structure once TEMs were able to resolve the structure fully [53]. In 1991, Iijima published his seminal paper *Helical Microtubules of Graphitic Carbon* [54] which launched an intense research interest in carbon nanotubes and nanotechnology over the following decades.

Early work with CNTs focused on the relationship between morphology and the synthesis route. Multi-wall carbon nanotubes (MWCNTs), that is CNTs made with multiple layers of concentric graphene shells, were the first to be discovered [50, 51]. Single-wall carbon nanotubes (SWCNTs) were observed much later during experimentation incorporating transition metals into MWCNTs [55, 56]. The geometry of a SWCNT is described by the chiral vector (C_h, shown in Figure 2.5). The chiral vector is defined as the traversal across an unrolled SWCNT (a graphene sheet) between crystallographically equivalent sites and is described by the equation $C_h = na_1 + ma_2$, where a_1 and a_2 are basis vectors for the hexagonal lattice and n and m are integer coefficients [57]. In this way, the morphology of

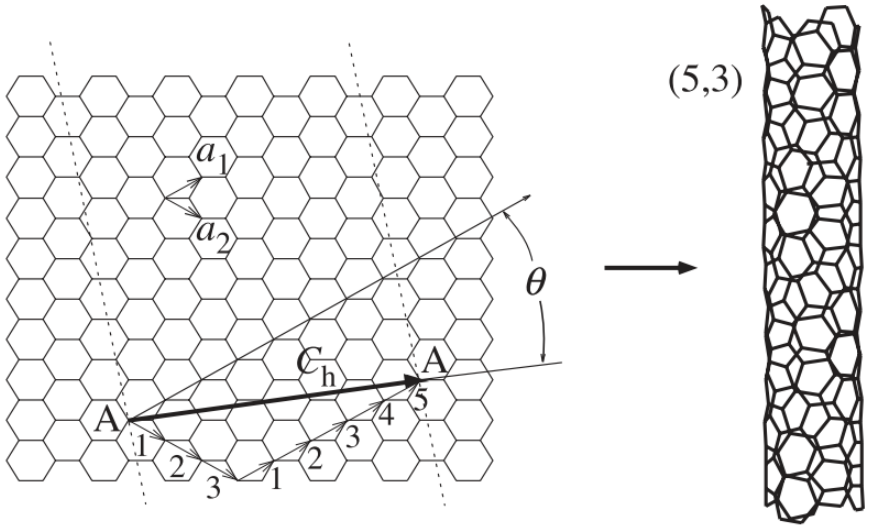

Figure 2.5: From Dresselhaus et al. [57]. Schematic showing how CNT morphology is described by the the chiral vector C_h, composed from the the basis vectors a_1 and a_2.

SWCNTs is entirely described by the integer pair (n, m).

Arc-discharge, laser ablation, and CVD are the primary methods for CNT synthesis. In the arc-discharge synthesis process, high currents are passed through a pair of separated carbon electrodes [58]. The arc that forms ignites a plasma of helium gas, evaporating the carbon atoms from the electrodes and depositing them in CNT form. The arc-discharge process creates mostly MWCNTs, however SWCNTs may also be synthesized by the introduction of a metal catalyst (such as cobalt) into the electrodes [56]. Laser ablation operates on a similar principle to the arc-discharge process, but uses a high intensity laser to ablate a carbon target. The target may be doped with a catalyst such as cobalt or nickel to affect the morphology of the produced CNTs [59]. Arc-discharge and laser ablation techniques tend to produce highly crystalline CNTs with few defects in a tangled bundle [60].

The CVD CNT growth process uses a hydrocarbon gas as the carbon source rather than a solid carbon source. The gas flows over a transition metal catalyst (often iron, cobalt or nickel) at high temperature (generally 550 °C-750 °C) where the hydrocarbon dissociates and carbon enters into solution in the catalyst nanoparticles [58]. When the catalyst particle becomes saturated, the carbon begins to precipitate out, growing a CNT. CVD grown MWCNTs tend to have much higher defect densities, as the lower synthesis temperature does not provide enough energy for

the CNTs to anneal into a fully crystalline form. CVD growth produces aligned arrays of CNTs, and was the method used to grow some of the longest CNTs [61, 62].

The carbon-carbon bond in a graphene layer is one of the strongest known chemical bonds [57]. As low-density, fibre-like nano-structures composed of rolled-up sheets of graphene, CNTs are thus uniquely suited to synthetic materials and composites stronger and lighter than ever before. The study of the mechanical properties of CNTs is therefore very valuable. Due to their tubular structure, CNTs are highly anisotropic. Their high aspect ratio fibre-like form makes the elastic modulus and the tensile strength along the longitudinal axis the most relevant mechanical properties. Table 2.1 shows a summary of experimental measurements of the Young's modulus of individual CNTs. The values exhibit a large range, which Shokrieh et al. attribute to a lack of direct measurement techniques at the nanometer scale, limitations on specimen size, and inadequate control over the alignment and distribution of nanotubes [63]. More recent bending tests that used more direct measurements and exhibited smaller uncertainties place the elastic modulus around 1 TPa [64, 65, 66].

Note that many of these studies focused on defect-free crystalline specimens formed with laser ablative or arc-discharge processes. The Young's modulus may be dramatically reduced by defects in the CNT structure. Salvetat et al. found Young's moduli ranging from 10-50 GPa for CNTs synthesized using a CVD process [64].

Yu et al. conducted a series of tensile tests by attaching opposite ends of CNTs to atomic force microscope (AFM) probe tips to determine tensile strength. They found that MWCNTs break at the external shell, with inner layers being drawn out like a sword from its sheath [65]. The tensile strength was found to lie between 11 and 62 GPa. For SWCNTs, the tensile strength was found to be between 13 and 52 GPa [67].

Due to their well defined structure, CNTs are uniquely suited to an analytical estimation of their material properties. To this end, atomistic modelling [71], analytical continuum mechanics [72] and numerical continuum mechanics approaches [73] have all been employed. Atomistic modelling methods use detailed models that are computationally intense to solve, and thus are limited to small length and time scales. Continuum models use simplified approaches developed for continuum mechanics analyses on larger scales and caution must be used when applying the

Table 2.1: Summary of experimental results from the mechanical testing of SWCNTs [63].

Year	**Method**	**Elastic Modulus** (TPa)	**Source**
1996	Thermal vibrations - TEM	0.4-4.15	[68]
1998	Thermal vibrations - TEM	0.9-1.7	[69]
1998	Cooling induced vibrations, micro-Raman spectroscopy	2.8-3.6	[70]
1999	Both ends clamped - AFM	0.8 ± 0.41	[64]
2000	Tensile test - AFM	1.002	[65]
2000	3-point bending - AFM	1.2	[66]

same assumptions to nanostructures [63]. As an example, a challenge with continuum models is the somewhat arbitrary definition of an equivalent continuum thickness. With SWCNTs especially, the tube wall is only a single atom thick, and the dimension of a carbon atom is neither clear or meaningful when applied to a continuum mechanics models. In this case, the commonly used value is the interplanar spacing of graphene sheets of 0.34 nm [63], although some studies have used values as large as 0.68 nm [74]. Results for the elastic modulus of CNTs in the axial direction from all methods of modelling generally fall within the range of 0.5-1.5 TPa, showing reasonably good agreement with experimental results.

Early theoretical calculations suggested that the electronic properties of CNTs were highly sensitive to the CNT morphology [75], spurring extensive research on the subject. CNTs fall into three categories based on their band gap energy: zero gap, tiny gap, and large gap [57]. As a general rule, CNTs with a (n, n) structure or a (n, m) structure satisfying $n - m = 3j$, where j is a non-zero integer, may be considered metals at room temperature, while most others are semi-conducting. On the extreme end of the spectrum Tang et al. demonstrated small diameter SWCNTs (0.4 nm) that exhibit superconductivity [76]. Later, low-temperature scanning tunneling microscopy experiments by Odom et al. and Wildöer et al. measured the electronic properties of CNTs and found the results to align well with theoretical predictions relating morphology and electronic properties [77, 78].

The relevance of the electronic properties of CNTs to the proposed sensor concept that uses VACNTFs as bulk material for capacitor electrodes is limited mainly to the electrical conductivity. Having established adequate conductivity among "metallic" CNTs, and with a number of previous experiments using VACNTFs for

this exact purpose [79, 80, 81], we can be satisfied that VACNTFs will work as capacitor electrodes in the proposed sensor. Worth noting is that many studies have investigated CNTs as electrode materials for supercapacitors, however most of these studies focus on electrolytic capacitors where the electrodes are flooded with electrolyte and the large surface area of the CNT material greatly improves the charge and discharge rate [82, 83]. When used as a bulk electrode material in a micro-scale parallel plate capacitor with an air gap, the increased surface area yields no appreciable benefit.

While relatively little research has been done on the thermal properties of CNTs, a study by Maniwa et al. highlights the potential for the small axial thermal expansion coefficient of CNTs to be an advantage of a CNT flow sensor [84]. Studies such as one by André et al. [49], highlight the challenge of drift with temperature in capacitive flow sensors due to thermal expansion. Maniwa et al. measured the axial (in-plane) coefficient of thermal expansion for CNTs to be $(-0.15 \pm 0.20) \times 10^{-5}\,\mathrm{K}^{-1}$ and the radial (inter-planer) coefficient of thermal expansion to be $(0.75 \pm 0.25) \times 10^{-5}\,\mathrm{K}^{-1}$ [84].

2.2.2 Vertically Aligned Carbon Nanotube Forests

Early CNT synthesis used mainly arc-discharge and laser ablative processes that created dense mats of randomly oriented CNTs. Initial work using a CVD process to synthesize CNTs used a carbon black substrate covered with transition metal nanoparticle catalyst, and also yielded tangled mats of CNTs [85]. Li et al. were the first to demonstrate a process for the large-scale synthesis of aligned CNTs [86], using a CVD process with iron nanoparticles embedded in mesoporous silica as a catalyst. They posited that the pores acted as a template to guide the aligned growth. Later experiments revealed that alignment at the start of CVD growth on a flat substrate was very poor, but that as the forest grew, the steric impediment from neighbouring CNTs forced aligned growth [87, 88]. This poor alignment during early growth leaves a "crust" of tangled CNTs on the top surface of the forest. Van der Waals forces help to maintain tight, aligned packing in CNT bundles, even after removal from the substrate [89].

Methods for the synthesis of VACNTFs can be broadly classed into single-step methods and double-step methods [90]. Single-step methods do not deposit a catalyst prior to growth, and therefore generally have less control over the entire

process. Single-step synthesis methods include thermal pyrolysis and flame synthesis. Thermal pyrolysis is a CVD process that uses an organometallic precursor such as ferrocene to supply the transition metal catalyst [88]. A two-furnace system may be used, where catalyst deposition occurs in an initial, low-temperature furnace and CNT growth occurs in a second, high temperature furnace. A single-furnace setup requires only one furnace held at a sufficiently high temperature to initiate CNT growth. Flame synthesis is unique as a non-CVD process capable of producing VACNTFs. Flame synthesis uses the direct combustion of a hydrocarbon in the presence of an oxidizer [90], growing CNTs directly on a transition metal alloy substrate [91]. Flame synthesis is attractive for commercial CNT production for its simple implementation, and energy efficiency due to the fuel acting as a source of both heat and carbon. Unfortunately, the flame synthesis process is difficult to control and produces VACNTFs that are less straight, more contaminated, shorter, and generally of lower quality than those synthesized with CVD processes [90].

Double-step VACNTF synthesis routes rely on an initial catalyst deposition step prior to CNT growth. While the extra step adds time and complexity to VACNTF synthesis, the benefit is more precise control over the catalyst composition and spatial distribution. The catalyst is frequently deposited using either a physical vapour deposition (PVD) process, or by a solution-based catalyst. PVD processes provide the benefit of precise control over catalyst thickness, which has been shown to affect the size and density of the catalyst nanoparticles produced during annealing [92]. The size and density of the catalyst nanoparticles in turn affects the CNT growth and properties, meaning control of the catalyst thickness is an indirect means of control over the synthesized VACNTF morphology. Zhao et al. have found the optimal catalyst thickness to be less than 5 nm [93]. Solution based methods for catalyst deposition use an alcoholic solution of metal salts. The solution may be dip coated, spin coated, spray coated or printed onto the substrate [90]. As the alcohol evaporates, the metal catalyst precipitates onto the substrate. In a similar manner to PVD catalyst deposition, the catalyst nanoparticle morphology and distribution may be controlled via the metal salt concentration and the coating thickness [94]. The most common catalysts for CNT growth are iron, cobalt and nickel [90], however Yuan et al. have shown aligned CNT growth using platinum, palladium, manganese, molybdenum, chromium, tin, and gold catalysts [95].

The second step of the double-step VACNTF synthesis processes is CNT growth by CVD. Thermal CVD, hot-filament CVD, and plasma-enhanced CVD have all been used for CNT synthesis [90]. Plasma-enhanced CVD yields better aligned CNTs due to the bias applied to the sample [96], and lowers the required reaction temperature by lowering the activation energy [97]. While it often produces better results, the more sophisticated equipment and conditions required make plasma-enhanced CVD synthesis of VACNTFs less common.

Early efforts to synthesize VACNTFs with a thermal CVD process struggled to grow tall arrays. In 2004, Hata et al. made a breakthrough when they discovered that the inclusion of a weak oxidizer significantly increased the CNT growth rate, growing a VACNTF 2.5 mm tall [98]. Later work showed that the dominant factor determining catalyst lifetime, and thus CNT length, was the rate of deposition of amorphous carbon on the catalyst nanoparticles. The presence of an oxidizer (in most cases water vapour) prevents this deposition and extends catalyst life [99]. Work by Futaba et al. showed that the optimal water/ethylene ratio for long CNT growth is 1/1000 [100]. Work to achieve the tallest VACNTF growth has been ongoing ever since, with the current record set by Sugime et al. sitting around 14 cm [62]. For this record growth, the group used a cold-gas CVD method where the substrate/catalyst was heated directly to reduce unwanted side reactions. A 0.8 nm Gd layer was sputtered between the 5 nm alumina catalyst support layer and the 2 nm Fe catalyst layer as it has been found to prevent structural change of the catalyst nanoparticles during growth, thereby significantly extending their life [101]. 0.5 vol% CO_2 was used as a an oxidant to further extend catalyst lifetime. Finally, vapours of aluminum isopropoxide ($\sim$ 0.03 ppmv) and ferrocene ($\sim$ 0.6 ppmv) were introduced by flowing the Ar carrier gas over powders upstream of the growth. The vapours serve to replenish Fe catalyst as it diffuses into the Al_2O_3 support material over time.

Relatively few studies have focused on the mechanical properties of VACNTFs, with research instead focusing on the more fundamental question of the mechanical properties of individual CNTs, or more commercially relevant questions such as the mechanical properties of CNT fibre bundles or CNT reinforced composite materials. Olofsson et al. were among the first to study the mechanical properties of VACNTFs [81]. They constructed a parallel plate capacitor with VACNTF electrodes synthesized on 200 nm thick molybdenum electrical traces using a thermal CVD process with a 1 nm thick Fe catalyst layer on a 5 nm thick Al_2O_3 support

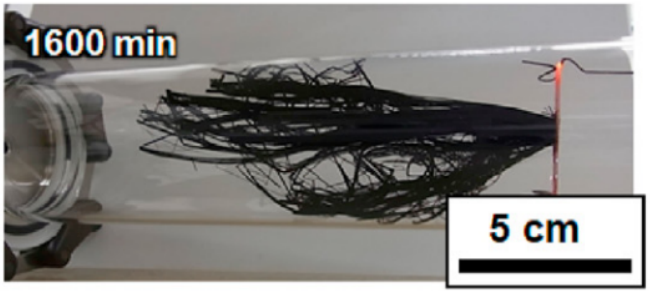

Figure 2.6: From Sugime et al. [62]. 14 cm long CNTs grown using a cold-gas CVD process with in situ supplementation of iron and aluminum.

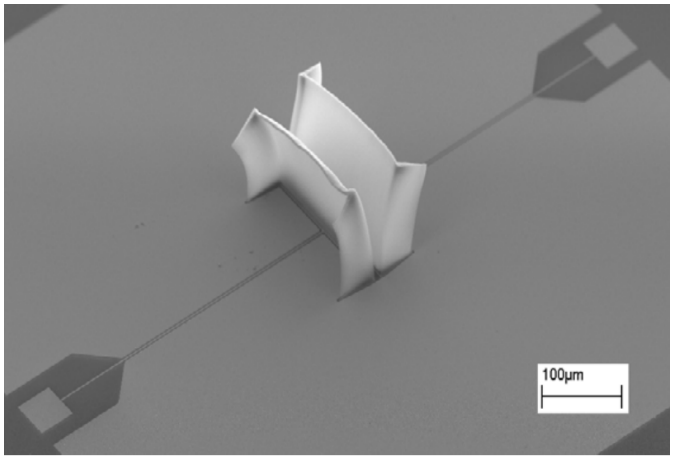

Figure 2.7: From Olofsson et al. [81]. Scanning electron microscope (SEM) image of the VACNTF capacitor electrodes. The molybdenum electrical tracing is also visible on the substrate.

layer. The VACNTFs were measured to have an area density of 10^{10} CNTs cm^{-2}. A voltage was applied to the capacitor plates, causing a build-up of charge and attractive electrostatic forces between the two. By measuring the deflection of capacitor plates using a microscope, the effective Young's modulus of the VACNTF was calculated to be in the range of 1-10 MPa.

Later work by Arun et al. measured the Young's modulus of VACNTFs as they sought to synthesize tunable MEMS capacitors using VACNTF electrodes [80]. 100 nm thick TiN tracing was used for making electrical connection to the VACNTFs, and the catalyst was a 1 nm layer of Fe on a 7 nm thick aluminum support layer. Using pull-in voltage, defined as the voltage at which point the capacitor plates collapse in and contact one another, Arun et al. estimated the effective Young's modulus of the VACNTFs to be in the range of 30-100 MPa. They justified the higher Young's modulus with the larger CNT density of 2×10^{11} CNTs

cm^{-2}, measured by counting CNTs in SEM imaging.

Using a very different technique, Hassan et al. measured the Young's modulus of a VACNTF by bending a cantilever beam comprised of CNTs aligned transverse to the beam's long axis [102]. A 1 mm tall VACNTF was first grown using a thermal CVD process with ethylene feedstock on a silicon substrate with a 1 nm Fe catalyst layer on a 10 nm thick Al_2O_3 support. A CNT micro cantilever was machined from the forest using micro-electrical discharge machining. The researchers used electrostatic actuation by a stainless-steel electrode and found the resonant frequency of the cantilever to be 7.95 kHz. From the resonant frequency, the effective Young's modulus of the VACNTF in the direction transverse to the CNT alignment was calculated to be 3.8 MPa.

A variety of studies have demonstrated potential applications for VACNTFs. Copic et al. demonstrated how VACNTF pillars could be densified by saturating the structure with solvent and allowing the capillary forces to densify the structure as the solvent evaporates [103]. The densified CNT structures were then used to create a PDMS master mold, and replicas were cast from SU-8 photoresist. DeVolder et al. showed how the growth rate of VACNTFs could be affected by the material beneath the catalyst layer, and how this could be exploited to grow a pattern of curved VACNTFs pillars to act as a hydrophobic coating [104]. Work by Kim et al. demonstrated how patterned VACNTFs coated with an atomic layer deposited Al_2O_3 insulating coating, and electronically addressable by conductive TiN traces, could be used for micro and nanotransfer printing [105, 106]. The team demonstrated the efficacy of their soft nanocomposite electroadhesives with a "pick and place" demonstration with a micro-LED of the kind found in electronic device screens.

2.2.3 Carbon Nanotube Based Flow Sensors

There have been many reports of CNTs used in flow sensing applications. Ghosh et al. were among the first to report CNT based flow sensors [107]. In their 2003 work, they observed a voltage generated by the flow of polar liquids over the surface of a SWCNT bundle oriented parallel to the flow. The sensor was exposed to laminar flows of polar liquids and found to produce a logarithmic voltage signal with sensitivity down to $1\,\mu m\,s^{-1}$. Ghosh et al. found that the response was better for more polar liquids, and that SWCNTs produced a signal ten times larger than

MWCNTs.

Bourlon et al. demonstrated a flow sensor for ionic liquids that used a single CNT oriented perpendicular to the direction of flow and embedded in the wall of a microfluidic channel [108]. The ∼2 nm diameter SWCNT acted as a nanoscale transistor, with the threshold voltage shifting with NaCl solution flow rate. This shift in threshold voltage was detectable by a change in the conductance of the CNT when a constant voltage was applied. The device was able measure a statistically significant signal at flow rates as low as $25\,\mu L\,min^{-1}$. Eight years later, Son et al. sought to improve on this work by producing a sensor that was less susceptible to the influence of substrate surface charge [109]. They produced a semi-suspended SWCNT by embedding the CNT in the wall and etching a microscale channel underneath. The device exhibited ten times the sensitivity of any previous nanoscale field effect transistor based flow sensing device.

Work by Choi and Kim made use of the electrothermal properties of CNTs to produce a wall mounted pressure and flow sensor [110]. Rectangular silicon micro-electrodes were patterned on a silicon surface and electrically isolated by a metal oxide interlayer. CNT walls were grown around each micro-electrode creating an electrical connection between the silicon substrate and the silicon micro-electrodes. A constant current was passed through the walls, heating the CNTs. The device was able to exploit the negative temperature coefficient of resistance ($-0.84\,\%\,K^{-1}$), and sense the convective cooling of the CNT walls by the change in applied voltage. The device was tested with a flow of nitrogen and produced a meaningful output across a pressure range of 3×10^{-3} to 1×10^{5} Pa, and a flow range of 1 to $52.4\,mm\,s^{-1}$.

As a more recent example of the electrothermal properties of CNTs applied to flow sensing, Nguyen et al. created a device to measure the flows in human respiration [111]. The device consisted of a VACNTF sandwiched between protective porous polyacrylonitrile films. A current was passed through the VACNTF, heating the sensor, and airflow over the sensor was measured by the change in electrical properties as the device was convectively cooled. Notable is that the device is highly flexible and robust, demonstrating the interesting applications enabled by the unique properties of VACNTFs.

A number of CNT based flow sensors have taken inspiration from nature and used CNTs as sensing elements in artificial hair flow sensors [21, 112]. In these devices,

a microfibre is coated with aligned CNT arrays. The microfibre extends from a substrate out into the fluid flow where drag forces act on it. The piezoresistive properties of aligned CNT arrays allow the bending moment created by the drag force to be sensed at the base by compression of the aligned CNT coating. Fundamental studies on the piezoresistive response of VACNTFs have shown sensitivity in the range 0.1-0.4 kPa [113]. When used in artificial hair sensors as described, the devices have shown sensitivity to flow velocities as low as $1\,\mathrm{mm\,s^{-1}}$ in air [21].

2.3 Summary

MEMS flow sensors have the potential for low-cost, high resolution, low disruption flow sensing, and are increasingly relevant with the rising prevalence of micro- and nanofluidics research. MEMS flow sensors are commonly fabricated from silicon using traditional wafer processing methods. Thermal flow sensors are among the most researched, with sensors operating on piezoresistive and piezoelectric principles being the second most common. Thermal and piezo devices suffer from sensitivity to the fluid temperature, and exhibit sensor drift as a result. Capacitive flow sensors are often less susceptible to temperature changes, and thus remain a valuable transduction mechanism for flow sensing.

CNT research exploded in the 1990s, and scientists have sought novel applications for the wonder material ever since. Characterization of individual CNTs revealed axial stiffness on the order of 1 TPa and a tensile strength of $\sim$30 GPa. Early synthesis often used arc-discharge or laser ablation processes, generating dense mats of tangled CNTs. The discovery of VACNTFs and the development of large scale CVD production processes opened the door for the use of bulk CNT material for micro-scale applications.

VACNTFs have found applications in micro-scale moulding, surface coatings, nanotransfer printing, and many others. Two-step synthesis methods with photolithographic catalyst patterning processes provide precise spatial control of VACNTF growth, and conductive tracing allows for electronically addressable CNT structures. VACNTFs have independantly been applied to MEMS capacitors and flow sensors, however this literature review found no examples of a capacitive MEMS flow sensor constructed from bulk VACNTF material.

Chapter 3

Chemical Vapour Deposition System

3.1 Design

Before the flow sensor project could begin, a CVD system for CNT synthesis needed to be constructed. The design was largely inspired by a system at the MIT [114]. This system had proven success synthesizing patterned VACNTFs, and detailed synthesis conditions for consistent results were readily available [115]. Table 3.1 lists the primary CVD control objectives for the system. Figure 3.1 shows a simplified schematic of the CVD system. A fully detailed engineering drawing is provided in Appendix A.

3.1.1 System Architecture and Component Selection

The constructed thermal CVD system provides connections for helium, hydrogen and ethylene. Two-stage pressure regulators from Praxair were selected for their

Table 3.1: CVD system control objectives. Ranges were based on recipes published by the group at MIT [115]

Parameter	**Range**	**Resolution**
Temperature	0 - 1000 °C	1 °C
Helium Flow	0 - 1000 sccm	1 sccm
Ethylene Flow	0 - 500 sccm	1 sccm
Hydrogen Flow	0 - 500 sccm	1 sccm

ability to provide a more consistent output pressure compared to a single-stage regulator. G-series mass flow controllers from MKS Instruments were selected and outfitted with a digital RS-485 serial interface for control of the process gas flow rates. Two units with a full scale flow of 500 sccm were selected for hydrogen and ethylene metering, and one unit with a full scale flow of 1000 sccm was selected for helium metering. These maximum flow rates were based on the anticipated maximum required flow rates from CVD recipes published by the MIT group [115]. Swagelok quarter-turn plug valves were installed immediately downstream of the mass flow controllers to provide options for system isolation.

The furnace is a Fisher Scientific 800 W, 25.4 mm tube furnace. The furnace features a 1100 °C maximum temperature with an RS-485 digital communications port for monitoring and control. A 610 mm long 25 mm diameter fused quartz tube fits in the furnace serving as the reaction chamber.

Connected to the exhaust side of the quartz tube is a tee allowing for an outlet for the exhaust gases and a connection for a Pfeiffer magnetically coupled rotary/linear feedthrough. The feedthrough features a 500 mm stroke, sufficient to move a sample from outside the furnace, to anywhere within the furnace. The rotary movement is undesirable, as the sample holder must remain level to prevent the samples from sliding off. Pfeiffer sells an anti-twist lock, however this ended up not being a viable option due to supply chain delays. Instead, a custom anti-twist lock was fabricated from aluminum tubing and 3D printed components. Detailed engineering drawings of the custom anti-twist lock are made available in Appendix A.

Out of the other port on the tee, the exhaust gas is transitioned into a 6.35 mm inside diameter (ID) vinyl tube routed to a 125 mL Chemglass gas wash bottle containing mineral oil. The mineral oil in the wash bottle generates a controlled amount of back pressure, and isolates the system from atmospheric gases. From the wash bottle outlet, the exhaust gas is routed through a second vinyl tube to the top of the fume hood housing the system.

Upstream from the reaction chamber, the system makes exclusive use of 6.35 mm diameter 304 stainless steel Swagelok tubing. Previous work with Teflon tubing indicated that moisture absorption and release from the polymer tubing caused inconsistent growth [115]. For the larger connections to the quartz tube and downstream from the reaction chamber, stainless steel ISO-KF vacuum flange

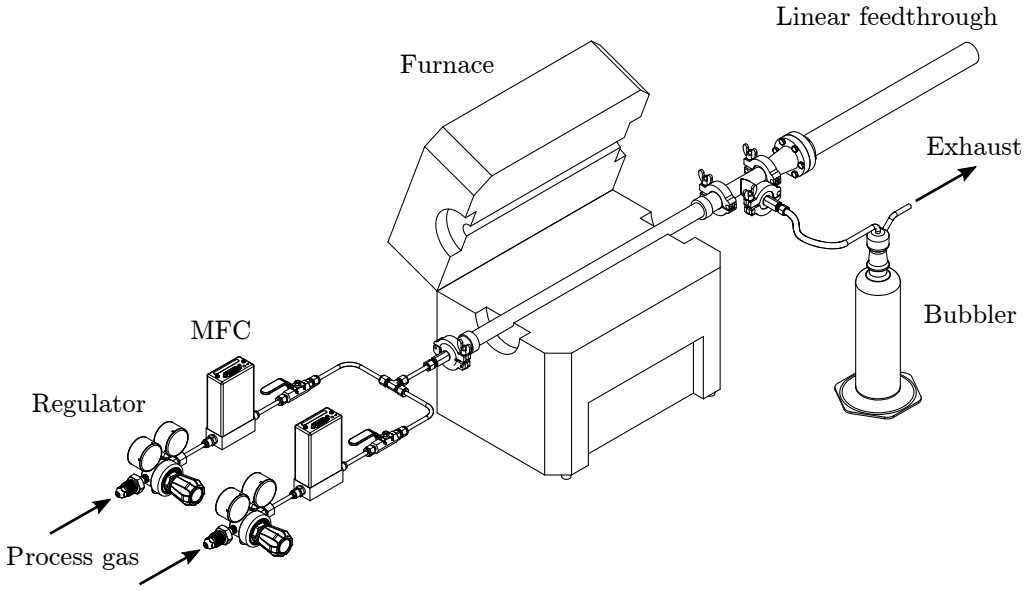

Figure 3.1: Schematic diagram of the thermal CVD system showing the main components and connections. Exact component locations and orientations do not correspond to the final arrangement in the laboratory. Connections for only two process gasses are shown for clarity.

fittings were used for their ability to be quickly disconnected and reconnected, with no practical limit on the number of re-connections. This was important as the system needs to be opened each time a new sample is processed. While intended for vacuum applications, the only pressure increase in the system originates from the major losses associated with process gas flows and the back pressure from the gas wash bottle, resulting in very little system gauge pressure.

3.1.2 Mechanical Design

Heat Transfer Calculations

A concern during the design of the CVD system was the rate of cooling of the exhaust gases, and their interaction with the vinyl exhaust tubing into the wash bottle. The vinyl tubing has a rated maximum operating temperature of $\sim$100 °C, therefore if the exhaust gases have not sufficiently cooled after exiting the furnace, this temperature could be exceeded. To check whether an extra length of a more heat resistant material would be required for cooling, some basic heat transfer calculations were conducted to find the rate of cooling of the exhaust gases in the

quartz tube after exiting the furnace.

The following assumptions were therefore made to simplify the analysis.

- Constant fluid properties
- Incompressible fluids
- Atmospheric pressure
- Fully developed internal flow
- Negligible conductive heat transfer resistance in the tube wall
- Negligible tube wall thickness ($r_i \approx r_o$)
- No radiation heat transfer

The properties of helium were used for these calculations as helium was to be the carrier gas used during CNT growth and would constitute the largest volume fraction of gas passed through the system (67 % during the growth step). The relevant thermophysical properties were taken at the log mean temperature. The conductive heat transfer resistance in the thin tube wall was assumed to be negligible compared to the resistance to convective heat transfer on the inside and outside surfaces of the tube. Figure 3.2 shows a symbolic representation of the heat transfer path. The thermal energy in the exhaust gas is transferred via convection to the wall of the tube, and then by free convection to the atmosphere at a constant temperature. Table 3.2 defines the parameters used in this analysis.

The rate of heat rejection may be expressed as a simple energy balance

$$q = \dot{m} c_{p_{He}} \Delta T \tag{3.1}$$

where $\dot{m}$ is the helium mass flow rate, and ΔT is the temperature difference between inlet and outlet. The rate of heat rejection may also be expressed as a function of the overall heat transfer coefficient $\overline{U}$

$$q = \overline{U} A_s \Delta T_{lm} \tag{3.2}$$

Table 3.2: Fluid properties and parameters used in the heat transfer analysis. Fluid properties are from Incropera et al. [116]

Parameter	Description	Value	Units	Condition
D_q	Tube diameter	0.025	m	-
T_∞	Ambient temperature	298	K	-
T_i	Inlet temperature	1273	K	-
T_o	Outlet temperature	373	K	-
T_f	Film temperature	473	K	-
T_{lm}	Logarithmic mean temperature	649	K	-
$\dot{V}$	Helium volume flow rate	8.3×10^{-6}	$\mathrm{m^3\,s^{-1}}$	@ T_∞
$c_{p_{air}}$	Specific heat capacity of air	1025	$\mathrm{J\,kg^{-1}\,K^{-1}}$	@ T_f
$c_{p_{He}}$	Specific heat capacity of helium	5193	$\mathrm{J\,kg^{-1}\,K^{-1}}$	@ T_{lm}
ρ_{air}	Density of air	0.738	$\mathrm{kg\,m^{-3}}$	@ T_f
ρ_{He}	Density of helium	0.0768	$\mathrm{kg\,m^{-3}}$	@ T_{lm}
μ_{air}	Dynamic viscosity of air	2.596×10^{-5}	$\mathrm{N\,s\,m^{-2}}$	@ T_f
μ_{He}	Dynamic viscosity of helium	3.32×10^{-5}	$\mathrm{N\,s\,m^{-2}}$	@ T_{lm}
k_{air}	Thermal conductivity of air	3.89×10^{-2}	$\mathrm{W\,m^{-1}\,K^{-1}}$	@ T_f
k_{He}	Thermal conductivity of helium	0.264	$\mathrm{W\,m^{-1}\,K^{-1}}$	@ T_{lm}
α	Thermal diffusivity of air	5.16×10^{-5}	$\mathrm{m^2\,s^{-1}}$	@ T_f

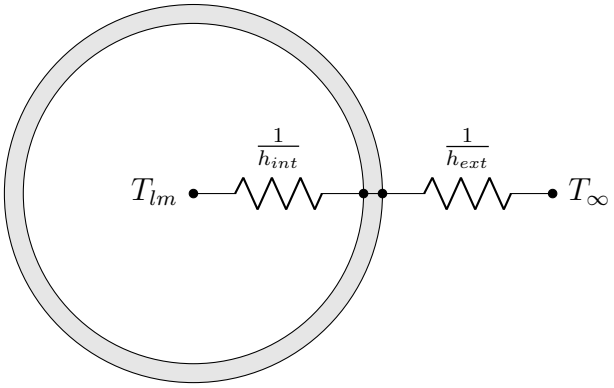

Figure 3.2: The quartz tube heat transfer model. Heat is transferred between the exhaust gas inside the tube, to the ambient atmosphere. The resistance to heat transfer may be expressed as the sum of the reciprocals of the internal convective heat transfer coefficient, and the external convective heat transfer coefficient. The tube wall thickness and the resistance to conductive heat transfer through the tube wall are assumed to be negligible in this analysis.

where A_s is the surface area of the tube, and ΔT_{lm} is the logarithmic mean temperature difference. By combining equations 3.1 and 3.2 and expanding some of the terms, the tube length required for a given change in temperature of the exhaust gases inside may be expressed as

$$L = \frac{\dot{V}\rho c_{p_{He}}(T_i - T_o)}{\overline{U}\pi D_q(T_{lm} - T_\infty)} \tag{3.3}$$

All of the above parameters are known quantities or fluid properties defined in Table 3.2, with the exception of the overall heat transfer coefficient $\overline{U}$. $\overline{U}$ relates to the sum of the reciprocals of the constituent heat transfer coefficients. In this case

$$\frac{1}{\overline{U}} = \frac{1}{h_{int}} + \frac{1}{h_{ext}} \tag{3.4}$$

The internal convective heat transfer coefficient h_{int} can be determined from the Nusselt number

$$N_D = \frac{h_{int}D_q}{k_{He}} \tag{3.5}$$

For laminar, fully developed conditions, it has been shown that the Nusselt number is equal to 3.66 [117]. We can ensure the flow is laminar by calculating the Reynolds number and verifying that it falls below 2300, the lower bound for the transition region indicating the onset of turbulence [118]. The Reynolds number is expressed as

$$Re_D = \frac{\rho_{He}u_{avg}D_q}{\mu_{He}}$$

where u_{avg} is the bulk flow velocity. The bulk flow velocity can be approximated by dividing the volume flow rate by the flow area, scaling the volume flow rate to the log mean temperature using the ideal gas law

$$u_{avg} = \dot{V}\frac{T_{lm}}{T_\infty}\frac{1}{A} = \dot{V}\frac{T_{lm}}{T_\infty}\frac{4}{\pi D_q}$$

For the resulting bulk velocity of $3.6\,\mathrm{cm\,s^{-1}}$, the Reynolds number is 2.1 and the flow laminar. Equation 3.5 may then be rearranged and solved for h_{int}, yielding a value of $38.0\,\mathrm{W\,m^{-2}\,K^{-1}}$.

The external heat transfer coefficient for free convection is more complicated. We begin by calculating the Rayleigh number, defined for a long horizontal isothermal cylinder as

$$Ra_D = \frac{g\beta\rho(T_s - T_\infty)D_q^3}{\mu\alpha}$$

where g is the acceleration of gravity, T_s is the surface temperature, and β evaluates to $\frac{1}{T}$ for ideal gases. Using T_{lm} as the surface temperature, the Rayleigh number is calculated to be 4.79×10^4. Since this value is less than 10^{12}, we are able to use the correlation for the Nusselt number recommended by Churchill and Chu [119]

$$\overline{Nu}_D = \left\{ 0.6 + \frac{0.387Ra_D^{1/6}}{[1 + (0.559/Pr)^{9/16}]^{8/27}} \right\}^2 = \frac{\overline{h}_{ext}D_q}{k_{air}}$$

where the Prandlt number Pr in this case is defined as

$$Pr = \frac{\mu}{\rho\alpha}$$

where all fluid properties are of air at the film temperature T_f, and are defined in Table 3.2. Solving for the heat transfer coefficient yields

$$\overline{h} = \frac{k_{air}}{D_q} \left\{ 0.6 + \frac{0.387Ra_D^{1/6}}{[1 + (0.559/Pr)^{9/16}]^{8/27}} \right\}^2$$

The average external free convective heat transfer coefficient evaluates to $9.8\,\mathrm{W\,m^{-2}\,K^{-1}}$. Using equation 3.4, we now calculate the overall heat transfer coefficient to be $7.8\,\mathrm{W\,m^{-2}\,K^{-1}}$. Substituting this value into equation 3.3, we find that the length of quartz tube required to achieve an exhaust gas temperature drop from 1000 °C to 100 °C is only ∼3 cm.

From this result we conclude that there is no need to provide an extra length of high

temperature tubing for exhaust gas cooling. As is, the vinyl tubing begins ∼25 cm, from the exit of the furnace, at which point the exhaust should be sufficiently cooled. Note that it is likely that our calculation for the length of tube required for cooling is an underestimate, as the omission of the resistance of the quartz tube to conductive heat transfer across its thickness increases the overall heat transfer coefficient. However, with almost ten times the length required, there is suitable margin for error. In the unlikely scenario where insufficient cooling takes place, there is also leeway provided by the ability to shift the furnace upstream on the quartz tube, yielding up to 10 cm of additional length for cooling.

Collet Adapter and Quartz Sample Holder

The magnetically coupled linear feedthrough (Figure 3.3) features a stainless steel shaft that cannot be inserted into the furnace during growth, as oxidation and other unwanted chemical reactions would occur. It is for this reason the group at MIT used a quartz extension with an integrated sample holder attached to the end of the feedthrough shaft.

The Pfeiffer linear feedthrough features an M6 threaded hole in the end of the shaft. To hold the quartz rod, a computer numerical control (CNC) collet extension adapter was purchased from Amana Tool. The collet adapter features a 6.35 mm shank, with the option for either a 6.35 mm or 3.18 mm collet. An M6 thread was cut into the 6.35 mm shank by University Machine Services (UMS), such that the collet adapter could be threaded into the end of the feedthrough shaft to hold the quartz rod. Figure 3.4 shows the modified collet adapter.

The two collet adapter variants meant the quartz sample holder could feature either a 3.18 mm rod, or a 6.35 mm rod. The former chosen for the reason that the collet nut on the 6.35 mm collet adapter had a cross-sectional area ∼50 % of the flow area and would thus significantly impede the flow.

To ensure that a long, 3.18 mm diameter quartz rod sample holder would not exhibit excessive deflection, a simple mechanical analysis was performed. The quartz sample holder was treated as a cantilever beam, with the distributed mass of the rod and the mass of the sample plate and sample exerting gravitational forces on the beam. The tip deflection was then found using the principle of superposition with the tip deflection caused by the distributed load and the point

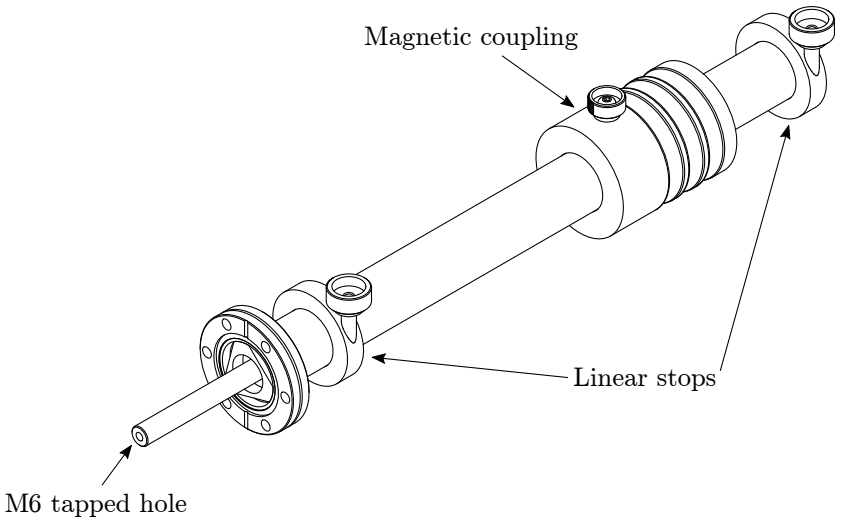

Figure 3.3: Not-to-scale diagram of the Pfeiffer magnetically coupled rotary/linear feedthrough. The feedthrough comes with linear stops for repeatable positioning, and an M6 threaded hole in the end of the 12.7 mm stainless steel shaft for attachments.

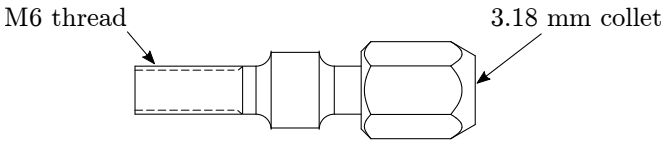

Figure 3.4: A drawing of the 6.35 mm to 3.18 mm shank CNC collet extension adapter modified by UMS to hold the quartz rod sample holder.

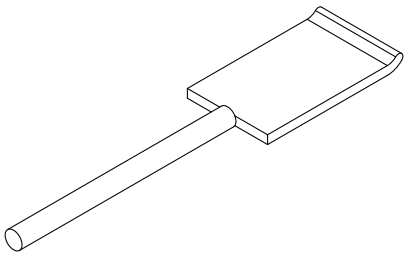

Figure 3.5: Not-to-scale drawing of the quartz sample holder. The sample holder features a 3.18 mm rod connected to a 1.59 mm thick sample plate. The sample plate features a lip at the far end to prevent samples from sliding off the front. Note that the rod has been shortened for this illustration. A detailed manufacturing drawing of the sample holder is provided in Appendix A.

load. The final form of the deflection equation is shown below [120].

$$\delta = \frac{L^3}{EI}\left(\frac{P}{3} + \frac{wL}{8}\right) \tag{3.6}$$

where P is the point load generated by the mass of the sample plate and sample, L is the length of the rod, E is the Young's modulus of quartz, w is the distributed load generated by the mass of the rod, and I is the second moment of area of the rod cross section. While less of a concern, the maximum stress developed in the rod may be calculated from the same model using the equation

$$\sigma_{max} = \frac{M_{max} r}{I}$$

where r is the diameter of the quartz rod, and M_{max} is the maximum bending moment, defined for this model as

$$M_{max} = -\frac{wL^2}{2} - PL$$

Solving using the properties of quartz and the dimensions of the sample holder yields a tip deflection of 1 nm and a maximum stress of 4 kPa. With a tensile strength of 48 MPa we can be assured the rod will not fail and will not deflect enough to be problematic. The quartz sample holder was fabricated by the university's glass blowing shop.

Linear Feedthrough Sliding Support Structure

One of the innovations of this CVD system was a sliding support structure for the linear feedthrough. In discussions with Dr. Boutilier, it was revealed that one of the primary challenges using MIT's system was the insertion and removal of samples. To do this, the quartz tube needed to be disconnected at both ends and removed entirely to place samples on the quartz sample holder. This multiple step process handling fragile components carried an increased risk of damaging the delicate quartz sample holder and the tubes themselves. Many tubes and sample holders were broken.

To avoid handling delicate components and mitigate the risk of breakage, a sliding support structure was designed for the linear feedthrough. Figure 3.6 shows how the KF-25 connection at the exhaust end of the quartz tube may be disconnected, and the linear feedthrough slid backward to access the quartz sample holder. Once the sample is positioned on the holder, the assembly slides back into place and the KF-25 clamp is replaced. The single degree of freedom movement greatly reduces the opportunity for breakage, and indeed nothing was broken for the duration of this work. A fully detailed engineering drawing of the linear feedthrough support structure is provided in Appendix A.

3.1.3 Electrical Design

The thermal CVD system is monitored and controlled over an RS-485 serial network designed by the author. The RS-485 standard defines only the electrical characteristics of the devices in the network, and does not specify a specific communication protocol [121]. RS-485 uses a differential signal over a twisted pair for reliable data transmission at speeds of up to $10\,\mathrm{MB\,s^{-1}}$, over distances of a kilometre or more. An RS-485 network may be either full-duplex or half-duplex, and uses a bus network topology.

A computer, the mass flow controllers (MFCs) and the tube furnace form the RS-485 network. A 12 V power supply is also connected to the bus to supply power to the MFCs. A diagram of the network topology is shown in Figure 3.7. The computer, a Raspberry Pi 4 model B with 8 GB of RAM running Ubuntu 20.10, interfaces with the RS-485 network through an FTDI universal serial bus (USB) to RS-485 converter. The converter, MFCs and furnace all use D-sub DB09

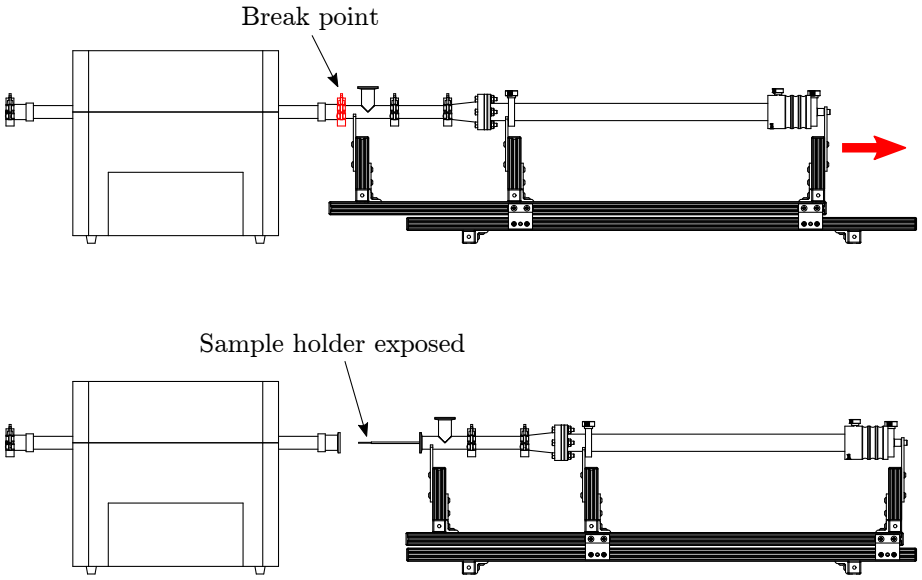

Figure 3.6: Schematic showing the movement of the linear feedthrough sliding support structure on the exhaust side of the furnace. The system is broken at the KF-25 connection shown in red. The support structure slides back, revealing the sample plate.

connectors. Custom cabling was fabricated to length using shielded 24 AWG CAT5 networking cable and DB09 solder cup connectors. The 100 Ω impedance of CAT5 network cable is not a perfect match with the 120 Ω RS-485 standard, but the CAT5 cable provides additional conductors for power delivery, and with the short cable runs of only a few metres, signal integrity proved not to be a problem.

To enable drop connections from the bus to the various devices in the network, custom signal splitters were used. The customs splitter printed circuit boards (PCBs) featured footprints for three, through-hole DB09 connectors connected in

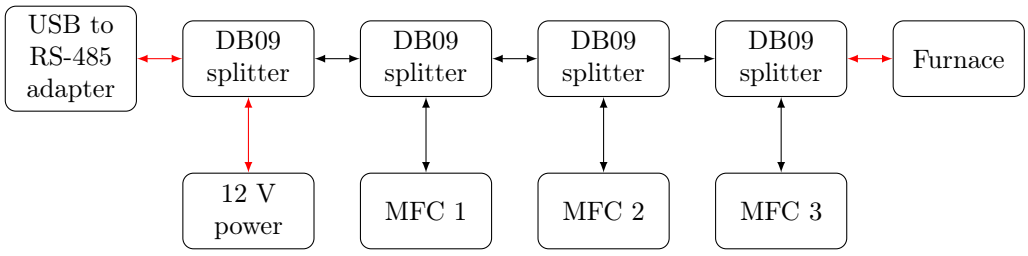

Figure 3.7: Network topology for the RS-485 network for CVD system monitoring and control. The main bus runs between the USB to RS-485 adapter and the furnace. The DBO9 splitters provide drop connections for the MFCs and power injection. Red connections show where custom cabling is required for connections where the pinout differs from one end to the other.

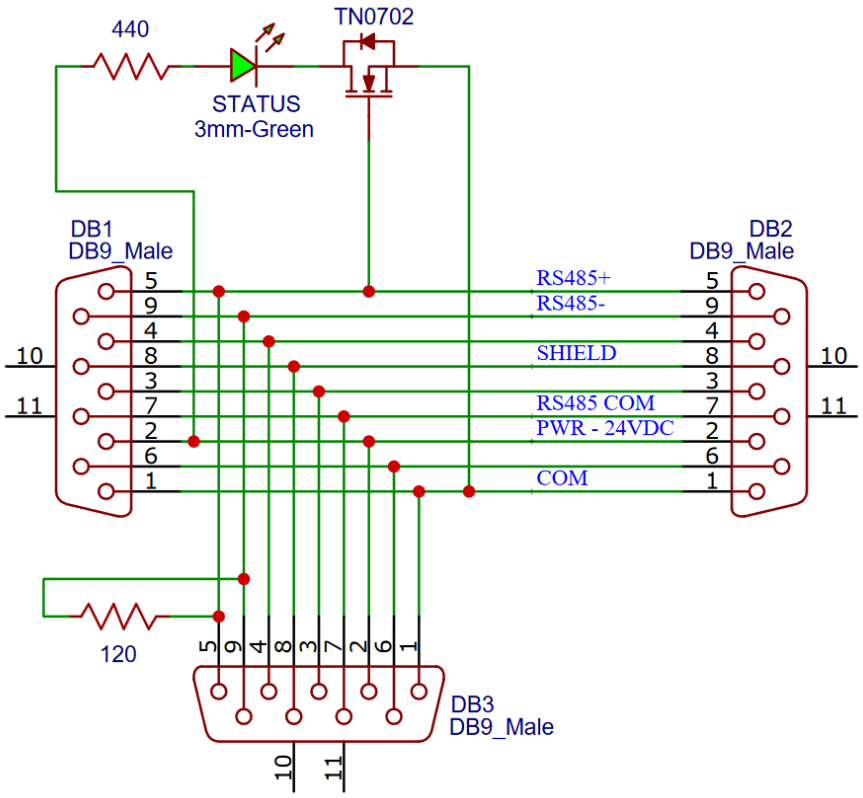

Figure 3.8: Electrical schematic of the RS-485 splitter PCB. The DB09 pin assigments match the pinout for the MFCs. A green bus status LED with current limiting resistor is included and is driven by the RS-485 data lines. Also shown is an optional 120 Ω termination resistor as specified by the RS-485 electrical standard.

parallel. Additional features for convenience and debugging included a footprint for an optional 120 Ω termination resistor, test pads for circuit debugging, and a light emitting diode (LED) circuit connected to one of the data lines for a visual indication of network activity. The two-layer PCBs were manufactured by JLCPCB and the through-hole components installed in the lab. The splitters were housed in custom 3D printed enclosures.

Complicating the electrical system design was the different DB09 pinout used by each device in the network. Table 3.3 lists the pinouts for the connectors for each device in the system. With three of the five networked devices being an MFC, it made sense for this pinout to be the "standard" for the bus. In this way, ordinary cables could connect the DB09 splitters to one another and to the MFCs, while custom cables that switch the pinout from one end to the other were required for the furnace and computer connections.

Table 3.3: RS-485 device DB09 connector pinouts as labeled on the respective data sheets.

Pin	USB to RS485	MFC	Furnace
Pin 1	DATA−	Power common	-
Pin 2	DATA+	12 V DC	DATA−
Pin 3	-	-	DATA+
Pin 4	-	-	-
Pin 5	Signal ground	DATA+	Ground
Pin 6	-	-	-
Pin 7	-	RS485 common	-
Pin 8	-	Shield	-
Pin 9	5 V DC	DATA−	-

3.1.4 Software Design

A program to control the furnace and MFCs was written in Python and run from the computer. The program includes an MFC class and a furnace class. Each class contains public methods to define setpoints, and query current values. Public methods for other common tasks such as changing the device address and reporting the device status were also included.

The MFCs and the furnace use different communication protocols. The MFCs use a custom message frame consisting of a start of message byte, a three byte device address, the command, a termination byte, and a two byte checksum. The furnace uses a Modbus protocol with a message frame consisting of a one byte device address, a one byte function code, the data bytes, and a two byte cyclic redundancy check. The public methods included in the devices classes encapsulate the message syntax unique to each device type, simplifying the commands from the main program.

The main program operates using a circular queue with first in, first out (FIFO) logic. A `QueueItem` class defines the objects stored in the queue. The `QueueItem` class includes two primary attributes, the function to be performed, and the timestamp before which the queue item is not to be executed. The main program logic operates at a frequency of 4 Hz, sufficiently fast for recipes that execute on a scale of minutes to hours. Each cycle the program checks and executes tasks in the queue according to the logic shown in the flowchart in Figure 3.9.

Most of the time, the queue contains a number of tasks, and the program executes each task when appropriate based on the `QueueItem` timestamp. In the case that

the queue is empty, the program decides how to populate the queue with tasks. When no recipe is running, the program adds a single `QueueItem` task to poll all connected devices. This allows the operator to monitor and manually operate the system even when a recipe is not running. In the case that the queue is empty and a recipe is actively running, there are two possible states indicated by the "Ramping" flag in the flowchart. If Ramping = FALSE, this means the end of a recipe step has been reached and it is time to set new setpoints. `QueueItem` tasks are created to set the new setpoints for all devices based on the recipe, and the Ramping flag is set to TRUE. Since the duration of the temperature ramp is not known, the program adds a `QueueItem` task to poll all devices and log the values one at a time until the temperature setpoint is reached. Once the temperature setpoint has been reached, the queue is populated with polling and logging tasks for the duration of the recipe step, with the timestamp attribute serving to schedule each `QueueItem` task. Once the recipe step is complete and the queue is empty, the cycle repeats for the next temperature ramp.

To more easily interact with the CVD program, a graphical user interface (GUI) was written in Python using PyQt5. A screenshot of the GUI is shown in Figure 3.10. The main feature of the GUI is an area to create, load, edit, save, start, and stop recipes. The GUI also features a section for manual control, where gas flow rates and the furnace temperature can be set without needing to load and run a recipe. On the right side of the window are live line plots showing the recent history of values reported by the furnace and the MFCs.

3.2 Results and Discussion

After the design and construction of the thermal CVD system was complete, testing was performed to validate system performance. Testing began with a number of "dry runs", where a recipe was executed without a sample in the reactor, to test the functionality of the electrical connections and control software. Once the system was confirmed to be working, testing shifted to CNT growth using silicon wafer samples with a blanket coating of catalyst. Examination of the resulting VACNTFs under optical microscope allowed fine tuning of the system and the growth recipe.

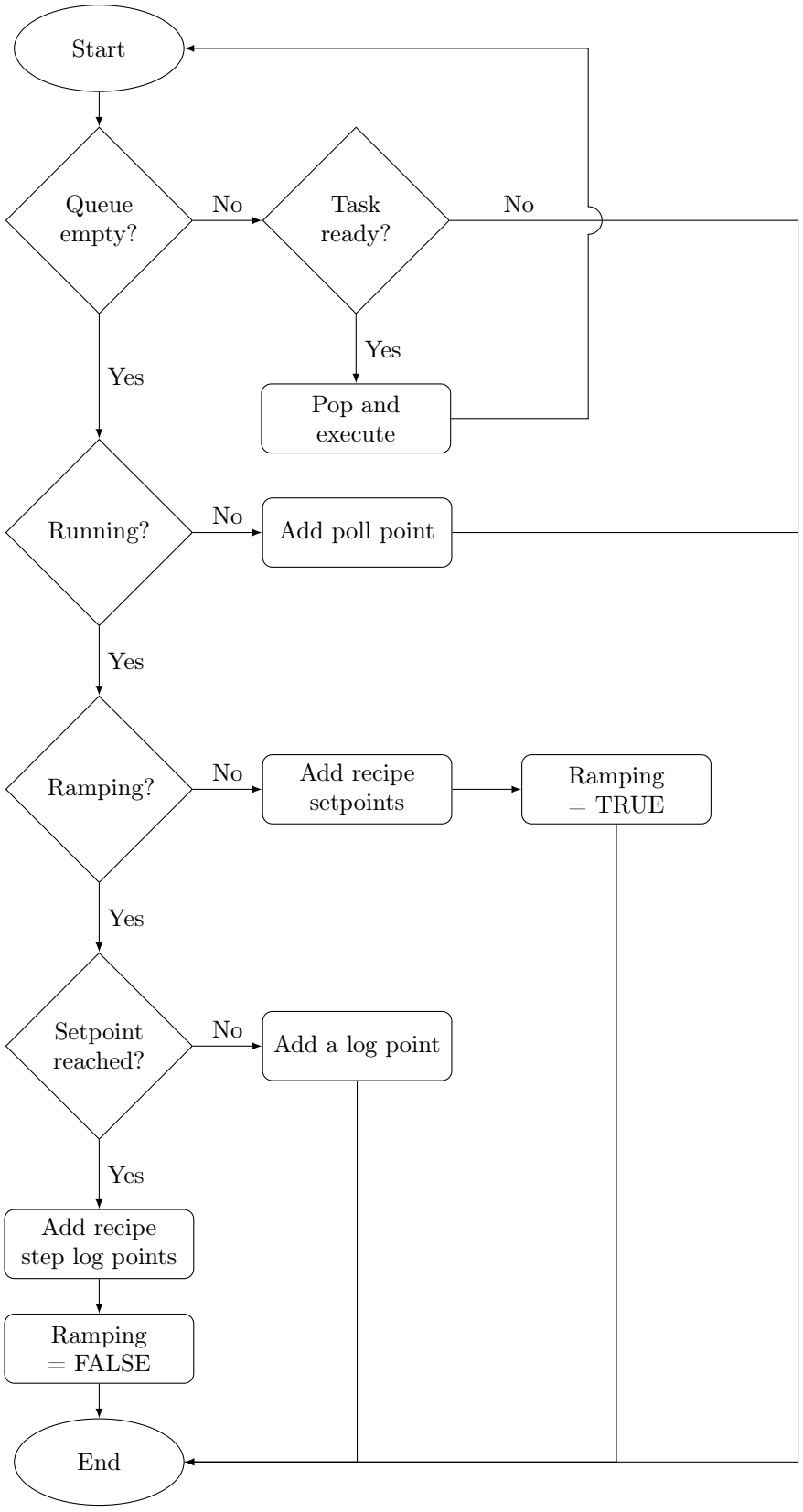

Figure 3.9: A flowchart showing the the logic used for CVD system software. The program is structured around a queue of scheduled tasks, and executes the above logic at a frequency of $\sim$4 Hz.

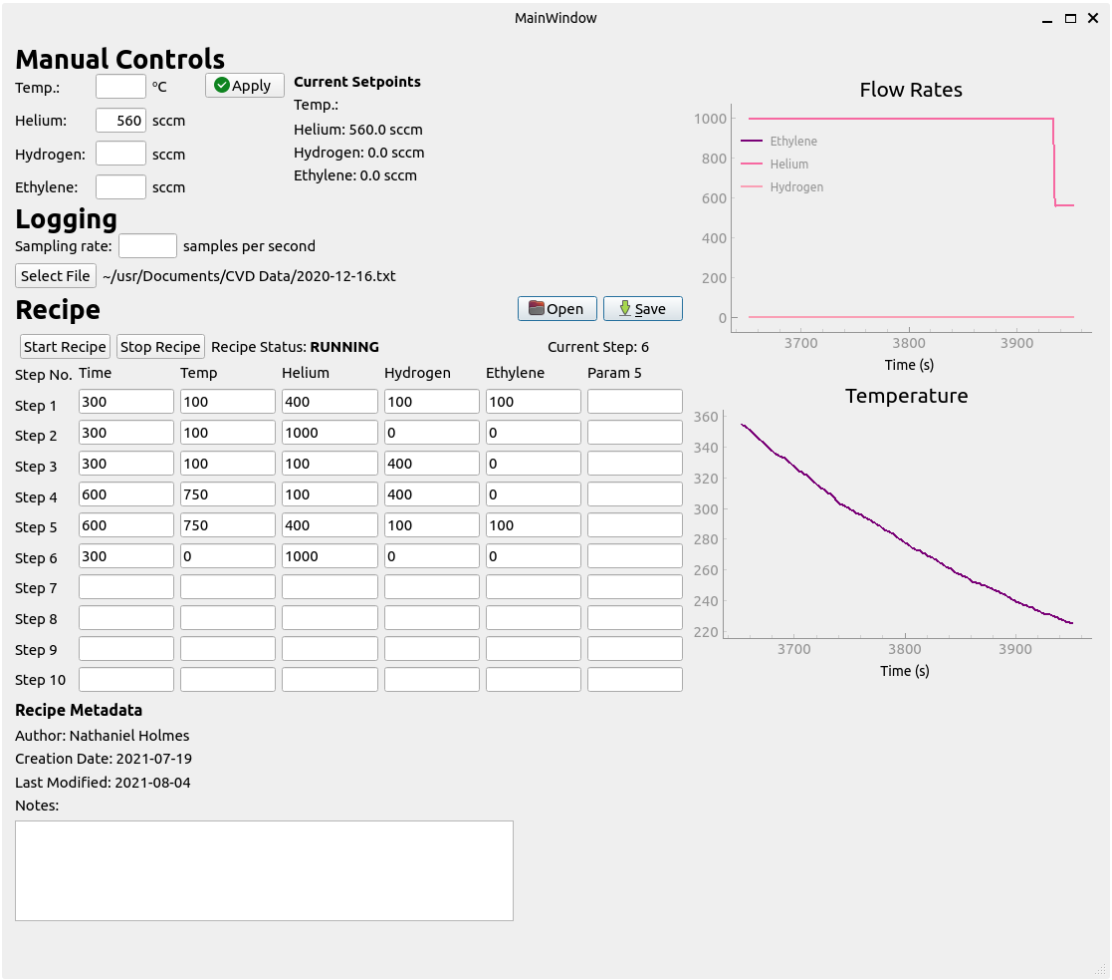

Figure 3.10: A screenshot of the CVD system GUI. On the left are the system controls, with options for manual control or automated recipe execution. On the right are live plots of the process gas flow rates and the furnace temperature.

3.2.1 Challenges

In the course of this testing, many problems were discovered and solved. One of the first tests was to verify the seal on all tubing and component connections. By closing the quarter turn plug valves, the portion of the system upstream could be pressurized using the process gasses. Pressurizing the gas lines to 100 kPa and checking the connections for leaks using soap and water revealed a leak in the ethylene regulator. This was solved by replacing the regulator. Downstream from the valves, the system could not be statically pressurized due to the low pressure components and vacuum fittings. Instead, a 1000 sccm helium purge was started and the mineral oil in the wash bottle relied on to create very slight back pressure. The connections were then checked with the soapy water and any minor leaks corrected.

Preliminary CNT growth testing on the blanket wafers revealed the first significant problem. The quartz sample holder was prone to vibration severe enough to eject samples from the sample plate. Movement of the sliding support for the linear feedthrough, of the linear feedthrough itself, or any vibrations in the lab were enough to start the quartz rod vibrating, and due to a lack of damping, it was slow to settle. At times, it seemed as if vibrations were even induced by the flow itself.

The solution to the problem of sample holder vibration was to revert to a more simple strategy. Rather than use the quartz sample holder for insertion and removal of the sample during recipe execution as was done by Li et al. [114], the strategy employed by Oliver et al. was adopted [115], using a rectangular slide cleaved from a silicon wafer. The quartz sample holder and linear feedthrough still found use as a means to push the silicon slide into the furnace prior to recipe execution, and to pull the silicon slide out after recipe completion.

While the silicon slide solution enabled CNT growth, the additional control over the process afforded by a sample holder that can be dynamically inserted and retracted during recipe execution remains desirable. The obvious solution is to redesign the collet adapter and the quartz sample holder. By switching to the Amana Tool 6.35 mm to 6.35 mm collet extension, a 6.35 mm quartz rod could be used. With the radius of the beam doubling, the second moment of area, defined for a circular cross section as $I = \frac{\pi}{4}r^4$, increases by a factor of 16. Referring back to equation 3.6, it is clear the stiffness of the beam increases by a factor of 16.

For a perfectly elastic system, this means that for a given energy input, the beam deflection will be more than an order of magnitude smaller. For our vibrating system, energy input from environmental vibrations or flow conditions will result in vibration of the sample holder that is much smaller in amplitude. We speculate that smaller amplitude vibrations would be less likely to eject the sample from the holder.

One last notable challenge encountered during system commissioning involved displaying and recording live pressure measurements. The initial concept for the system included a pressure transducer immediately upstream of the tube furnace. Oliver et al. showed a relationship between barometric pressure and CNT forest density, emphasizing the need for pressure monitoring and control for consistent CNT growth [115]. An Omega PX409-485 1000 torr absolute pressure transducer was purchased for this purpose. While this pressure transducer features an RS-485 serial connection, it uses a non-configurable baud rate of $115\,200\,\mathrm{bit\,s^{-1}}$. Meanwhile, the tube furnace features a non-configurable baud rate of $9600\,\mathrm{bit\,s^{-1}}$. Various solutions were explored, including adding a second RS-485 bus operating at $115\,200\,\mathrm{bit\,s^{-1}}$, and a micro-controller based baud rate converter that acted as an intermediate entity, receiving messages at one baud rate and passing them along at another. In the end, the simplest solution was to have the computer switch frequencies before broadcasting messages to the pressure transducer on the bus. While this requires constant re-initialization of the serial port, the slow nature of CVD processes meant that the software refresh rate could be slowed without adverse impact to the system performance. However, by the time this solution was developed, adequate CNT growth had been achieved on the blanket wafers and as such, the solution was never fully implemented.

3.2.2 CNT Growth Testing

System tuning and CVD recipe development began using wafers with a uniform catalyst layer. Figure 3.11 shows some optical microscope images of the results. Near uniform growth was observed across the surface of the wafer pieces. Panel (b) of Figure 3.11 shows a well defined VACNTF edge created by bringing a razor blade perpendicular to the silicon surface straight down and scraping to the right, leaving a clear step where the CNT forest drops away to the bare silicon surface. This provides an excellent view to measure the height of the forest, in this case

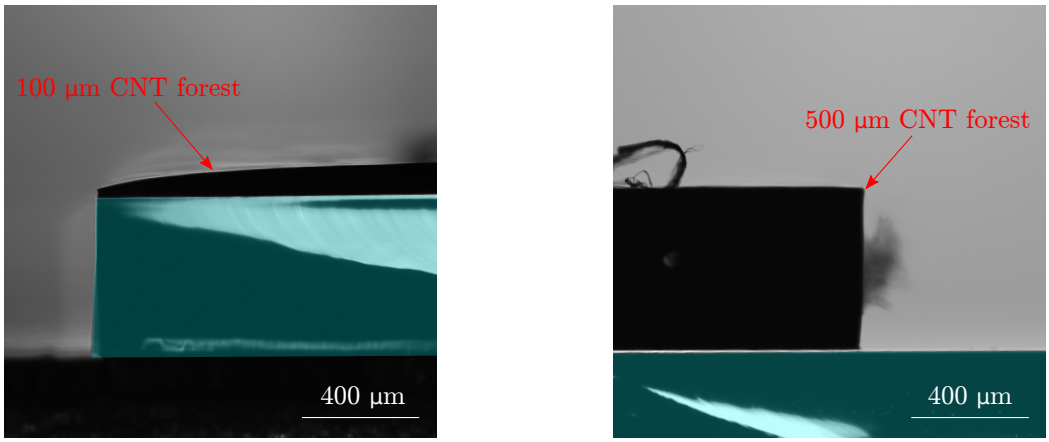

(a) (b)

Figure 3.11: Optical microscope images of VACNTFs grown on silicon wafers (highlighted in cyan) with a uniformly deposited catalyst layer. *(a)*: a view of the edge of a 0.5 mm thick silicon die with a 100 µm tall VACNTF grown on top. The height of the VACNTF tapers down to approximately 20 µm at the edge of the die. *(b)*: A well defined forest edge created by carefully splitting and scraping away the forest from the silicon surface using a razor blade. This forest is approximately 500 µm tall.

approximately 500 µm. An exception to the uniform CNT growth was a region of reduced forest height observed around the perimeter of the wafer pieces. Panel (a) of Figure 3.11 shows an example of the VACNTF height tapering off toward the edge of the wafer piece. The cause of this effect is unclear. One possible explanation is that the disruption of the gas flow caused by the sharp edge of the silicon wafer piece may disrupt the dynamics of the chemical reaction taking place, reducing the growth rate. Since uniform growth was observed across the rest of the wafer, and our sensor footprints were spread diagonally across our patterned dies, this observation did not prevent us from moving on once we had established a recipe which gave good CNT growth.

Chapter 4

Sensor Design and Fabrication

4.1 Design

4.1.1 Sensor Concept

The genesis of this project was Dr. Boutilier's idea to construct a micro-scale fluid flow sensor by building on earlier work of electronically addressable patterned VACNTFs [106]. In this concept, two electronically isolated VACNTF structures would be carefully arranged such that fluid drag would cause deflection of the structures, changing the capacitance between the two. Here we present the assumptions and design decisions as the general geometric form of the sensor was devised.

A key assumption which predicates the design decisions to follow is that high aspect ratio VACNTF structures may be treated as a cantilever beam, fixed in all degrees of freedom at the base and free in all degrees of freedom at the unsupported end. Furthermore, the base of the structure is adequately adhered to the substrate such that the application of a force to the structure causes deflection, without separation of the structure from the substrate.

The first design decision was that the mechanism whereby the capacitance signal was generated would be a change in separation of the structures. This decision evolved from an examination of the most basic model for a parallel plate capacitor

$$C = \epsilon_0 \frac{A_c}{d} \tag{4.1}$$

where C is the capacitance, ϵ_0 is the permittivity of free space, A_c is the area of the parallel capacitor plates, and d is the plate separation [122]. This model assumes uniform separation of the plates across the plate area and that the ratio of the plate area to separation distance is large enough such that the electric fields are entirely contained within the space between the capacitor plates. It is important to note that any two bodies in proximity to one another exhibit capacitance and the geometry need not be flat, parallel plates. Different geometry will change the details of the formulation for capacitance, however the positive correlation between area and capacitance and the negative correlation between separation and capacitance, will be preserved.

Equation 4.1 makes evident that the two means of changing capacitance through geometry are by changing the plate spacing or by changing the plate area. Since fluid drag was the proposed operating mechanism for the sensor, a strategy which used the drag to deflect the structures and vary their separation was the most obvious implementation.

The form of the patterned VACNTF is primarily controlled by the shape of the catalyst footprint deposited on the substrate. The next design decision therefore relates to the shape and relative position of the two footprints. We previously introduced the parallel plate capacitor model only to illustrate the nature of the proportionality between capacitance as a dependant variable and the independent variables of area and spacing. However, the simplicity of this model and its compatibility with the manufacturing techniques available make it a logical design framework for our CNT flow sensor. Applied to our footprint design, the parallel plate capacitance model requires both footprints to have an edge equal in length to, parallel to, and aligned with an edge from the other.

We further constrained the sensor footprint design by dividing the functions of the VACNTF sensor elements between the two bodies. Such a functional decomposition simplifies design decisions and sensor modelling. We designated one VACNTF structure the reference element, exhibiting less deflection in the flow and serving as a static reference for the capacitance measurement. The other VACNTF structure was designated the sensing element. The drag force on the sensing element would cause a deflection of the structure, changing the separation. Expressed in

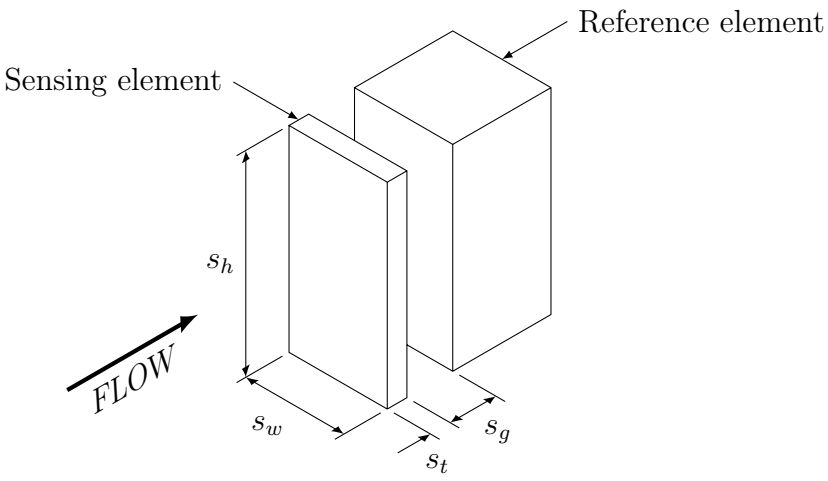

Figure 4.1: Schematic of the CNT flow sensor concept with key dimensions indicated. s_h, s_w, s_t and s_g represent the sensor, height, width, sensing element thickness, and air gap respectively. Typical values for these key dimensions are listed in Table 4.1.

terms of mechanical properties, the reference element needs to exhibit high bending stiffness when drag forces are applied and the sensing element needs to exhibit low bending stiffness when similar drag forces are applied.

Considering the requirements for matching parallel edges and differing stiffness, a simple embodiment is to have rectangular footprints with one parallel edge, and to vary the length of the perpendicular edges to alter the stiffness. Using a square footprint for the reference element bestows the added benefit of a symmetrical structure, whereby additional sensing elements may be added to the other three sides of the structure for sensitivity to flow in other directions. Figure 4.1 shows a schematic representation of the sensor geometry with key dimensions shown.

Arrival at the form shown in Figure 4.1 concluded the conceptual design of the sensor. The detailed modelling and design which followed was highly iterative as it sought to determine the optimal values for the various sensor parameters. The next section traces a simplified linear progression as it presents the detailed modelling using values which were settled on after many iterations. Table 4.1 presents a complete list of the final sensor parameter values.

Table 4.1: Finalized sensor parameters from an iterative modelling and design process for a CNT flow sensor mounted on a flat plate parallel to fluid flow. The leading edge offset represents the position of the sensor relative to the leading edge. The Young's modulus is an approximate value for the effective elastic modulus of bulk VACNTF material [81]. Room temperature air was assumed to be the working fluid.

Parameter	**Value**	
Height	s_h	100 µm
Width	s_w	50 µm
Thickness	s_t	5 µm
Air gap	s_g	5 µm
Leading edge offset	x_s	10 mm
Young's modulus	E	10 MPa
Free stream velocity	U	20 m s^{-1}

4.1.2 Fluid Model

Before we can calculate the drag forces acting on the sensor, we require a fluid model which describes the velocity field around the sensor. For this analysis, we targeted a wind tunnel experiment with air as the working fluid due to easy access to wind tunnels on campus, and the low relative permittivity of air. Due to its micro-scale size, the sensor operates within the boundary layer of the flow. The selected model must therefore accurately describe the velocity within the boundary layer and relate it to the bulk flow measurements controlled in a wind tunnel experiment.

For this analysis we chose the Blasius boundary layer solution, a steady-state two dimensional boundary layer describing laminar flow over a flat plate oriented parallel to the flow [123]. The Blasius boundary layer model was selected for its robustly proven analytical solution, as well as its simple physical configuration which could be easily replicated in a wind tunnel experiment. The concept for the experiment was to place the sensor on the surface of the plate, extending up into the boundary layer.

Blasius' solution makes use of the self-similar variable η defined as

$$\eta = \frac{y}{\delta(x)} = y\sqrt{\frac{U}{\nu x}}$$

where y is the distance from the fluid/wall interface, $\delta(x)$ is the boundary layer

thickness as a function of x, the coordinate in the direction parallel to the flow referenced from the leading edge of the plate, U is the free stream velocity, and ν is the kinematic viscosity. Blasius used η to define the normalized stream function f as a function of only η and showed that the normalized stream function satisfies the following third-order non-linear ordinary differential equation.

$$f''' + f''f = 0 \tag{4.2}$$

The horizontal and vertical velocity components of the boundary layer flow may then be calculated from the normalized stream function using the equations

$$u(x, y) = \frac{\partial \psi}{\partial y} = U f'(\eta) \tag{4.3}$$

$$v(x, y) = -\frac{\partial \psi}{\partial x} = \frac{1}{2}\sqrt{\frac{\nu U}{x}}[\eta f'(\eta) - f(\eta)]$$

where u and v are the horizontal and vertical velocity components respectively, and ψ is the stream function.

Three boundary conditions fully define this problem. The first boundary condition is imposed by the impermeability of the wall dictating the y component of the velocity must be zero at $y = 0$. The second boundary condition is the no slip boundary condition which dictates that the x component of the velocity must be zero at $y = 0$. The final boundary condition is that the x component of the velocity is equal to the free stream velocity as the distance from the wall approaches infinity. The three boundary conditions are expressed algebraically and translated to non-dimensionalized form below.

$$\begin{aligned} v(x, 0) = 0 \quad &\rightarrow \quad f(0) = 0 \\ u(x, 0) = 0 \quad &\rightarrow \quad f'(0) = 0 \\ u(x, \infty) = U \quad &\rightarrow \quad f'(\infty) = 1 \end{aligned}$$

To solve the boundary value problem this analysis uses the lsoda solver from the Fortran library odepack as implemented in the Python scientific computing library

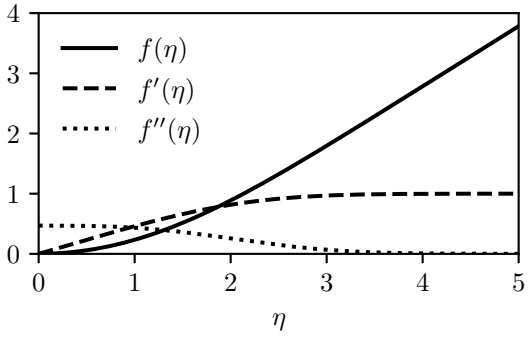

Figure 4.2: The numerical solution for the normalized stream function and its first two derivatives.

SciPy as `odeint`. To use this solver, Equation 4.2 must be translated into a system of first order ordinary differential equations. We accomplish this by defining the following

$$f_1 = f$$

$$f_2 = f_1' = f'$$

$$f_3 = f_2' = f''$$

Substituting back into Equation 4.2 yields the system of first order ordinary differential equations shown below.

$$f_1' = f_2$$

$$f_2' = f_3$$

$$f_3' = -f_3 f_1$$

The `odeint` solver yields the solution for the normalized stream function shown in Figure 4.2. Equation 4.3 may then be used to calculate the horizontal component of the fluid velocity in the boundary layer at any coordinate (x,y). Figure 4.3 shows a visualization of the horizontal flow velocity in the region extending back from the leading edge of a flat plate. The horizontal flow velocity was subsequently used to estimate the drag force exerted on the sensing element. A free stream velocity of $20\,\mathrm{m\,s^{-1}}$ was chosen as a velocity that could reasonably be achieved in

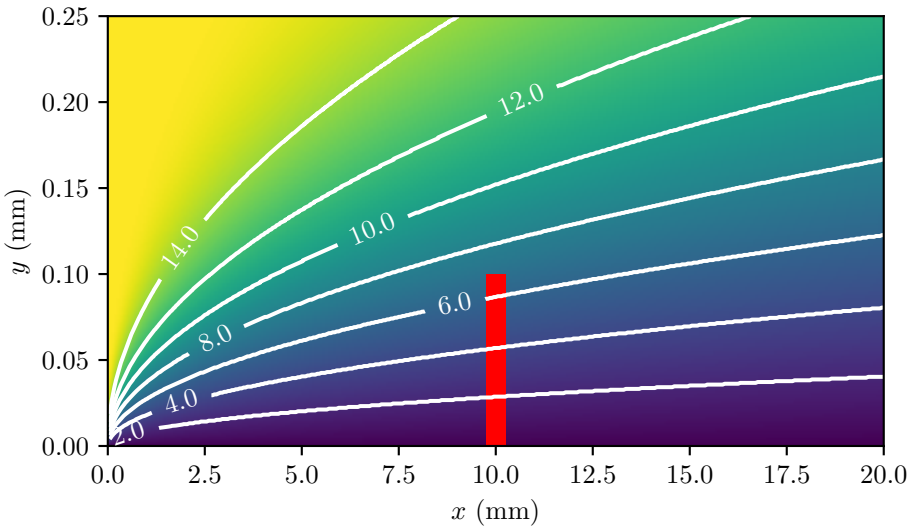

Figure 4.3: Visualization of the horizontal velocity component of the Blasius boundary layer solution for air with a free stream velocity of $20\,\mathrm{m\,s^{-1}}$. The red bar represents the CNT sensing element and is to scale in the y direction. Contour labels show the horizontal velocity in $\mathrm{m\,s^{-1}}$.

most wind tunnels.

4.1.3 Solid Mechanics Model and Capacitance Signal

The solid mechanics analysis used a simplified finite element method to estimate the sensing element deflection. The sensing element was divided into 25 equal sections along its height and the average flow velocity at each height was interpolated from the fluid model. A drag force was calculated for each section and beam deflection equations used to calculate the deflection caused by the drag force on each section. Finally, the method of superposition was leveraged to find the total deflection caused by all the discrete drag forces along the height of the beam.

The first step was to use the fluid model to obtain a velocity profile along the height of the sensing element. Selection of the velocity vector at the position $x = 10$ mm from the two-dimensional boundary layer solution matrix visualized in Figure 4.3 yields the velocity profile shown in the left panel of Figure 4.4. Using the velocity profile we can calculate the local Reynolds number for each section of the discretized sensing element using the width of the pillar as the characteristic length. The local Reynolds number increases almost linearly up to 23 at the free

end of the sensing element

The total drag on the sensing element was approximated by summation of the drag on a flat plate normal to flow, the shear stress on the side surfaces, and the shear stress on the top surface. We begin with the flat plate drag. Relatively little research has been done on flat plate drag at such low Reynolds numbers. In his 1958 Master's thesis, Alva Jones observed the following relationship for the drag coefficient of a flat plate in perpendicular flow [124].

$$C_d = \frac{37}{\mathrm{Re}}\mathrm{AR}^{-0.3} \qquad 0.05 \leq \mathrm{Re} \leq 2 \quad \text{and} \quad 1 \leq \mathrm{AR} \leq 4 \tag{4.4}$$

Where Re is the Reynolds number and AR is the aspect ratio of the plate. Unfortunately this relationship was only tested across a small subset of the range of local Reynolds numbers for our sensing element, and there has been little research done on flat plate drag in the range $2 \leq \mathrm{Re} \leq 25$. We can justify the use of Equation 4.4 across the entire range of local Reynolds numbers by looking at higher Reynolds number research. Many studies have looked at the drag coefficient for rectangular plates, square plates and disks perpendicular to flow in the range $7 \cdot 10^4 \leq \mathrm{Re} \leq 3 \cdot 10^5$ and found the drag coefficient for all to be largely independent of Reynolds number and varying from 1.14 to 1.17 [125, 126, 127]. We therefore expect Equation 4.4 to flatten out to a near constant value around 1.15 at higher Reynolds numbers. Evaluating Equation 4.4 with $\mathrm{Re} = 23$, the previously calculated local Reynolds number at the top of the sensing element, and $\mathrm{AR} = 2$, yields a drag coefficient of 1.3. Since this is not below 1.15, Equation 4.4 seems to be a reasonable approximation for the drag coefficient across the entire height of the sensing element.

With element thicknesses up to 10 µm modelled, the thickness of the sensing element as a proportion of the element width was not negligible and the shear stress along the element edges and top could not be neglected. Edge shear and top shear were calculated by treating the sides as flat plates, using the average skin friction drag coefficient for laminar flow, defined by

$$C_f = \frac{1.328}{\sqrt{\mathrm{Re}_L}} \qquad \mathrm{Re}_L < 5 \cdot 10^5$$

where the characteristic length is the wetted length parallel to the flow [128] (in this case the sensing element thickness).

For each segment of the sensing element, the local velocity was used to calculate the skin friction drag coefficient, which in turn was used to calculate the drag force for that segment using the drag equation

$$F_d = \frac{1}{2}\rho C_f V^2 A$$

where ρ is the fluid density, V is the local fluid velocity, and A is the wetted area on the sides of the sensing element (and the top of the sensing element for the uppermost segment).

The total drag force acting on each sensing element section was calculated by summation of the flat plate drag component and the skin friction drag component on that element section. The centre panel in Figure 4.4 shows the result. The large increase in drag force at the free end of the sensing element is due to the skin friction on the top face of the CNT pillar.

Deflection was calculated using superposition of the deflection caused by the drag force on each pillar segment. The deflection Δx of a cantilever beam of height h at a point y along its length subjected to a point load F at a distance a from the supported end is defined by the piece-wise continuous function

$$\Delta x = \frac{Fy^2}{6EI}(3a - y) \quad \text{for} \quad 0 < y < a$$

$$\Delta x = \frac{Fa^2}{6EI}(3y - a) \quad \text{for} \quad a < y < h$$

where E is the Young's modulus and I is the second moment of area of the cross-section [120]. The results of the solid mechanics analysis are shown in the right panel of Figure 4.4. The sensing element deflection resembles the typical profile for a cantilever beam in bending, with a maximum deflection at the free end of just over 4 µm. With an air gap of 5 µm, 4 µm is an ideal amount of deflection, as it will give good sensitivity without the sensing element and reference element contacting one another and creating an electrical short circuit.

The final step in the deflection analysis was to translate the anticipated deflection to a capacitance change. To do this we revisit the parallel plate capacitance model described by Equation 4.1. Using the same discretization approach, we treat each segment of the sensing element as a parallel plate capacitor, and calculate the total

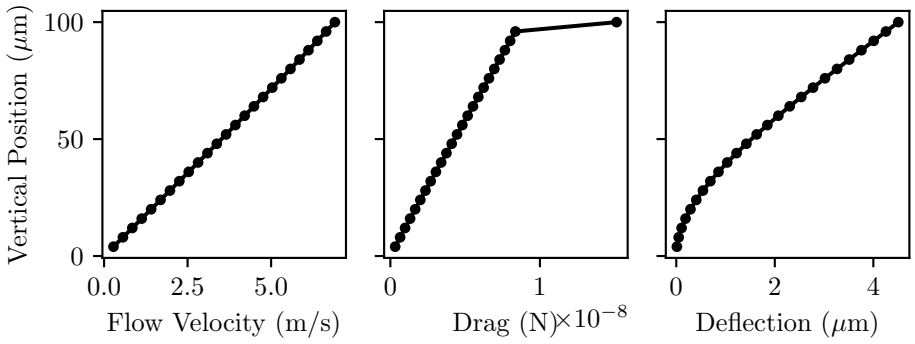

Figure 4.4: Sensing element deflection modelling using a 25 element discretization. *Left*: horizontal velocity vs. vertical position. The velocity gradient is nearly linear at such a low Reynolds number. *Centre*: drag vs. vertical position. The large increase in drag at the tip of the sensor is due to the shear drag on the top surface of the structure. *Right*: deflection vs. vertical position. The total deflection is significant enough to produce a signal, but does not bridge the 5 µm gap between the sensing element and the reference element.

capacitance as the sum of all segments. Note that in doing so we violate one of the core assumptions of the parallel plate model, that the plates are parallel and uniformly spaced across their whole area. The fact that this is not the case means that a uniform charge density on the two elements, and thus a uniform electric field between the two, is not guaranteed. While this undoubtedly affects the accuracy of our calculations, the method we have outlined above (effectively a weighted average) should produce results accurate enough for us to get a general idea of the magnitude of the capacitance change when the sensing element is deflected. A more in depth analysis would be non-trivial and is unnecessary for this level of design. The approach is expressed algebraically as

$$C_{deflected} = \sum_{i=1}^{i=n} \epsilon_0 \frac{s_h s_w}{n(s_g - x_i)}$$

where n is the number of sensing element segments, x_i is the local deflection, and s_h, s_w and s_g are the height, width and air gap as defined in Figure 4.1

To obtain the change in capacitance, we subtract the initial capacitance from the calculated deflected capacitance using the equation

$$\Delta C = C_{deflected} - \epsilon_0 \frac{s_h s_w}{s_g}$$

Using the finalized parameters listed in Table 4.1, the modelling predicts a change in capacitance of 12.1 fF. This signal is well within the measurable range of the AD7746 integrated circuit (IC) used for capacitive measurements, which has a full-scale capacitance range of ±4 pF, an accuracy of 4 fF, and a resolution of 4 aF.

4.1.4 Sensitivity Analysis

The sensor modelling above relies on a host of simplifications that introduce significant, unquantifiable uncertainty in the model output. To mitigate the risk that model inaccuracy could lead us to produce a sensor that would not produce meaningful results in the flow experiment, we planned to produce a number of different sensor configurations with varying sensitivity. The sensing element height, width, thickness and air gap were the four geometric parameters most easily controlled through the photomask design. While the Young's modulus was also likely to have a large effect on the output, it could not be directly controlled. To inform our decision about which parameters to change to vary the sensitivity, we performed a sensitivity analysis to better understand which parameters had the greatest influence on the sensor output.

We began the sensitivity analysis by establishing a baseline configuration from which each parameter was individually varied through a range of realistic values. Table 4.2 lists the parameters, their baseline values, and the range for the sensitivity analysis. For the height, a taller sensing element would deflect more for a given drag force. The maximum height was limited by our ability to synthesize tall VACNTFs. Previous work indicated that 100 µm was a reasonable expectation [104]. For the width, 50 µm was selected as the baseline since it gave a height to width aspect ratio of 2, which was expected to yield a robust structure. The lower and upper width limits were set to half and double the baseline respectively, as any narrower would yield a less robust structure, and there was no clear benefit to making the sensing element any wider. The baseline thickness and air gap both had minimum values of 3 µm, as discussions with the Western Nanofabrication facility indicated that smaller feature sizes would be difficult to achieve with the

Table 4.2: Parameter baseline values and ranges for the sensitivity analysis. The leading edge offset, Young's modulus and free stream velocity are not related to the photomask design and were therefore held constant for the sensitivity analysis.

Parameter	**Baseline**	**Min.**	**Max.**
Height (µm)	100	50	100
Width (µm)	50	25	100
Thickness (µm)	5	3	10
Air gap (µm)	5	3	10
leading edge offset (mm)	10	-	-
Young's modulus (MPa)	100	-	-
Free stream velocity (m/s)	20	-	-

equipment available. The baseline values were specified to be slightly larger at 5 µm to increase the chances of successful fabrication. The maximum values were set to 10 µm as it was deemed unlikely that less sensitivity would be required beyond this point.

Finally, a note about the leading edge offset and Young's modulus parameters. The leading edge offset was held constant at 10 mm from the leading edge of the flat plate, as this parameter had no bearing on the photomask design, and could easily be changed during the flow experiment. The Young's modulus is difficult to control and also does not influence the photomask design, and as such it was also held constant. Note that the the Young's modulus for the sensitivity analysis was increased to 100 MPa from the 10 MPa used for the final model sensor parameters. A higher Young's modulus ensured that as parameters were varied in the sensitivity analysis, the sensing element did not deflect too far and contact the reference element. It also helped develop an understanding of the anticipated sensor response should our 10 MPa value be found to be a significant underestimate.

For each configuration, the entirety of the solid mechanics and capacitance response analysis was performed, and the estimated capacitance change recorded. Figure 4.5 shows the results of the sensitivity analysis. The output is most sensitive to the thickness and the air gap, and is notably more sensitive to changes as the thickness and air gap get smaller. The thickness and air gap were therefore selected as the two variable parameters in the photomask design to fabricate sensors with different sensitivity and increase the probability of experimental success.

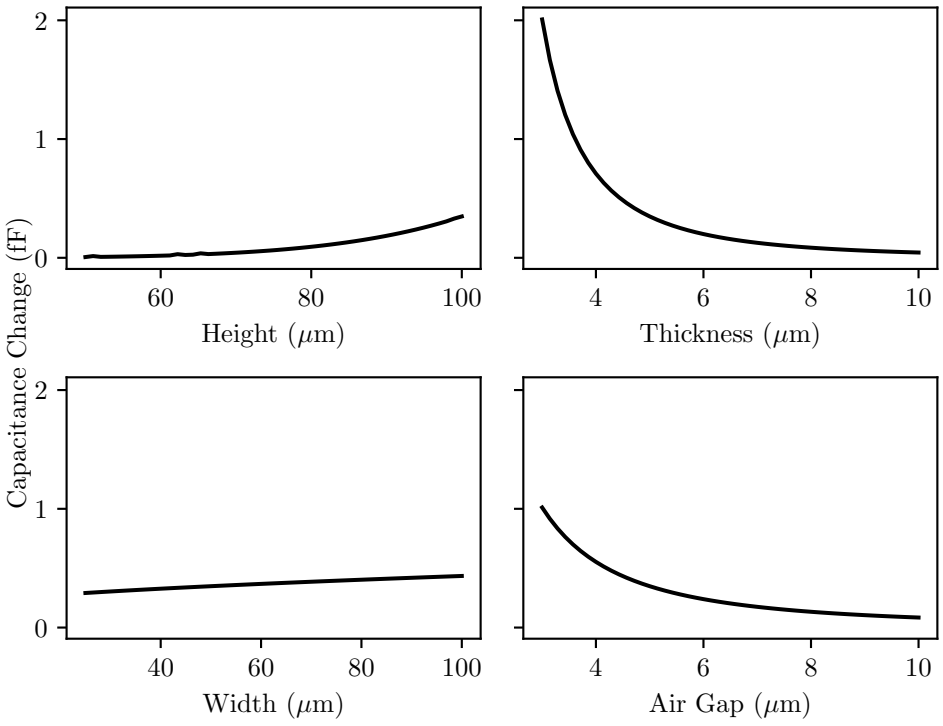

Figure 4.5: CNT flow sensor sensitivity analysis. The height, thickness, width and air gap as defined in Figure 4.1 were individually varied through the ranges defined in Table 4.2.

Table 4.3: Photomask die configuration summary. The configuration value corresponds to the enumeration in Figure 4.6 and is ordered from most sensitive (Config. = 1) to least sensitive (Config. = 5).

Config.	**Count**	**Thickness** (µm)	**Air Gap** (µm)
1	15	3	5
2	24	5	5
3	12	5	8
4	8	8	8
5	7	10	10

4.1.5 Photomask Design

Fabrication of the flow sensor required a photomask for the catalyst pattern and a photomask for the conductive tracing pattern. The photomasks were designed for 101.6 mm diameter silicon wafers, the size most commonly processed at the Western Nanofabrication facility. The wafer was sectioned into 66, 10 mm by 10 mm square dies. This die size makes good use of the wafer area and is convenient to handle.

The 66 dies were divided into the five configurations detailed in Table 4.3. For each configuration the thickness and air gap were changed to affect the sensitivity. The sensor configuration deemed most likely to yield good results (5 µm thickness and air gap) was allocated the largest number of dies. Configurations that were deemed less likely to yield good results were given fewer dies and were positioned toward the edges of the wafer. Figure 4.6 shows the complete wafer layout.

The final form for the sensor footprint was a square base for the reference element, with twin sensing elements situated on adjacent sides (shown in the right panel of Figure 4.7). The decision was made to include orthogonal sensing elements as the AD7746 integrated circuit used for the capacitance measurement has two channels, and it was thought that an additional sensing element might enable interesting possibilities for future experiments. The sensor footprints were arranged along the diagonal of each die. Each footprint had the same orientation, ensuring that each sensing element would see clean flow unobstructed by any other sensor.

To reduce parasitic capacitance, parallel traces to the same sensor were avoided by routing the trace for the reference element and the traces for the sensing elements to different edges of the die. Each conductive trace originates underneath a

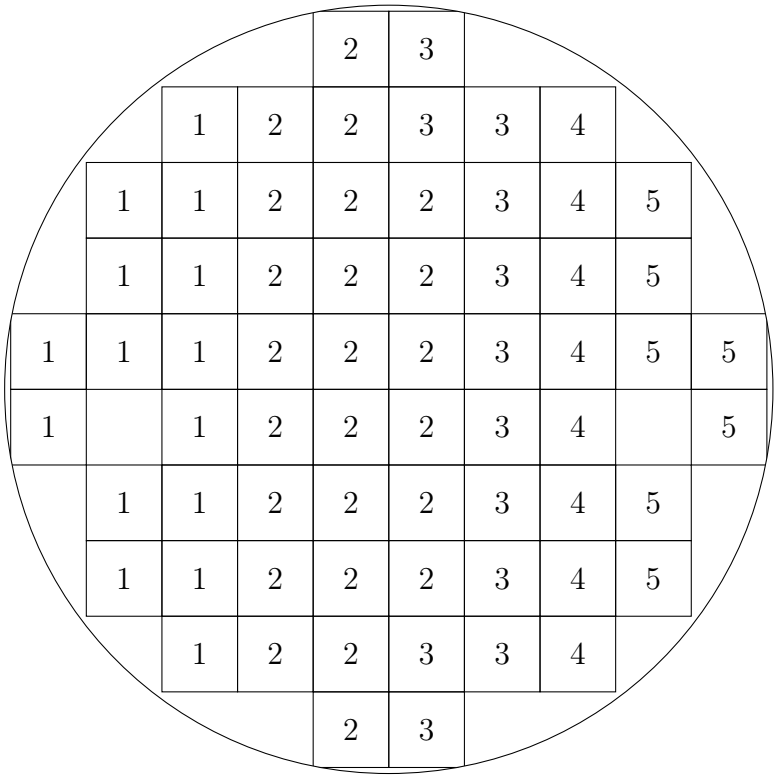

Figure 4.6: Die configuration layout on the 101.6 mm silicon wafer. Each square represents a 10 mm by 10 mm silicon die. The number on the die represents the configuration of the four sensors on that die. Table 4.3 defines the five configurations. Two dies were left blank for the inclusion of alignment marks used in the photolithography process.

segment of the sensor footprint and terminates at a round electrical contact at the edge of the die. Since the copper tape used in the flow experiment to make the electrical connection to the round contacts would protrude above the die surface and disrupt the flow, the contacts needed to be located along the two die edges downstream from the sensing elements. The left panel of Figure 4.7 shows the layout of the conductive tracing on each die.

With a sensor footprint smaller than 100 µm by 100 µm, the design of the conductive traces limited the number of sensors on each die rather than the size of the sensor itself. The round electrical contacts needed to be large enough to connect to with copper tape. It was decided that a pad 1 mm in diameter was an appropriate compromise for the competing objectives of maximizing the number of sensors on a die and facilitating the electrical connection. This left room for a maximum of four sensors arranged diagonally across the square die, with eight contacts for the sensing elements along one edge, and four contacts for the reference elements along an adjacent edge.

The catalyst patterns were sized per the specifications in Table 4.3 and arranged per the layout in Figure 4.6. The conductive tracing beneath each catalyst region was oversized 1 to 2 µm to provided flexibility in the event of photomask misalignment and prevent distorted forest growth due to the catalyst layer running off the edge of the conductive trace. A 3 µm gap, the smallest feature size the Nanofab could reliably produce, was maintained between adjacent sections of conductive tracing to prevent electrical short circuits. The complete photomask designs are included in Appendix A.

4.2 Fabrication

4.2.1 Wafer Fabrication

Both the catalyst photomask and the conductive tracing photomask were 5 in by 5 in darkfield masks on soda lime glass and were manufactured by Front Range PhotoMask. 101.6 mm diameter, 1 µm thermal oxide silicon wafers were used. The wafers were first washed in a Semitool ST-240D spin rinse dryer. A hexamethyldisilazane (HMDS) adhesion layer was then applied using a Yield Engineering YES-3TA HMDS oven. MICROPOSIT S1805 photoresist was coated on the wafer

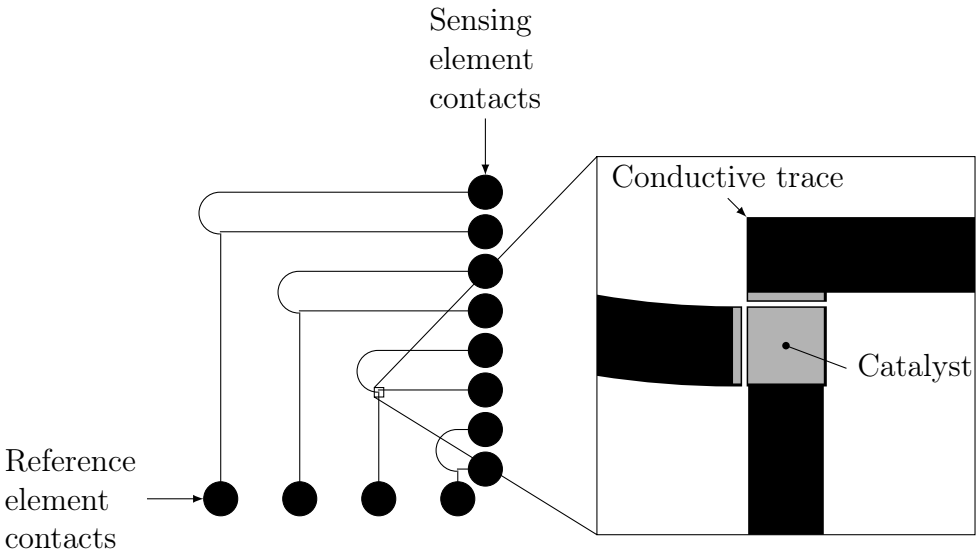

Figure 4.7: Sensor and conductive tracing layout on each 10 mm by 10 mm die. *Left*: layout for the complete die showing the conductive tracing. The four sensors lie at the confluence of the conductive traces and are too small to see in this view. *Right*: expanded view of the sensor footprint showing the conductive trace and catalyst layout.

with a Cost Effective Equipment 200 spin coater at 3000 RPM. The wafer was heated at 113 °C for 2 minutes on a Thermoscientific SuperNuova hotplate to cure the photoresist.

Next, the wafer was taken to the Neutronix-Quintel NXQ 4006 mask aligner for the conductive trace patterning. A 405 nm light source with 38 mW cm^{-2} intensity was used for the exposure. Given the small feature size, both the default mechanical pressure and optional vacuum functions were used for more intimate contact between the mask and wafer. For development, the wafer was placed in a shallow bath of MICROPOSIT MF-319 developer at 3.2 % concentration and agitated for two minutes. The wafer was then rinsed with de-ionized water and dried using a stream of compressed nitrogen.

Once the photoresist had been patterned for the conductive tracing, Tim Goldhawk from Western's Nanofabrication facility performed the deposition of a 50 nm layer of TiN by evaporation. Mr. Goldhawk also performed the liftoff procedure to complete the TiN tracing, leaving the wafer ready for catalyst patterning.

Patterning for the catalyst layer used the same materials and processes as the photoresist patterning for the conductive tracing. Alignment of the catalyst pho-

Table 4.4: Pre-growth recipe. The purpose of the zero duration steps is to specify the gas flows during temperature ramps.

Step	**Description**	**Duration** (min)	**Temp.** (°C)	**Helium** (sccm)	**Hydrogen** (sccm)	**Ethylene** (sccm)
1	Purge	5	100	400	100	100
2	Purge	0	775	1000	0	0
5	Growth	20	775	400	100	100
6	Cool-down	0	0	600	0	0

tomask to the conductive tracing used the windows and alignment marks included in the photomask design. Deposition of 10 nm of Al_2O_3 followed by 2 nm of Fe by evaporation was again performed by Mr. Goldhawk. With patterning and deposition complete, a layer of MICROPOSIT S1827 photoresist was spun onto the wafer as a protective layer. The wafer was then placed onto a piece of dicing tape and cut into 10 mm by 10 mm squares using a dicing saw.

Finally, blanket wafers for the purpose of CVD recipe development and system tuning were prepared by deposition of 10 nm of Al_2O_3 followed by 2 nm of Fe on 101.6 mm diameter, 1 µm thermal oxide silicon wafers using the same process as for the patterned wafers.

4.2.2 Chemical Vapour Deposition

The chemical vapour deposition CNT growth procedure began with the removal of carbon deposits that had built up on the inside surface of the quartz tube and on the silicon slide during previous CVD processes. Oxidation of the carbon deposits was achieved by heating the tube to 1100 °C for 20 minutes. The KF-25 flanges at both ends of the quartz tube were disconnected during this time so that atmospheric oxygen could enter the tube.

The quartz tube cleaning was followed by execution of the pre-growth recipe detailed in Table 4.4. A pre-growth recipe was included in the procedure for this experiment based on previous investigations that found carbon deposits on the reactor walls to be beneficial for VACNTF growth [129]. The pre-growth recipe was run with the silicon slide positioned in the same location as for the actual CNT growth recipe, but without a silicon die.

As the quartz tube was being cleaned and the pre-growth recipe run, the silicon die

Table 4.5: CNT growth recipe.

Step	**Description**	**Duration** (min)	**Temp.** (°C)	**Helium** (sccm)	**Hydrogen** (sccm)	**Ethylene** (sccm)
1	Purge	5	100	400	100	100
2	Purge	5	100	1000	0	0
3	Equilibrate	10	100	100	400	0
4	Anneal	10	775	100	400	0
5	Growth	10	775	400	100	100
6	Cool-down	5	100	1000	0	0

was prepared. The protective layer of photoresist applied before die saw cutting was only removed immediately prior to CVD growth to keep the surface as clean as possible. The protective layer was removed by cleaning with propan-2-one in a Branson CPX1800H 40 kHz ultrasonic cleaner for five minutes. The ultrasonic cleaning was repeated twice more for the same duration in propan-2-ol. After the final cleaning, the die was removed from the propan-2-ol and any residual liquid blown off with a compressed stream of air before it could evaporate. The die was placed on the silicon slide 30 mm back from the leading edge. The CVD system was opened at the KF-25 connection on the downstream side of the furnace. The slide was then placed into the quartz tube, and positioned with the leading edge of the slide 10 mm downstream of the furnace thermocouple using the magnetic transporter. The KF-25 connection was sealed and the furnace lid closed. From the computer, the GUI was launched and the recipe loaded.

Table 4.5 details the most successful recipe used in this experiment. For each recipe step, the step duration timer was only started once the furnace temperature reached the step set point. Step 1 purges impurities from all gas lines. Step 2 is a continued purge using only inert helium to remove traces of the gases from the first step. Step 3 is the final purge step, using the gas mixture for the upcoming anneal step and holding for 5 minutes to allow the system to reach equilibrium. The annealing takes place in step 4, where the temperature is held at 775 °C for 10 minutes without a carbon source. In step 5, ethylene is added and CNT growth begins. In the final step, a helium purge accompanies cooling down to 100 °C. The tube furnace may be opened during this step to speed the cooling. Figure 4.8 shows a plot of the data logged during a recipe execution.

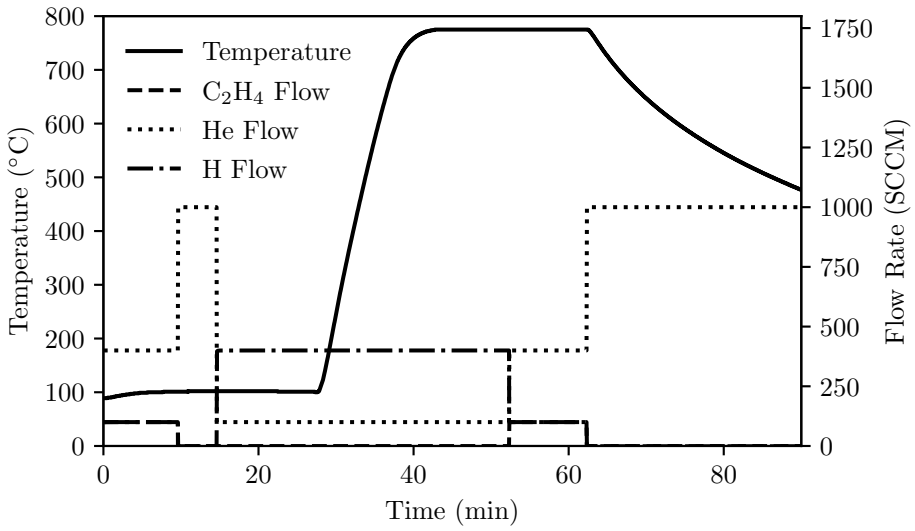

Figure 4.8: Gas flow rates and furnace temperature versus time, as recorded during recipe execution.

4.3 Results and Discussion

Figure 4.9 shows optical microscope images of the results from the photolithography process. The photographs show a high fidelity replication of the photomask geometry with no visible protective photoresist remaining and a surface free of micro-scale debris which could negatively impact CNT growth.

Panel (b) shows a higher magnification view of the sensor footprint. Slight horizontal misalignment of the catalyst and conductive layers is evident when compared to the intended layout illustrated in Figure 4.7. With feature sizes as small as 3 µm, this photomask design approached the limit of the NXQ 4006 mask aligner's capabilities, and the small production batch of only two wafers provided little opportunity for technique refinement when operating the machine. While better alignment could be achieved, this degree of misalignment was reasonable given the circumstances.

The observed misalignment is problematic primarily for the left sensing element. Bridging between the conductive tracing for the left sensing element and the conductive tracing for the reference element by the catalyst layer for the left sensing element would cause an electrical short, preventing meaningful readings from the left sensing element. Moreover, multiple studies have shown the catalyst substrate to influence the growth rate of CNTs [130, 104]. Results from these studies suggest

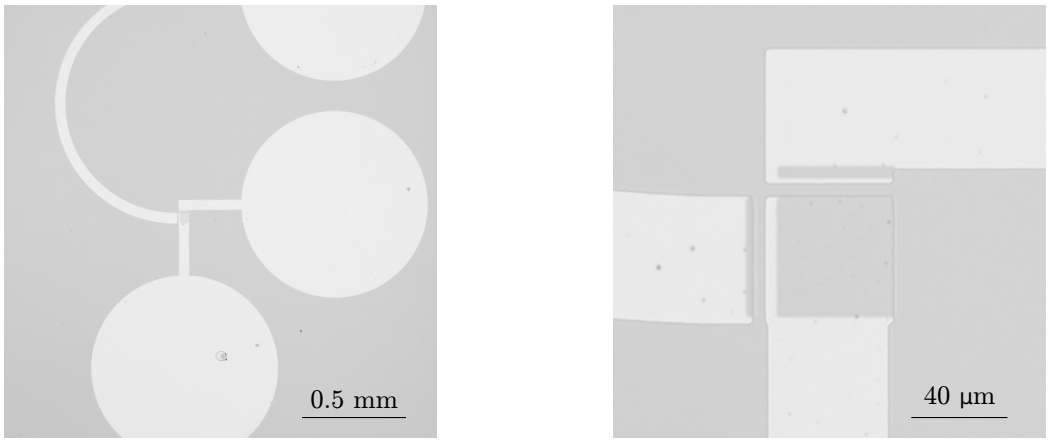

(a) (b)

Figure 4.9: Die viewed under an optical microscope after removal of the protective photoresist, and before CNT growth.

that the growth rate of the CNTs grown from catalyst situated on SiO_2 will be higher than that of CNTs grown from catalyst deposited on the TiN conductive trace [104]. We would therefore anticipate that due to the catalyst deposition which has spilled off the edge of the TiN base layer, the left sensing element will curve away from the reference element during growth. While better alignment may have been achieved with more attempts, this was not required as the alignment of the top sensing element was deemed satisfactory for this experiment. The horizontal misalignment was unlikely to adversely affect the growth or function of the top sensing element.

Achieving the VACNTF target height of 100 µm proved much more challenging on the patterned dies than on the blanket wafers used during commissioning of the thermal CVD system. The height of the VACNTF structures was also more difficult to measure due to their small size and distance from the edge of the die. Figure 4.10 shows two views of the same 50 µm tall sensor through an optical microscope. This sensor was one of the tallest sensors we were able to produce.

It is unclear why the synthesis of taller patterned VACNTF structures eluded us after the successful growths on the unpatterned wafers. One possibility is that the TiN conductive tracing was limiting the growth rate more than anticipated. De Volder et al. found the presence of a 80 nm thick TiN layer beneath a Fe/Al_2O_3 catalyst layer to reduce CNT growth rate by a factor of 2 [104]. Impurities in the TiN tracing from a contaminated evaporation chamber may have further reduced the rate of CNT growth to the extent that only 50 µm of total growth was observed.

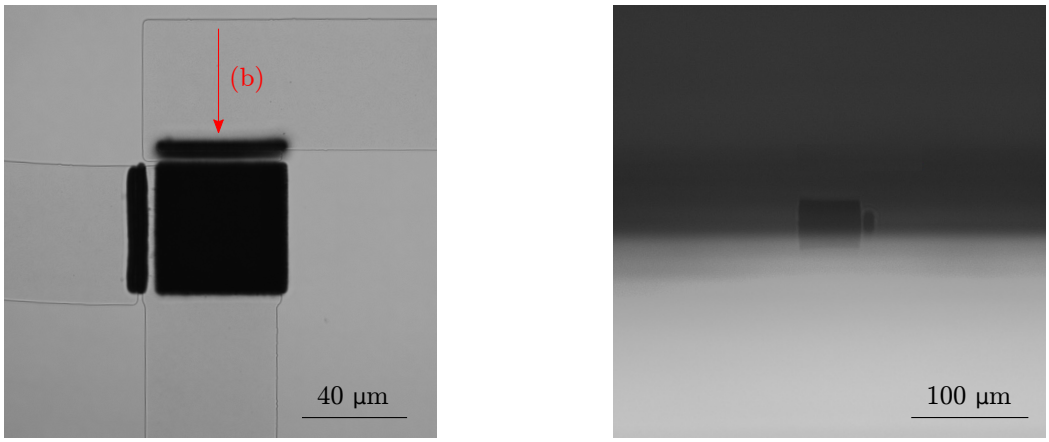

(a) (b)

Figure 4.10: Optical microscope images of the patterned wafer post growth. *(a)*: a top-down view showing the patterned CNT growth. The height of the top sensing element is evident by the blurred effect as the structure rises out of the plane of focus. The red annotation shows the point of view of panel (b). *(b)*: side view to measure the height of the sensing element. This sensing element was estimated to be 50 µm tall.

Another possible explanation for the reduced forest height relates to size of the sensor footprints, and total catalyst area on the patterned dies. With four sensors with footprints only slightly larger than 50 µm by 50 µm, each 10 mm by 10 mm die is very sparsely populated with catalyst ($< 0.003\%$ of the total surface area). Early work by Bronikowsky [131], and later work by Jeong et al. [132], established a relationship between catalyst pattern size, spacing, and CNT forest height. Smaller catalyst regions and larger spacing between catalyst regions produced shorter VACNTF growth. Bronikowsky attributed this to the interaction of the ethylene gas with the iron catalyst particles producing volatile molecular byproducts which assist CNT growth. While our 50 µm by 50 µm sensor footprints are larger than the individual catalyst regions in Bronikowsky's work, the spacing between catalyst regions on our patterned die is significantly larger than anything he tested. It is therefore plausible that there is simply too little catalyst too far apart on our patterned dies for the required evolution of hydrocarbon chemistry of the ethylene feedstock to yield good CNT growth.

Despite the fact that we were unable to synthesize 100 µm tall VACNTF on the patterned wafers, the results shown in Figure 4.10 were adequate to proceed with the planned experiments. Panel (a) shows the geometry of the top sensing element to be true to the intended form. This photograph was taken with the plane of

focus at the surface of the wafer, where a clear gap between the sensing element and the reference element is visible. Turning the focus screw to raise the plane of focus to the top of the sensing element, we were able to verify that the gap between the sensing element and the reference element was maintained. Panel (b) shows a photograph taken from the perspective shown by the red annotation in panel (a). Since the sensor is not located right at the edge of the die, the view of the sensing element is obscured somewhat by the out of focus die edge closer to the microscope objective. Regardless, we were able to measure the height of the sensing element to be around 50 µm.

Chapter 5

Sensor Characterization and Testing

5.1 AFM Experiment

Preliminary testing saw creative use of an atomic force microscope (AFM) with the aim to validate the measurement system and verify sensor response to stimulus. The precision XY stage with visual feedback through the AFM's live digital microscope feed was used to precisely position the silicon die and deflect the CNT sensing element by running it into the stationary AFM probe. Observation of a sensor response would rule out a number of potential problems with the system configuration including short circuits, electromagnetic interference and parasitic capacitance, and generally serve as a proof of concept before engaging in a more technically challenging fluid flow experiment.

5.1.1 Methods

The AFM experiment made use of the capacitance measuring system described in Appendix B. The silicon die with CNT sensors was placed on the carrier PCB and copper tape with conductive adhesive was used to make electrical connection between the conductive pads on the die and the conductive traces on the carrier board. A 33 conductor ribbon cable connects the carrier board to the capacitance measurement PCB. The assembly was secured to the Oxford Instruments Asylum MFP-3D Origin AFM's precision XY stage using double sided tape. The NanoAndMore 160AC probe was landed on top of the CNT forest, raised, moved

away from the sensor, and then lowered again such that the probe tip was vertically positioned below the top of the sensing element and above the surface of the silicon die. This position is illustrated in Figure 5.1, inset (a).

The capacitance measurement board was connected to a computer via USB cable, and recording started with the custom GUI at a sampling frequency of 9.1 Hz. The micrometer adjustment on the AFM stage was used to repeatedly place the probe tip into the four distinct positions described below and illustrated in Figure 5.1.

1. *No contact, off trace*: not in contact with the CNT sensing element and not above one of the conductive TiN traces (panel (a)).
2. *No contact, on trace*: not in contact with the CNT sensing element but above the conductive TiN trace (panel (c)).
3. *Contact*: in contact with the CNT sensing element but not applying enough force to noticeably deflect the VACNT forest (panel (e)).
4. *Deflected*: in contact with the CNT sensing element and applying enough force to cause deflection toward the base pillar (panel (g)).

This series of placements was repeated in reverse order as the probe was backed out, pausing at each position for a period of 15 seconds to allow the signal to settle. The entire sequence was repeated 15 times.

5.1.2 Results and Discussion

Figure 5.2 shows a subset of the data collected during the AFM experiment. The sample data shown corresponds to one complete cycle through the four defined positions from “no contact, off trace", to “deflected" and back. The positions are labeled on the plot. There are clear, abrupt changes in the sensor capacitance signal when the AFM probe is re-positioned. Each time the probe is moved, the signal settles to a steady-state value different from the steady-state value for the prior state.

The capacitance time series data was divided into regions of near constant value between probe position changes. These regions, dubbed averaging windows, were

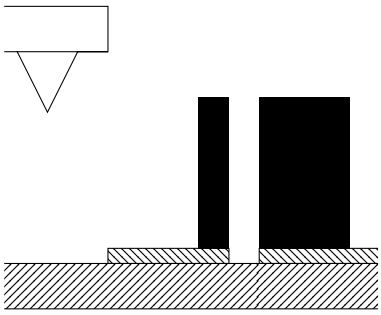

(a) No contact, off trace

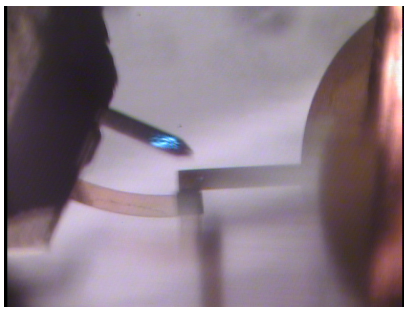

(b)

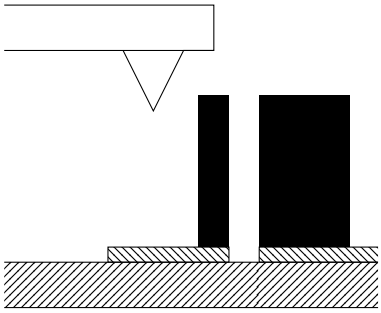

(c) No contact, on trace

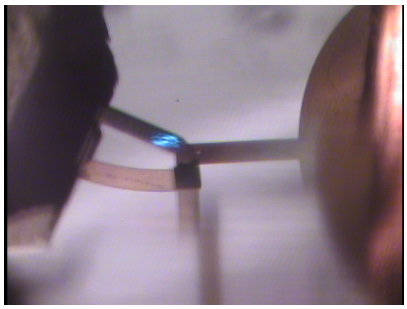

(d)

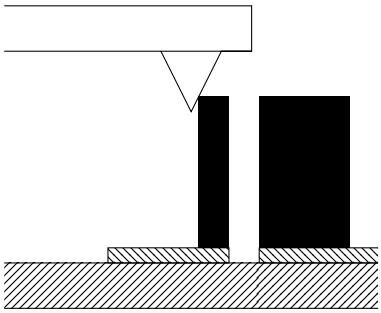

(e) Contact

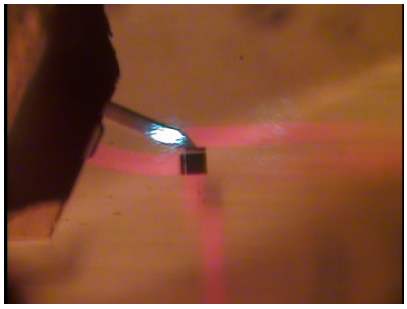

(f)

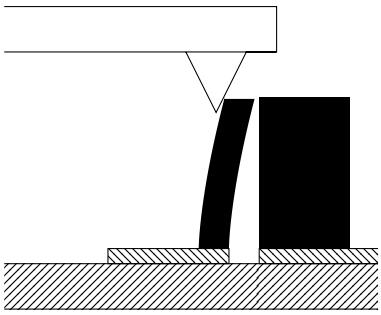

(g) Deflected

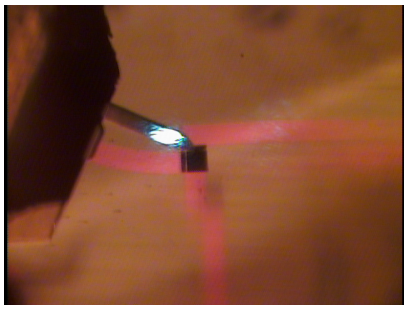

(h)

Figure 5.1: Not-to-scale side-view schematic showing the four distinct positions of the AFM probe during the experiment, with corresponding top-down images from the experiment on the right. The triangular probe tip extends down to contact the CNT sensing element. Beneath the CNT sensing element and the CNT base pillar and on top of the silicon substrate is the TiN conductive tracing.

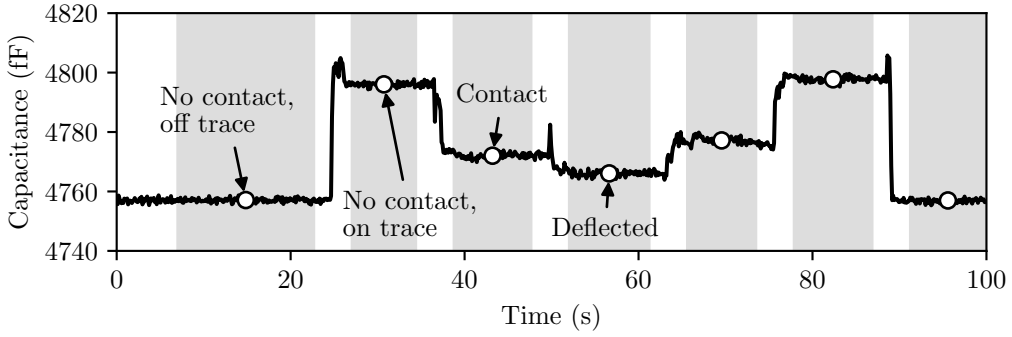

Figure 5.2: Time signal of the the recorded capacitance as the AFM probe was repositioned using the AFM's precision XY stage. The grey regions show the time window over which an average value was collected. The average value in each window is shown with the white marker. The plot has been cropped in the time axis to show one complete cycle through the four probe positions. The following 14 cycles are not shown for clarity.

identified by taking the absolute value of the filtered derivative of the capacitance signal and identifying peaks which correspond to changes in probe position. The averaging windows were defined as the central 60% of the region between the derivative peaks, making them approximately 9 seconds in length. These windows are shown as the grey shaded regions in Figure 5.2.

The signal was averaged over each window, and sets of values collected based on probe position. The complete data set is shown in Table 5.1. The same data are shown as a violin plot in Figure 5.3 to visualize the distribution of the data for the four positions.

Visual inspection of Figure 5.3 indicates clear sensitivity of the device to the AFM probe position. The largest difference in median values occurs between the "no contact, off trace" and "no contact, on trace" states. This change in capacitance may be due to the presence of the probe changing the sensing element's local electromagnetic environment. The proximity of the probe in the "no contact on trace" position could provide an additional body for charge accumulation, increasing the parasitic capacitance compared to when the probe is positioned further from the sensing element. Worth clarifying is that sensitivity to this effect is not desirable, and signal components from similar phenomena in potential future applications will be sources of noise, drift and/or error.

The most important result is the apparent significant difference in signal value be-

Table 5.1: CNT sensor signal in fempto-farads for the four discrete positions tested in the AFM experiment. Note that there are half as many data points for the “no contact, off trace" position and the “deflected" position due to the cyclic nature of the data collection. The final cycle is an exception, with two data points for the “no contact, off trace position" as this was the start and end position in the final cycle.

	No contact, off trace	**No contact, on trace**	**Contact**	**Deflected**
	4757.1	4796.0	4772.0	4766.1
		4797.7	4777.2	
	4757.0	4795.2	4791.3	4778.1
		4800.3	4793.1	
	4757.0	4799.8	4777.6	4758.7
		4799.9	4796.6	
	4756.9	4796.7	4781.2	4758.8
		4801.3	4787.8	
	4757.3	4801.0	4793.0	4758.2
		4795.6	4793.6	
	4757.0	4797.0	4793.4	4762.8
		4806.6	4797.3	
	4757.4	4801.8	4777.3	4758.8
		4795.5	4794.6	
	4757.4	4797.3	4787.5	4763.3
		4797.1	4771.9	
	4757.3	4785.4	4782.7	4758.6
		4799.8	4792.5	
	4757.3	4804.9	4787.0	4764.1
		4796.5	4776.2	
	4757.2	4807.1	4770.3	4760.1
		4806.1	4779.7	
	4757.4	4795.2	4786.9	4762.9
		4797.4	4777.6	
	4757.2	4806.2	4784.3	4765.8
		4795.5	4776.9	
	4757.4	4802.8	4792.8	4757.7
		4806.4	4785.7	
	4757.4	4801.4	4764.7	4757.5
	4757.5	4803.9	4768.7	
Count:	16	30	30	15
Minimum:	4756.9	4785.4	4764.7	4757.5
Median:	4757.3	4799.8	4785.0	4760.1
Maximum:	4757.5	4807.1	4797.3	4778.1
Std. Dev.:	0.2	4.8	9.2	5.3

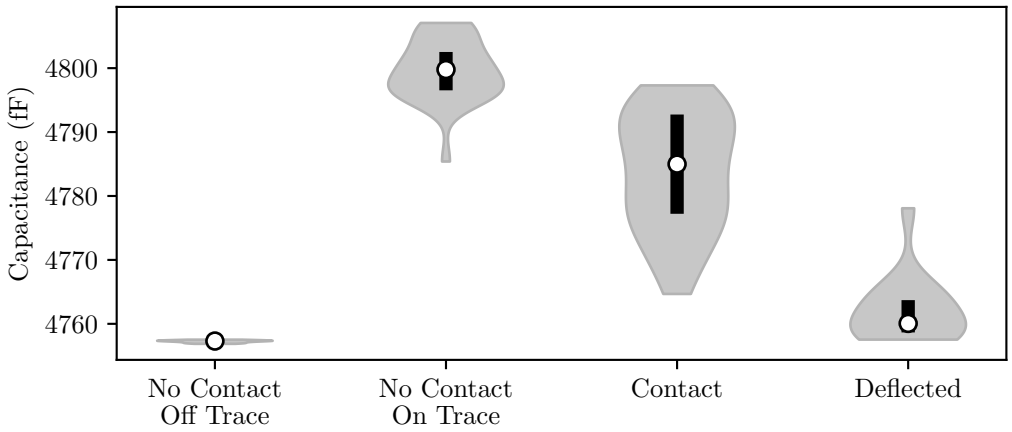

Figure 5.3: Violin plot of the averaged data points aggregated by probe position. The white marker shows the median value and the black bar shows the interquartile range.

tween the contact and deflected states. As we are concerned with the comparison of the mean value of two populations of unequal size with assumed normal distributions and potentially unequal variance, Welch's t-test serves as an appropriate hypothesis test. In this case, the research hypothesis is that the expected value for the measured capacitance differs between the "contact" position and the "deflected" position. The null hypothesis therefore states that the expected values for the measured capacitance for the "contact" position and the "deflected" position are identical. Welch's t-test outputs a t-statistic of 10 and a p-value of $1.2 \cdot 10^{-12}$. We can therefore reject the null hypothesis and say with near certainty ($> 99.9\%$) that the mean capacitance measurement in the "contact" position differs from the mean capacitance measurement in the "deflected" position.

This finding is key, because it clearly indicates that our measurement system is sensitive to the mechanism of interest. In both the "contact" and "deflected" states, the probe is in direct contact with the CNT sensing element, ruling out contact with the probe or a change in position of the probe relative to the CNT sensing element as a potential cause of the change in measured capacitance. It is therefore reasonable to conclude that the measured change is primarily attributable to the deflection of the CNT sensing element and not some secondary factor.

As a final point of discussion pertaining to the results from the AFM experiment, the nature of the relationship was opposite to what was anticipated. The parallel plate model developed in Chapter 4 predicts an increase in capacitance as the

sensing element deflects toward the base element. In contrast, the “deflected" state shows a median value 25 fF less than the “contact" state.

A deeper investigation into the physical mechanisms at play was beyond the scope of the current investigation, so we are left to speculate on the cause of the observed behaviour. One possible explanation relates to the difficulty in precisely manipulating the CNT sensing element with the AFM probe, and the challenge of determining the state of the sensor from the limited resolution visual feedback from the AFM digital microscope feed. If CNTs from the sensing element deflect too far and contact the base pillar, they may act as a path for current leak and decrease the capacitance of the device.

Regardless of the nature of the relationship, the AFM results have established sensitivity of the CNT flow sensor and measurement system to deflection of the CNT sensing element, validating the sensor concept and experimental setup, and clearing the way for the planned flow experiment.

5.2 Flow Channel Experiment

The intention for the flow channel experiment was to determine how the established sensitivity of the CNT device to deflection of its sensing element translates to a flow sensing application where the actuation force is provided by fluid drag. While any non-conductive fluid could be used, air was the clear choice for its ubiquity and inherent experimental simplicity.

5.2.1 Methods

Figure 5.4 shows a simplified schematic of the flow channel experiment. Detailed technical documentation is included in Appendix A. A 1.83 m length of 19.05 mm x 1.59 mm (15.88 mm inside dimensions) extruded square aluminum tubing served as the flow channel. A square cross section was chosen for the flat sides within which the flat silicon samples could be mounted. The size of the cross section was selected to be slightly larger than the 10 mm sample size, but not so large as to make achieving higher flow velocities challenging. The length of the channel was maximized within the constraints of what was readily available from online

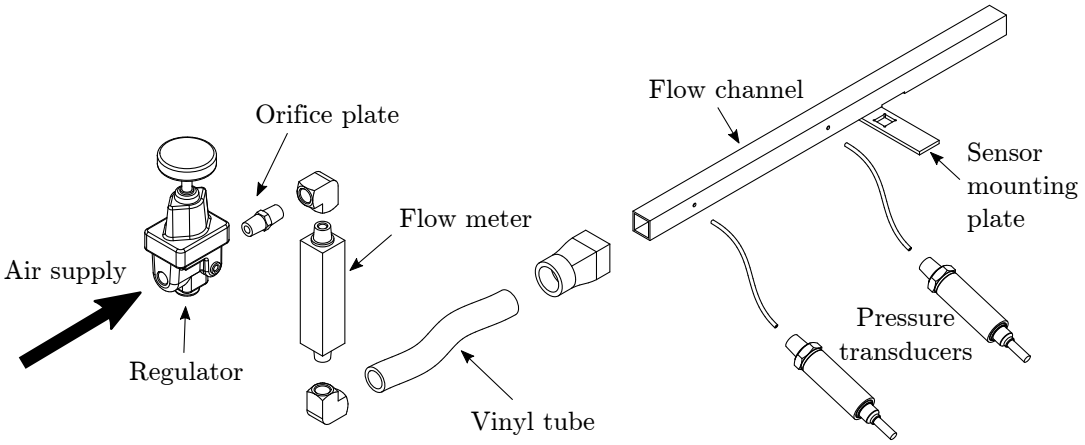

Figure 5.4: Not-to-scale simplified schematic of the flow experiment. Air is supplied from either the lab supply or a blower depending on the desired flow rate. An optional combination of regulator, orifice plate and flow meter (shown upside-down for a more compact illustration) can be included to fine tune the flow. A long section of vinyl tubing allows sufficient time for the flow velocity profile to fully develop. Two pressure taps are included in the square aluminum flow channel upstream of the flow sensor. The flow sensor is fitted to a mounting plate whose top face installs flush with the inside surface of the flow channel.

suppliers, so as to provide a long entry length for the development of a stable flow velocity profile by the time the air passed over the sensor. A pair of Omega PX409 pressure transducers measured the pressure in the channel through 3.18 mm ports drilled in the wall. Air was supplied by either the lab compressed air source or a blower depending on the desired flow rate. A three metre length of 15.88 mm I.D. vinyl tubing served as an extended entry length to ensure fully developed flow by the time the air reached the square tubing [118].

When using the lab compressed air source, a 3-200 kPa regulator was used in conjunction with 3.18 mm and 1.59 mm orifice plates to throttle the flow. An inline 0.4 - 4.0 SCFM flow meter indicated the volumetric flow rate at the orifice plate exit. When the blower was used for high flow tests, the regulator, orifice plate and flow meter were removed to reduce system back pressure and give maximum flow.

Figure 5.5 shows a detailed view of the sensor sub-assembly installed into the bottom of the flow channel. The silicon die hosting the CNT sensors was installed onto the mounting PCB by means of double sided tape, making use of a 3D printed spacer to raise the die flush with the inside of the flow channel. A 3.18 mm by

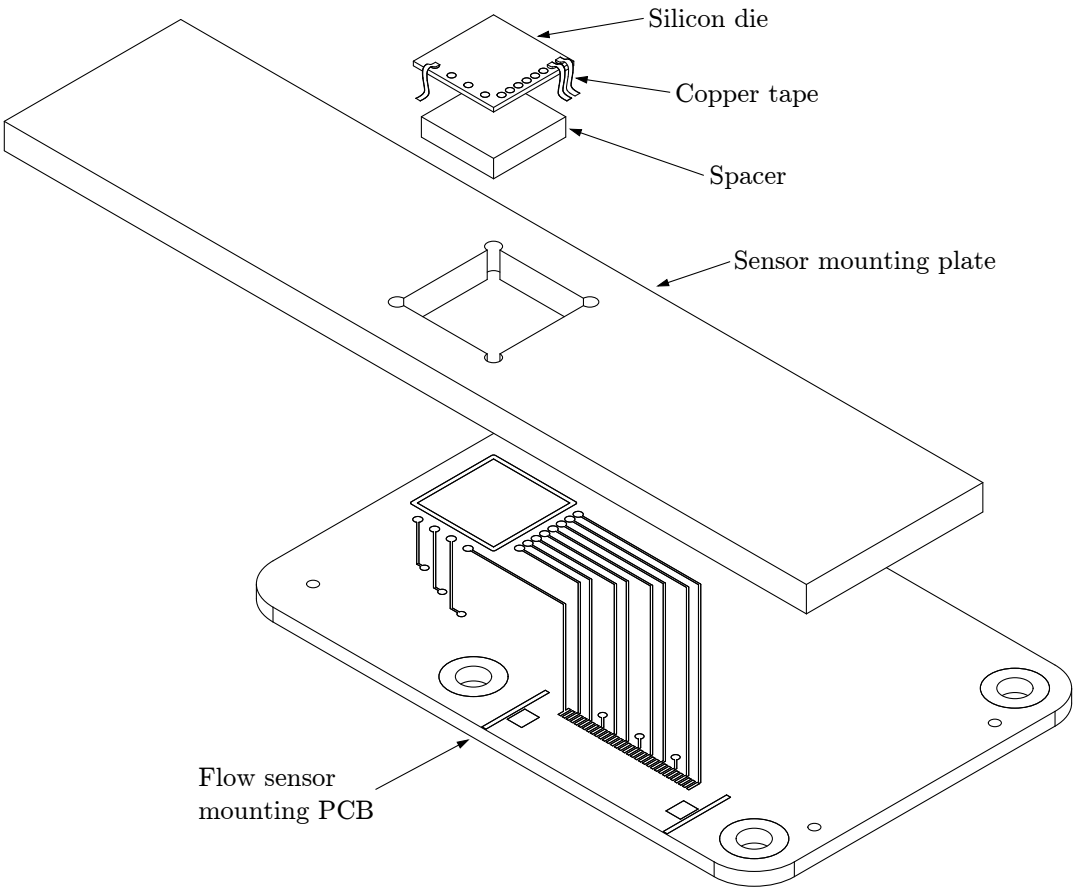

Figure 5.5: Exploded view of the sensor configuration in the flow channel experiment. A carrier PCB has a footprint for the sensor and pads with traces for making electrical connection to the sensors. The sensor mounting plate is secured to the top of the carrier PCB and fits snugly into a machined slot in the bottom of the flow channel. A spacer raises the silicon die up so the top surface sits flush with the top surface of the sensor mounting plate. Not shown is the copper tape which makes electrical contact between the pads on the silicon die and the pads on the carrier PCB.

25.4 mm machined aluminum bar dubbed the sensor mounting plate served to precisely interface with a machined window in the bottom of the flow channel. The flow sensor mounting plate was secured to the mounting PCB using double sided tape, with the silicon die positioned tightly in the corner of the cutout at the vertex opposite the electrical pads. The machined interface between the sensor mounting plate and the flow channel, combined with the 3D printed spacer underneath the silicon die, ensured the silicon surface was reasonably flush with the inside wall of the flow channel. It was important to minimize protruding features which might disrupt the flow.

Once again electrical connection was made by careful application of copper tape with conductive adhesive. The cutout on the sensor mounting plate is oversized to give clearance on the two sides of the die where the electrical pads are located, ensuring the conductive aluminum does not short the connections. Kapton tape was used to cover small gaps between the silicon die and the sensor mounting plate. The mounting PCB connects to the capacitance measurement PCB using the same 33 pin ribbon cable and the capacitance measurement PCB connects to a computer used for control and logging via USB. For all flow experiments, data from the sensor was recorded at a frequency of 9.1 Hz. This was the slowest polling frequency supported by the AD7746 device, and served to increase the signal to noise ratio through time-averaging.

Because the impact of the shear stresses exerted by the fluid flow on the CNT sensors was unknown, the flow experiments started with a low flow rate, and the sensor signal monitored while the flow rate was increased. At each flow rate the flow was cycled on for five minutes and off for five minutes for approximately 100 cycles. A micro-controller was programmed to automate the flow cycling and avoid the need for input every five minutes over the hours-long duration of the tests.

This binary flow strategy provided two distinct advantages for identifying a signal which was anticipated to be on the order of a fempto-farad. First, the long cycle period provided sufficient time for the signal to settle after an abrupt state change. Second, this procedure garnered a large quantity of data for each test that could be averaged to filter out signal noise.

Since the regulator, orifice plates and flow meter generated too much back pressure to be used with the blower at higher flow rates, a different means to control the

Table 5.2: Configuration for the four flow experiments conducted. Included is the mean bulk flow velocity estimated from experimental measurements. The results show experiment configurations selected to yield a relatively linear distribution of bulk flow velocities from 5 m/s up to 87 m/s.

Trial	**Source**	**Restriction** (mm)	**Samples** (count)	**Mean Flow Velocity at Sensor** (m/s)
1	Lab supply	0	90	5.1
2	Lab supply	13	104	29.5
3	Blower	10	65	57.7
4	Blower	13	99	86.7

flow rate was required. For this purpose, inserts of varying height were 3D printed that reduce the flow area in the vicinity of the sensor (Figure 5.7). The inserts include pockets for rare earth magnets. Additional magnets can be positioned externally to clamp the channel wall and hold the inserts firmly in place during even the highest flow rate experiments.

Table 5.2 shows a summary of the experiment configurations for the four flow experiments.

5.2.2 Results and Discussion

Figure 5.6 shows a sample of the raw analogue to digital converter (ADC) output and differential pressure signal from experiment 4. The binary flow state at a given time is evident from the differential pressure signal, with a larger differential pressure corresponding to flow in the channel. With no flow in the channel, the differential pressure signal differs from zero due only to systematic calibration error between the two absolute pressure transducers. The plot of the ADC output shows no immediately apparent corresponding signal from the capacitance measurement board. A more careful inspection of the results is therefore required to determine if a signal from the CNT sensor was detected.

Both the pressure signal and the capacitance signal were chunked into regions of near constant differential pressure between changes in flow states using a modification of the technique from the AFM experiment analysis. In this experiment, the averaging windows were identified by taking the absolute value of the derivative of the differential pressure signal and identifying the peaks which correspond to changes in flow states. The averaging windows were defined as the central 60% of

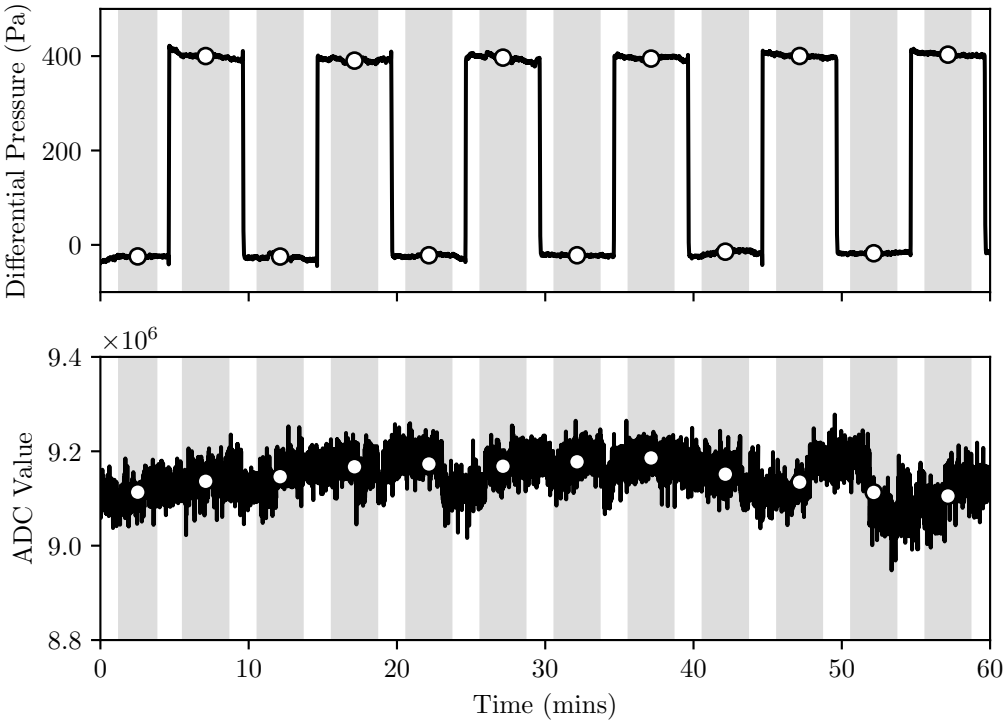

Figure 5.6: *Top*: the black trace shows the differential pressure reading from the two pressure transducers. *Bottom*: the black trace shows the analogue to digital converter output value from reading the capacitance signal. On both plots, the regions in grey represent the averaging window. The average value in each window is represented by the white marker.

the region between these derivative peaks, making them approximately 3 minutes in length.

A mean was taken for both signals across each averaging window, yielding a single differential pressure value and a single ADC value for each of the two binary flow states for each cycle. Subtraction of the flow-off values from the flow-on values for each cycle yields the sensor response for a given upstream pressure drop.

The upstream pressure drop is dependent on the geometry of the flow channel and thus not a useful metric with which to gauge the sensor response. The following analysis presents the bulk flow velocity in the channel at the location of the CNT sensor as a metric helpful for developing an intuitive feel for the experiment flow conditions, and the wall shear stress as a universal metric applicable to different flow environments.

To relate the measured pressure differential to the bulk flow velocity, we start with

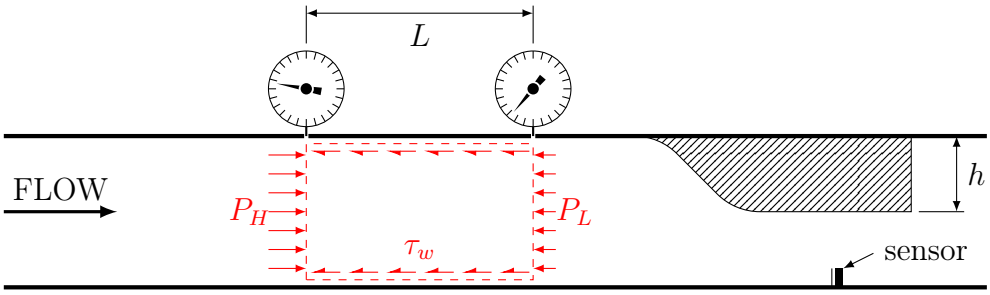

Figure 5.7: Schematic representation of the flow channel experiment. The restriction is removable and restrictions with different heights h are installed to vary the flow area at the sensor. Shown in red is the control volume used to calculate the wall shear stress from the two pressure transducers located upstream from the CNT sensor and separated by a distance L.

general form of the energy equation for one inlet, one outlet, steady, incompressible internal flows.

$$\frac{P_1}{\rho g} + \frac{u_{avg_1}^2}{2g} + z_1 + h_p = \frac{P_2}{\rho g} + \frac{u_{avg_2}^2}{2g} + z_2 + h_t + h_f$$

Figure 5.7 shows a schematic representation of the flow conditions in the channel. Assuming incompressible flow, with a horizontal flow channel and no energy inputs or outputs, the energy equation simplifies to the following.

$$\frac{\Delta P}{\rho g} = h_f \tag{5.1}$$

The major loss expressed as a function of the Darcy friction factor is shown below.

$$h_f = f\frac{Lu_{avg}^2}{2Dg}$$

Substituting this back into Equation 5.1 we arrive at the final form for the energy equation.

$$\frac{\Delta P}{\rho} - f\frac{Lu_{avg}^2}{2D} = 0 \tag{5.2}$$

Based on the experiment modelling, the flow for all four tests was expected to be

turbulent and the Haaland equation (Equation 5.3) was used to find the friction factor. (The analysis which follows confirms that the Reynolds number works out to be greater than 4000 for all four experiments, validating the use of the Haaland equation [118].)

$$f = \left(\frac{1}{-1.8 \log \left(\frac{6.9}{Re_D} + \left(\frac{\epsilon/D}{3.7} \right)^{1.11} \right)} \right)^2 \tag{5.3}$$

Fluid properties for the analysis are for air at standard ambient temperature and pressure. A value of 30 µm was used for the surface roughness ϵ based on typical values of surface roughness for aluminum extrusions.

Substituting Equation 5.3 into Equation 5.2 yields the final relationship between the measured pressure difference and the flow velocity.

$$\frac{\Delta P}{\rho} - \left(\frac{1}{-1.8 \log \left(\frac{6.9\mu}{u_{avg} \rho d_h} + \left(\frac{\epsilon/D}{3.7} \right)^{1.11} \right)} \right)^2 \frac{L u_{avg}^2}{2D} = 0 \tag{5.4}$$

Given a pressure differential ΔP, Equation 5.4 can be solved for the flow velocity using numerical methods. In experiments where no flow restriction was used, the assumption of an incompressible fluid ensures that the calculated flow velocity upstream is the same as the bulk flow velocity at the CNT sensor. In experiments where a restriction was used, the same assumption allows the bulk flow velocity at the sensor to be calculated using the principle of conservation of volume.

$$u_{avg_1} A_1 = u_{avg_2} A_2$$

Calculation of the bulk flow velocity at the sensor from the pressure data for each test yields a linear distribution of bulk velocities across experiments from around 5 m/s to 85 m/s. The top panel of Figure 5.8 shows a violin plot of the differential capacitance response for the four tests, plotted against the bulk flow velocity at the sensor.

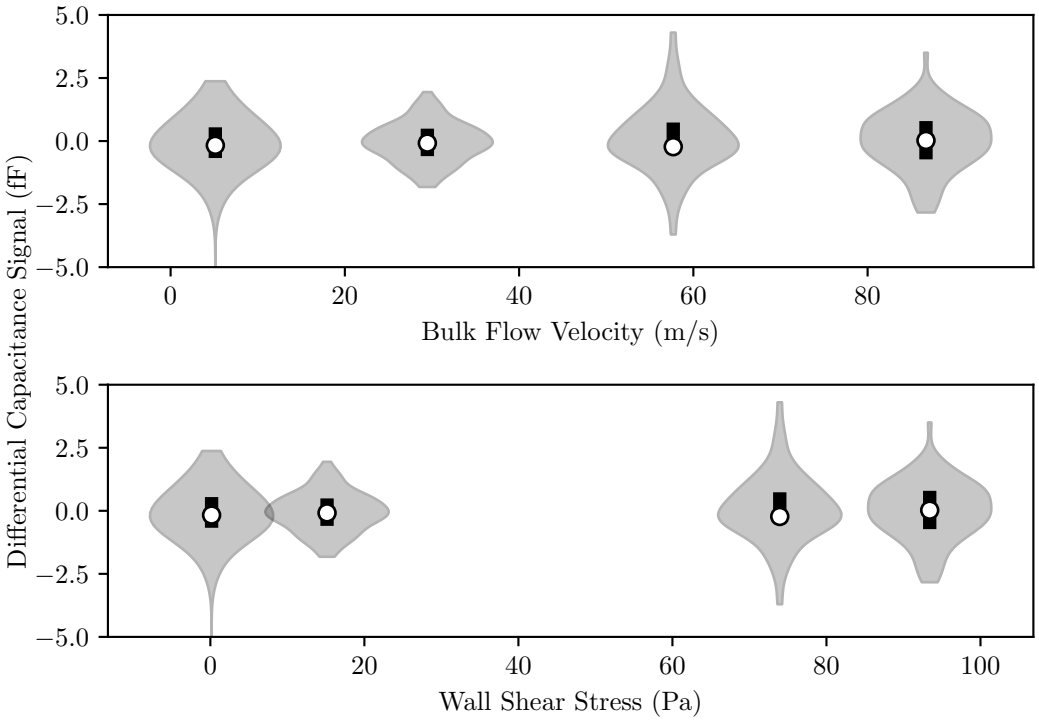

Figure 5.8: Distribution of the differential capacitance signal for each of the four flow experiments. Each distribution represents around 100 data points. The white markers show the median values and the black bars show the interquartile ranges. *Top:* distribution positions corresponding to the average flow velocity for each experiment. *Bottom:* distribution positions corresponding to the average wall shear stress for each experiment.

While the bulk flow velocity is helpful for an intuitive understanding of the flow conditions, it does not easily translate to different flows. It is therefore useful to look at this same data with wall shear stress as the independent variable.

For the experiments without flow restriction, the wall shear stress can be calculated easily using the upstream pressure drop. Figure 5.7 shows a control volume (shown in red) encompassing the entire cross-sectional area of the channel and extending some distance L between the two pressure taps. The pressure differential measured between the two pressure transducers and acting on the cross-sectional area creates a net force toward the right. This force is offset by the wall shear stress acting on the square perimeter of the inside of the flow channel. This relationship is expressed mathematically as

$$(P_H - P_L)A_x = \tau_w A_w$$

where P_H is the upstream pressure, P_L is the downstream pressure, A_x is the cross-sectional area, τ_w is the wall shear stress, and A_w is the wetted area of the control volume. Expressing the areas as a function of the channel geometry and solving for τ_w yields

$$\tau_w = \frac{(P_H - P_L)w}{4L}$$

where w is the internal channel width. Since the flow is assumed to be fully developed and incompressible, the upstream wall shear stress is equal to the wall shear stress at the sensor.

For experiments that used the flow restriction, the upstream pressure gradient is not equal to the pressure gradient at the sensor and the strategy employed above is not appropriate. Instead, we can compare the pressure readings during the the flow-on and flow-off states recorded by the downstream pressure transducer only. Since the pressure during the flow-off state is atmospheric pressure and equal to the pressure at the outlet during the flow-on state, we can use these values to approximate the pressure drop from the second pressure transducer position to the outlet during the flow-on state.

To process the pressure signal from the downstream pressure sensor we use the

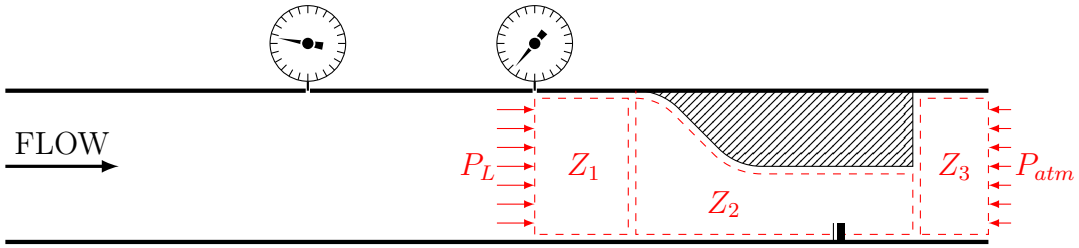

Figure 5.9: Schematic of the flow channel showing the three zones defined for the wall shear stress analysis for the flow experiments using a flow restriction.

same techniques employed for the analysis of the differential pressure signal, locating peaks in the absolute value of the filtered derivative to construct averaging windows, and evaluating the mean value within each window. Subtracting the averaged values from adjacent averaging windows at different flow states gives an approximation of the pressure drop from the downstream pressure transducer to the channel outlet.

The section of the flow channel in question can be divided into the three zones depicted in Figure 5.9. Zone 2 is characterized by a reduced cross section due to the presence of the restriction, while zones 1 and 3 have flow in the full channel cross section.

The aim of the following analysis is to approximate the pressure gradient in zone 2 and use it to find the wall shear stress at the sensor. We begin by making the simplifying assumption that the pressure gradient in the direction of flow is constant across each of the three zones. Since zones 1 and 3 have the full channel cross section, we assume the pressure gradient to be the same as the upstream pressure gradient measured with the two pressure transducers. The pressure drop across zone 2 can then be calculated by subtracting the pressure drop across zones 1 and 3 from the total pressure drop from the downstream pressure transducer to the channel outlet. The pressure gradient in zone 2 is then calculated by dividing the pressure drop by the length of the restriction. Finally, the wall shear stress in zone 2 is calculated using the same method as before, but using the reduced cross sectional area and wetted area of the restricted channel section.

The lower panel of Figure 5.8 shows the same capacitance signal distributions plotted against the estimated wall shear stress at the sensor. It is immediately apparent that there is no significant capacitance signal with varying flow. From the experiment with the lowest wall shear stress to the experiment with the highest wall shear stress, the capacitance signal shows a uniform distribution centred

about zero. Such a clear deviation from the anticipated result deserves a detailed examination of the evidence and a proposed explanation.

Using experiment data, we can re-construct higher fidelity versions of some of the initial fluid and solid mechanics models, substituting previously estimated values for measured ones. Many of the initial estimates for experimental parameters changed significantly in the final experiment. Before the experiment, the height of the CNT sensing element was estimated to be 100 µm. The realities of CNT synthesis prevented such tall VACNT forest growth within the time available, resulting in a final forest height a mere third of what was expected. Since the response was anticipated to be highly sensitive to forest height, it is not surprising that it was more challenging to record sensitivity. To compensate for the reduced sensor height, the flow velocity was increased far beyond what was originally planned. The following analysis combines the techniques used in the pre-experiment modelling with experimental data to see if the lack of a signal can be explained with the previously conceived simplified model.

We start by using the recorded pressure data to re-construct the anticipated boundary layer profile in the vicinity of the CNT flow sensor. In the lower flow velocity experiments, the 50 μm tall CNT flow sensor is entirely contained within the viscous sublayer. The linear velocity profile within the viscous sublayer is defined by

$$u = \tau_w \frac{y}{\mu} \tag{5.5}$$

where τ_w is the wall shear stress and y is the distance from the wall. The thickness of the viscous sublayer is defined as

$$\delta_{sublayer} = \frac{5\mu}{\rho u_*}$$

where u_* is called the friction velocity and is defined as $u_* = \sqrt{\tau_w/\rho}$ [118].

For higher velocity flows, the the viscous sublayer thickness drops below the top of the sensor, necessitating the incorporation of another boundary layer profile. Immediately beyond the viscous sublayer is the buffer layer, characterized by the beginning of the influence of turbulent effects on the flow [118]. The buffer layer

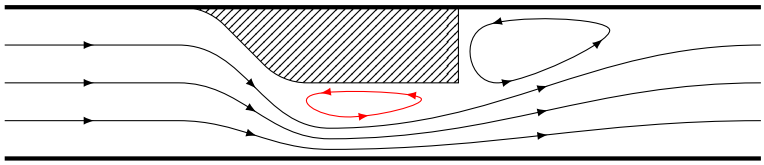

Figure 5.10: A streamline sketch showing how a sharp restriction might cause flow separation in the throat. The flow separation and re-circulation zone in the throat (shown in red) creates an effective flow area smaller than the actual cross-sectional area of the throat.

is somewhat unpredictable and difficult to characterize, thus this analysis satisfies itself with reasonable approximations.

Up to this point, we have focused on using the wall shear stress as an independent variable to characterize sensor response. Therefore a logical method to estimate the velocity profile in the buffer layer might use a relationship like the logarithmic law, an empirical relationship relating wall shear stress to the velocity profile in the overlap layer (and to a certain extent the buffer layer). Unfortunately when the logarithmic law is applied using the previously calculated wall shear stress, the velocity profile grows too large and does not agree with the expected bulk flow velocity calculated from the upstream pressure measurements and the conservation of volume assumption. We speculate that this is due in part to the sharp narrowing of the channel at the restriction causing boundary layer separation and an effective throat area smaller than the geometric throat area. Figure 5.10 illustrates this theory.

Adopting a more basic approach, the power-law velocity profile can can be used in conjunction with the bulk flow velocity to approximate the boundary layer velocity profile beyond the viscous sublayer. While not suitable for estimating the velocity profile in the viscous sublayer due to the function's infinite slope at $r = r_i$, the power-law profile yields suitably accurate results for turbulent internal flow within the rest of the pipe. The power-law velocity profile is defined as

$$\frac{u}{u_{max}} = \left(1 - \frac{r}{r_i}\right)^{\frac{1}{n}} \tag{5.6}$$

where the coefficient n varies with Reynolds number. We don't know the value of u_{max}, however we know the bulk flow velocity u_{avg}. We can manipulate Equation 5.6 to express u_{max} as a function of u_{avg}. We start with the equation for the

volume flow rate

$$\dot{V} = u_{avg} A_x$$

where A_x is the cross sectional area. For a circular pipe, the volume flow rate can be calculated with the following integral

$$\dot{V} = \iint_A u \, dA$$

Since $dA = 2\pi r \, dr$ this works out to

$$\dot{V} = 2\pi \int_{r=0}^{r=r_i} ur \, dr$$

Substituting into the equation for volume flow rate and re-arranging yields

$$u_{avg} = \frac{2\pi}{A_x} \int_{r=0}^{r=r_i} ur \, dr$$

Now solving Equation 5.6 for u and substituting it into the above we get

$$\frac{u_{avg}}{u_{max}} = \frac{2\pi}{A_x} \int_{r=0}^{r=r_i} \left(1 - \frac{r}{r_i}\right)^{\frac{1}{n}} r \, dr$$

Evaluating the integral above yields

$$\frac{u_{avg}}{u_{max}} = \frac{2\pi}{A_x} r_i^2 \frac{n^2}{2n^2 + 3n + 1}$$

Since πr_i^2 is the cross sectional area this simplifies to

$$\frac{u_{avg}}{u_{max}} = 2\frac{n^2}{2n^2 + 3n + 1}$$

For each flow experiment, the Reynolds number may be used to interpolate a

value of n using tabulated empirical data [133]. For example, a Reynolds number of $4 \cdot 10^3$ yields a value of $n = 6$. Substituting $n = 6$ we find that the average velocity to be 79% of the maximum velocity. We can use this to solve for the velocity at a radial location in the pipe using Equation 5.6 manipulated as shown.

$$u = \frac{u_{avg}}{0.79}\left(1 - \frac{r}{r_i}\right)^{\frac{1}{6}}$$

The last step is to express u as a function of the distance from the wall, rather than the radial distance. Since $y = r_i - r$ the above changes to

$$u = \frac{u_{avg}}{0.79}\left(\frac{y}{r_i}\right)^{\frac{1}{6}}$$

This completes the theoretical framework for the post-experiment analysis. For experiments where the viscous layer thickness is greater than the height of the sensing element, the velocity profile is linear and dependent on the wall shear stress (law of the wall profile). For experiments where the sensing element protrudes out of the viscous sublayer, the same linear velocity profile is used up until the point where it crosses the power-law velocity profile, which better approximates the velocity profile in the buffer layer using the bulk flow velocity estimated from upstream pressure measurements.

To illustrate the modelling described above, the top left inset of Figure 5.11 visualizes the boundary layer modelling for the fourth experiment. The hybrid velocity profile is a piece-wise concatenation of the minimum of the law of the wall profile and the power-law profile. This technique generates a velocity profile which agrees with both the calculated average wall shear stress, and the calculated bulk flow velocity.

The remainder of the analysis of the deflection of the sensing element and the change in capacitance follows the same trajectory as the modelling performed prior to the experiment. The results are shown in Table 5.3.

Before concluding the post-experiment modelling, it is worth revisiting the assumptions made for the analysis of the experiment trials using the flow restriction, and examining the unintended consequences those assumptions may have had on the model output. The reason the velocity profile was constructed from both the

Table 5.3: Summary of the post flow experiment modelling results. The values for bulk velocity, Reynolds number and wall shear stress are at the location of the CNT sensor in the flow channel and account for the presence of the flow restriction when relevant.

Trial	**Bulk Vel.** (m/s)	**Re. Num.**	**Wall Shear** (Pa)	**Tip Defl.** (m)	**Cap. Change** (F)
1	5.1	5.03e+03	0.2	1.54e-08	5.68e-18
2	29.5	8.86e+03	15.2	9.90e-07	4.26e-16
3	57.7	3.06e+04	73.9	1.85e-06	9.30e-16
4	86.7	2.61e+04	93.4	3.00e-06	2.01e-15

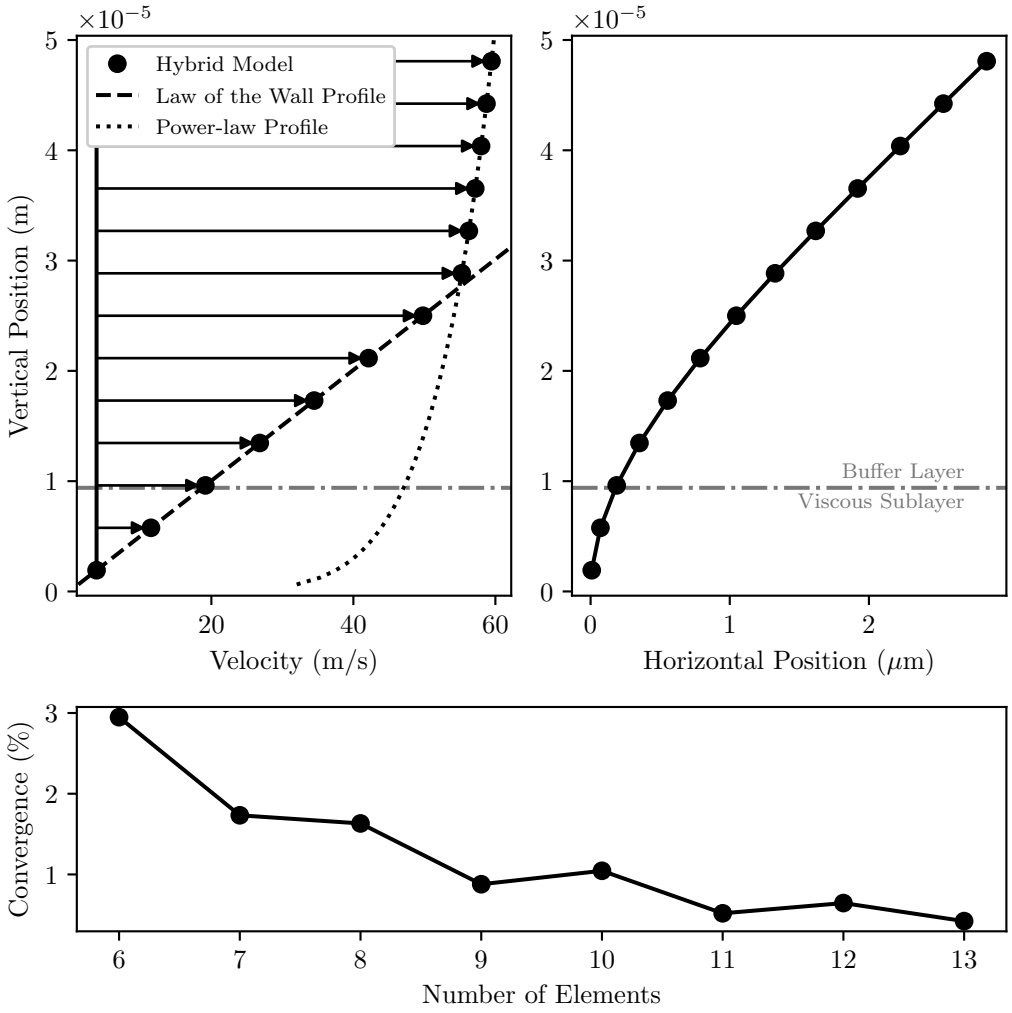

Figure 5.11: Simple finite element model of the CNT sensing element using experimental data. *Top left*: boundary layer velocity profile estimated from the calculated wall shear stress and bulk flow velocity. *Top right*: 13 element finite element model of the sensing element deflection. *Bottom*: Solution convergence showing the percent change in tip deflection as the number of elements was incremented. Convergence limit was set to 0.5%.

estimated bulk flow velocity and the estimated wall shear stress was because the two values did not perfectly align with one another. Detachment of the boundary layer at the leading edge of the flow restriction was posited as the cause. The hope was that incorporating the two into the boundary layer profile calculations would output values within some reasonable middle ground.

One way we might validate this approach is to simulate an experiment where the flow rate in a unobstructed channel is ramped smoothly without the use of any flow restriction. Of course such an experiment is one which we would have liked to conduct in physical form, but which was impractical under the circumstances. Rearranging Equation 5.2 to solve for the expected pressure gradient in the channel yields

$$\frac{\Delta P}{L} = \frac{f \rho V^2}{2D}$$

The wall shear stress can be found by multiplying the pressure gradient by the ratio of the cross sectional area to the wetted area

$$\tau_w = \frac{\Delta P}{L} \frac{w^2}{4w}$$

where w is the internal channel width. The deflection of the sensing element is then calculated from the bulk flow velocity and the wall shear stress using the same technique as before. The results from this simulated experiment plotted against wall shear stress are shown in Figure 5.12, alongside the four discrete data points from the laboratory flow experiment.

Figure 5.12 illustrates two key findings. The first is the large discrepancy between the simulated results and the experimental results at higher values of wall shear stress. This result is consistent with the hypothesis that boundary layer separation around the flow restriction at high flow rates causes a reduced effective cross sectional flow area in the throat. This would result in a smaller hydraulic diameter and larger bulk flow velocity than our conservation of volume calculation provided. Since our velocity profile model worked from the bulk flow velocity and wall shear stress, an under-reported value for the bulk flow velocity would reduce the velocity further from the channel wall, disproportionately reducing the calculated deflection.

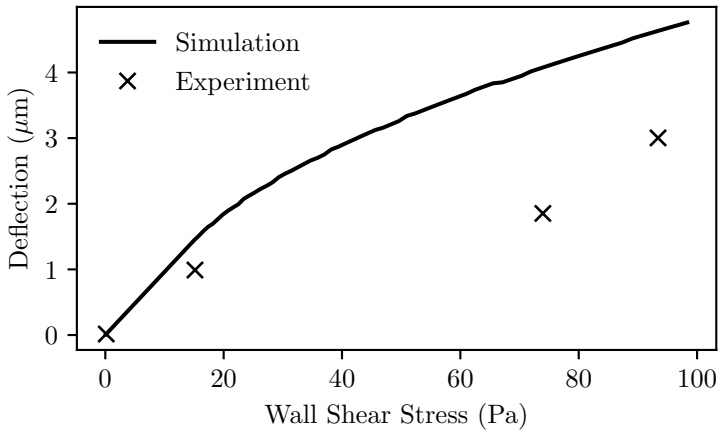

Figure 5.12: CNT sensing element tip deflection versus wall shear stress. The solid trace shows the modelling for a simulated experiment where the flow rate is smoothly ramped in an unobstructed channel. The "×" markers represent the experimental data, where the tip deflection is calculated from the estimated bulk flow velocity at the sensor and the estimated wall shear stress at the sensor calculated from the measured upstream pressure gradient and the measured pressure gradient through the flow restriction respectively.

The second observation from Figure 5.12 is that both the simulation and experimental data predict enough deflection to produce a detectable change in capacitance. The pertinent question is therefore why no discernible capacitance signal was observed. It is unlikely to be a problem within the measurement system, as the results from the AFM experiment proved measurable sensitivity to deflection of the CNT sensing element. The most probable reason for the lack of a discernible signal is therefore that there was far less deflection of the CNT sensing element than predicted by the model.

The modelled deflection is a function of the properties of the CNT pillar, and the forces applied to it. While the simplifying assumptions made during the fluid analysis certainly contribute to error in the drag calculations, the calculated drag is likely to be an underestimate due to the suspected underestimate of the bulk flow velocity in the throat. This leaves the CNT pillar properties as the more likely source of the error in the deflection calculations. Since the Young's modulus of high aspect ratio CNT forests has not been extensively studied, our estimate of the Young's modulus could easily have been incorrect by an order of magnitude or more. A CNT pillar which was 10 times stiffer than predicted would drop the capacitance signal by the same amount and render it indiscernible.

Chapter 6

Conclusion

6.1 Concluding Remarks

Applications for MEMS flow sensors abound in micro- and nano-fluidics, and MEMS flow sensors present unique advantages for the characterization of larger scale flows. The small size and abundance of highly developed bulk synthesis techniques like photolithography make individual MEMS sensors extremely low cost. The small sensor size also enables flow measurement with minimal flow disruption, an advantage for applications where the nature of flow patterns is being studied. Finally, the ability to synthesize tightly spaced sensor arrays provides the opportunity for an unprecedented level of spatial resolution in flow sensing measurements while simultaneously maintaining good temporal resolution.

In this work we first designed and constructed a thermal CVD system for CNT synthesis. We validated the CVD system performance by growing a 500 µm tall VACNTF. We then developed a drag based flow sensor operating by capacitive transduction and constructed from VACNTFs. The fabricated sensor featured a 60 µm by 60 µm footprint, and a height of ∼50 µm. Sensor synthesis is a two-step process, starting with catalyst patterning using photolithography techniques, followed by CVD CNT growth. A measurement system featuring an AD7746 IC was designed and assembled. The sensor and measurement system were validated by physical manipulation of the CNT sensing element using an AFM probe. The system produced a change in output of ∼30 fF as the sensing element was deflected. The AFM experiment was followed by an internal flow experiment in air in a

16 mm by 16 mm square channel. Channel flows from 5 to 85 $\mathrm{m\,s^{-1}}$ (1 to 95 Pa wall shear stress) were tested and found to produce no significant signal. The most likely explanation for the lack of a signal is a significant underestimate of the mechanical properties of the bulk VACNTF material, resulting in little deflection of the sensing element at the flow rates tested.

While less common than thermal and piezo flow sensors, capacitive flow sensors are often more versatile due to their greater temperature independence. CNTs are also beneficial in this regard, featuring a low coefficient of thermal expansion [84]. Previous work fabricating micro-scale capacitive flow sensors has often required many synthesis steps and used complex 3D etching processes. The two-step process used in this work represents a significant simplification of sensor synthesis, revealing an opportunity for highly configurable, low-cost bulk sensor synthesis.

6.2 Future Work

Synthesis of good quality patterned VACNTF structures was one of the biggest challenges in this work. CNT height on the patterned wafers only ever achieved 10 % of what was achieved on blanket wafers, and was only 50 % of the target value. Improvements to the CVD system to refine process control is one avenue to improve results. A redesigned quartz sample holder with a larger diameter rod would likely solve the vibration problem and enable insertion and retraction of the sample during recipe execution. Implementing the proposed solution for communication with the pressure transducer via serial communication baud rate switching would provide a better picture of process conditions and may help explain some of the variability run to run. If new features were to be added to the CVD system, humidity control would be a logical place to start, as CNT growth has been shown to be highly sensitive to reactor humidity [115].

Adjustment of the wafer design and catalyst patterning is a final avenue for improved VACNTF synthesis. The catalyst pattern used in this work was incredibly sparse, covering less than 0.003 % of the die surface. With experimental evidence suggesting optimal pattern densities much higher than this [132], increasing the sensor density, or even including a dense pattern of inactive VACNTF structures may improve sensor CNT growth. While additional VACNTF structures surrounding the sensors may disrupt the boundary layer flow and invalidate the boundary

layer model used in this work, a different model based on wall shear stress might be appropriate.

Another major challenge in this work was anticipating the sensor response with a limited understanding of the material properties of the synthesized VACNTFs. Future work in this area might begin to address this with a more thorough nanoscale characterization of the synthesized CNTs. SEM imaging of the VACNTF structures would not only provide a clearer picture of their microscale shape, but could also reveal CNT areal density, a parameter shown to have a large impact on the effective elastic modulus of VACNTF structures [80]. Direct measurement of the mechanical properties of the synthesized VACNTF structures using lateral force measurements with an AFM would also be informative.

This limited understanding of the sensor properties is also what led to the design of a flow experiment that did not produce adequate flow velocities to generate a sensor response. The blower and the flow restrictions were introduced as stopgap solutions to try to achieve a sensor response. The rushed nature of the implementation is ultimately what led to oversights such as the sharp restriction causing flow separation and the associated difficulties. A future flow experiment could apply the results from a more detailed characterization to design a more refined means for flow control within a relevant range of flow velocities.

Finally, I recommend that future work explores possibilities for alternate means of capacitive transduction. The AD7746 IC used in this work is well suited for measuring the femtofarad scale signals produced by the device. The drawback is that this extreme sensitivity makes the signal highly susceptible to external influence as it travels between the sensor and the IC. Fluctuating electromagnetic fields and small changes in the local electromagnetic environment result in signal noise and significant signal drift, making it difficult to extract the sensor output. During the flow experiments, it was observed that even moving one's hand within a distance of 5 to 10 cm of device wiring produced a change in the signal larger than the anticipated sensor response. There has been recent work to integrate transducers into MEMS sensors, and an interfacing circuit featuring a CMOS ring oscillator has been demonstrated for measuring capacitance signals produced by MEMS devices [49]. Such a device could be employed to generate a more robust signal right on the silicon die and reduce problematic signal noise and drift.

References

[1] Fatemeh Ejeian, Shohreh Azadi, Amir Razmjou, Yasin Orooji, Ajay Kottapalli, Majid Ebrahimi Warkiani, and Mohsen Asadnia. "Design and applications of MEMS flow sensors: A review". In: *Sensors and Actuators, A: Physical* 295 (2019), pp. 483–502. ISSN: 09244247. DOI: 10.1016/j.sna.2019.06.020. URL: https://doi.org/10.1016/j.sna.2019.06.020.

[2] Chwee-Lin Choong, William I. Milne, and Kenneth B. K. Teo. "Review: carbon nanotube for microfluidic lab-on-a-chip application". In: *International Journal of Material Forming* 1.2 (2008), pp. 117–125. ISSN: 1960-6206. DOI: 10.1007/s12289-008-0379-3.

[3] Cairan He, Li Shiah Lim, Muhammad Hamidullah, Pushpapraj Singh, Woo Tae Park, and Han Hua Feng. "Batteryless MEMS flow sensor within prosthetic vascular graft". In: *2011 Defense Science Research Conference and Expo, DSR 2011* (2011). DOI: 10.1109/DSR.2011.6026866.

[4] C. von Campenhausen, I. Riess, and R. Weissert. "Detection of stationary objects by the blind Cave FishAnoptichthys jordani (Characidae)". In: *Journal of comparative physiology* 143.3 (Sept. 1981), pp. 369–374. ISSN: 1432-1351. DOI: 10.1007/BF00611175. URL: https://link.springer.com/article/10.1007/BF00611175.

[5] Jürgen Tautz and Hubert Markl. "Caterpillars detect flying wasps by hairs sensitive to airborne vibration". In: *Behavioral Ecology and Sociobiology* 4.1 (Mar. 1978), pp. 101–110. ISSN: 1432-0762. DOI: 10.1007/BF00302564. URL: https://link.springer.com/article/10.1007/BF00302564.

[6] Susanne Sterbing-D'Angelo, Mohit Chadha, Chen Chiu, Ben Falk, Wei Xian, Janna Barcelo, John M. Zook, and Cynthia F. Moss. "Bat wing sensors support flight control". In: *Proceedings of the National Academy of Sciences of the United States of America* 108.27 (July 2011), pp. 11291–11296.

ISSN: 00278424. DOI: 10.1073/PNAS.1018740108/ASSET/CD5F2E07-A267-4FD5-8860-9B1E4F8FEEFE/ASSETS/GRAPHIC/PNAS.1018740108FIG05.JPEG. URL: https://www.pnas.org/doi/abs/10.1073/pnas.1018740108.

[7] Son D. Nguyen, Igor Paprotny, Paul K. Wright, and Richard M. White. "MEMS capacitive flow sensor for natural gas pipelines". In: *Sensors and Actuators, A: Physical* 231 (2015), pp. 28–34. ISSN: 09244247. DOI: 10.1016/j.sna.2014.10.013. URL: http://dx.doi.org/10.1016/j.sna.2014.10.013.

[8] Andrea De Luca, Claudio Falco, Ethan L.W. Gardner, John D. Coull, and Florin Udrea. "Diode-based CMOS MEMS thermal flow sensors". In: *TRANSDUCERS 2017 - 19th International Conference on Solid-State Sensors, Actuators and Microsystems* (2017), pp. 2211–2214. DOI: 10.1109/TRANSDUCERS.2017.7994516.

[9] D. Bestion, J. Gaviglio, and J. P. Bonnet. "Comparison between constant-current and constant-temperature hot-wire anemometers in high-speed flows". In: *Review of Scientific Instruments* 54.11 (June 1998), p. 1513. ISSN: 0034-6748. DOI: 10.1063/1.1137279. URL: https://aip.scitation.org/doi/abs/10.1063/1.1137279.

[10] B. W. van Oudheusden and A. W. van Herwaarden. "High-sensivity 2-D flow sensor with an etched thermal isolation structure". In: *Sensors and Actuators: A. Physical* 22.1-3 (1990), pp. 425–430. ISSN: 09244247. DOI: 10.1016/0924-4247(89)80007-X.

[11] Vivekananthan Balakrishnan, Toan Dinh, Hoang Phuong Phan, Dzung Viet Dao, and Nam Trung Nguyen. "Highly sensitive 3C-SiC on glass based thermal flow sensor realized using MEMS technology". In: *Sensors and Actuators, A: Physical* 279 (2018), pp. 293–305. ISSN: 09244247. DOI: 10.1016/j.sna.2018.06.025. URL: https://doi.org/10.1016/j.sna.2018.06.025.

[12] M. M. Sadeghi, R. L. Peterson, and K. Najafi. "Air flow sensing using micro-wire-bonded hair-like hot-wire anemometry". In: *Journal of Micromechanics and Microengineering* 23.8 (2013). ISSN: 09601317. DOI: 10.1088/0960-1317/23/8/085017.

[13] Jonathan T.W. Kuo, Lawrence Yu, and Ellis Meng. "Micromachined Thermal Flow Sensors—A Review". In: *Micromachines 2012, Vol. 3, Pages 550-573* 3.3 (July 2012), pp. 550–573. ISSN: 2072-666X. DOI: 10.3390/

MI3030550. URL: https://www.mdpi.com/2072-666X/3/3/550/htm%20https://www.mdpi.com/2072-666X/3/3/550.

[14] Herbert Ernst, Artur Jachimowicz, and Gerald A. Urban. "High resolution flow characterization in Bio-MEMS". In: *Sensors and Actuators A: Physical* 100.1 (Aug. 2002), pp. 54–62. ISSN: 0924-4247. DOI: 10.1016/S0924-4247(02)00187-5.

[15] M. Dijkstra, M. J. de Boer, J. W. Berenschot, T. S.J. Lammerink, R. J. Wiegerink, and M. Elwenspoek. "Miniaturized thermal flow sensor with planar-integrated sensor structures on semicircular surface channels". In: *Sensors and Actuators, A: Physical* 143.1 (2008), pp. 1–6. ISSN: 09244247. DOI: 10.1016/j.sna.2007.12.005.

[16] Wei Xu, Beiqi Lijin, Mingzheng Duan, Xiaoyi Wang, Jeffry Wicaksana, A. Min, Moaaz Ahmed, Ruijin Wang, Nicholas Xuanlai Fang, Amine Bermak, and Yi Kuen Lee. "A wireless dual-mode micro thermal flow sensor system with extended flow range by using CMOS-MEMS process". In: *Proceedings of the IEEE International Conference on Micro Electro Mechanical Systems (MEMS)* (2018), pp. 824–827. ISSN: 10846999. DOI: 10.1109/MEMSYS.2018.8346682.

[17] Moaaz Ahmed, Wei Xu, Saqib Mohamad, Farid Boussaid, Yi Kuen Lee, and Amine Bermak. "Fully Integrated Bidirectional CMOS-MEMS Flow Sensor with Low Power Pulse Operation". In: *IEEE Sensors Journal* 19.9 (2019), pp. 3415–3424. ISSN: 1530437X. DOI: 10.1109/JSEN.2019.2891784.

[18] Zhe Li, Wenhan Chang, Chengchen Gao, and Yilong Hao. "A novel five-wire micro anemometer with 3D directionality for low speed air flow detection and acoustic particle velocity detecting capability". In: *Journal of Micromechanics and Microengineering* 28.4 (2018). ISSN: 13616439. DOI: 10.1088/1361-6439/aaac63.

[19] C. Gerhardy and W. K. Schomburg. "Time of flow sensor with a flow parallel wire". In: *Sensors and Actuators A: Physical* 186 (Oct. 2012), pp. 105–110. ISSN: 0924-4247. DOI: 10.1016/J.SNA.2012.03.010.

[20] Canqian Yang, M. Kümmel, and H. Søeberg. "Dynamic model for a thermal transit-time flow sensor". In: *Chemical Engineering Science* 46.3 (1991), pp. 735–740. ISSN: 00092509. DOI: 10.1016/0009-2509(91)80179-3.

[21] Matthew R. Maschmann, Gregory J. Ehlert, Benjamin T. Dickinson, David M. Phillips, Cody W. Ray, Greg W. Reich, and Jeffery W. Baur. "Bioinspired carbon nanotube fuzzy fiber hair sensor for air-flow detection". In: *Advanced Materials* 26.20 (2014), pp. 3230–3234. ISSN: 15214095. DOI: 10.1002/adma.201305285.

[22] Nannan Chen, Craig Tucker, J.M. Engel, Yingchen Yang, Saunvit Pandya, and Chang Liu. "Design and Characterization of Artificial Haircell Sensor for Flow Sensing With Ultrahigh Velocity and Angular Sensitivity". In: *Journal of Microelectromechanical Systems* 16.5 (Oct. 2007), pp. 999–1014. ISSN: 1057-7157. DOI: 10.1109/JMEMS.2007.902436.

[23] Sergiy Peleshanko, Michael D. Julian, Maryna Ornatska, Michael E. McConney, Melbourne C. LeMieux, Nannan Chen, Craig Tucker, Yingchen Yang, Chang Liu, Joseph A.C. Humphrey, and Vladimir V. Tsukruk. "Hydrogel-encapsulated microfabricated haircells mimicking fish cupula neuromast". In: *Advanced Materials* 19.19 (2007), pp. 2903–2909. ISSN: 09359648. DOI: 10.1002/adma.200701141.

[24] A. G.P. Kottapalli, C. W. Tan, M. Olfatnia, J. M. Miao, G. Barbastathis, and M. Triantafyllou. "A liquid crystal polymer membrane MEMS sensor for flow rate and flow direction sensing applications". In: *Journal of Micromechanics and Microengineering* 21.8 (2011). ISSN: 09601317. DOI: 10.1088/0960-1317/21/8/085006.

[25] Jonathan M. Engel, Jack Chen, Chang Liu, and David Bullen. "Polyurethane rubber all-polymer artificial hair cell sensor". In: *Journal of Microelectromechanical Systems* 15.4 (2006), pp. 729–736. ISSN: 10577157. DOI: 10.1109/JMEMS.2006.879373.

[26] Ajay Giri Prakash Kottapalli, Mohsen Asadnia, Jianmin Miao, and Michael Triantafyllou. "Touch at a distance sensing: Lateral-line inspired MEMS flow sensors". In: *Bioinspiration and Biomimetics* 9.4 (2014). ISSN: 17483190. DOI: 10.1088/1748-3182/9/4/046011.

[27] Takeo Yamada, Yuhei Hayamizu, Yuki Yamamoto, Yoshiki Yomogida, Ali Izadi-Najafabadi, Don N. Futaba, and Kenji Hata. "A stretchable carbon nanotube strain sensor for human-motion detection". In: *Nature Nanotechnology* 6.5 (2011), pp. 296–301. ISSN: 17483395. DOI: 10.1038/nnano.2011.36. URL: http://dx.doi.org/10.1038/nnano.2011.36.

[28] Niklas Svedin, Erik Stemme, and Goran Stemme. "New bi-directional gas-flow sensor based on lift force". In: *International Conference on Solid-State Sensors and Actuators, Proceedings* 1 (1997), pp. 145–148. DOI: 10.1109/sensor.1997.613603.

[29] Y. Su, A. G.R. Evans, A. Brunnschweiler, and G. Ensell. "Characterization of a highly sensitive ultra-thin piezoresistive silicon cantilever probe and its application in gas flow velocity sensing". In: *Journal of Micromechanics and Microengineering* 12.6 (2002), pp. 780–785. ISSN: 09601317. DOI: 10.1088/0960-1317/12/6/309.

[30] Yu Hsiang Wang, Chia Yen Lee, and Che Ming Chiang. "A MEMS-based air flow sensor with a free-standing microcantilever structure". In: *Sensors* 7.10 (2007), pp. 2389–2401. ISSN: 14248220. DOI: 10.3390/s7102389.

[31] Hideotoshi Takahashi, Akihito Nakai, and Isao Shimoyama. "Waterproof airflow sensor for seabird bio-logging using a highly sensitive differential pressure sensor and nano-hole array". In: *Sensors and Actuators A: Physical* 281 (Oct. 2018), pp. 243–249. ISSN: 0924-4247. DOI: 10.1016/J.SNA.2018.08.050.

[32] Bian Tian, Huafeng Li, Ning Yang, Hanyue Liu, and Yulong Zhao. "A MEMS-based flow sensor with membrane cantilever beam array structure". In: *2017 IEEE 12th International Conference on Nano/Micro Engineered and Molecular Systems, NEMS 2017* c (2017), pp. 185–189. DOI: 10.1109/NEMS.2017.8017002.

[33] Steven R Anton and Henry A Sodano. "TOPICAL REVIEW A review of power harvesting using piezoelectric materials (2003 – 2006)". In: 16 (2007), pp. 1–21. DOI: 10.1088/0964-1726/16/3/R01.

[34] Jiyoung Chang, Michael Dommer, Chieh Chang, and Liwei Lin. "Piezoelectric nanofibers for energy scavenging applications". In: *Nano Energy* 1.3 (2012), pp. 356–371. ISSN: 2211-2855. DOI: 10.1016/j.nanoen.2012.02.003. URL: http://dx.doi.org/10.1016/j.nanoen.2012.02.003.

[35] Wooseok Jung, Chunyan Li, Dong Sik Kim, and Chong H. Ahn. "A sensing tube with an integrated piezoelectric flow sensor for liver transplantation". In: *Proceedings of the 31st Annual International Conference of the IEEE Engineering in Medicine and Biology Society: Engineering the Future of Biomedicine, EMBC 2009* (2009), pp. 4469–4472. DOI: 10.1109/IEMBS.2009.5333823.

[36] Tushar Sharma, Sang Soo Je, Brijesh Gill, and John X.J. Zhang. "Patterning piezoelectric thin film PVDF–TrFE based pressure sensor for catheter application". In: *Sensors and Actuators A: Physical* 177 (2012), pp. 87–92. ISSN: 0924-4247. DOI: 10.1016/J.SNA.2011.08.019.

[37] Ajay Giri Prakash Kottapalli, Mohsen Asadnia, K. Domenica Karavitaki, Majid Ebrahimi Warkiani, Jianmin Miao, David P. Corey, and Michael Triantafyllou. "Engineering biomimetic hair bundle sensors for underwater sensing applications". In: *AIP Conference Proceedings* 1965.1 (2018), p. 160003. ISSN: 0094-243X. DOI: 10.1063/1.5038533. URL: https://aip.scitation.org/doi/abs/10.1063/1.5038533.

[38] M. Asadnia, A. G.P. Kottapalli, J. M. Miao, A. B. Randles, A. Sabbagh, P. Kropelnicki, and J. M. Tsai. "High temperature characterization of PZT(0.52/0.48) thin-film pressure sensors". In: *Journal of Micromechanics and Microengineering* 24.1 (2013), p. 015017. ISSN: 0960-1317. DOI: 10.1088/0960-1317/24/1/015017. URL: https://iopscience.iop.org/article/10.1088/0960-1317/24/1/015017%20https://iopscience.iop.org/article/10.1088/0960-1317/24/1/015017/meta.

[39] A G P Kottapalli, M Asadnia, J M Miao, M S Triantafyllou, and Technology Smart. "Harbor Seal Whisker Inspired Flow Sensors to Reduce Vortex-induced Vibrations". In: *28th IEEE International Conference on Micro Electro Mechanical Systems*. Estoril, Portugal, 2015, pp. 889–892. ISBN: 9781479979554. DOI: 10.1109/memsys.2015.7051102.

[40] X. Guo, B. Yang, Q. H. Wang, C. F. Lu, and D. Hu. "Design and Characterization of a Novel Bio-inspired Hair Flow Sensor Based on Resonant Sensing". In: *Journal of Physics: Conference Series* 986.1 (2018), p. 012005. ISSN: 1742-6596. DOI: 10.1088/1742-6596/986/1/012005. URL: https://iopscience.iop.org/article/10.1088/1742-6596/986/1/012005%20https://iopscience.iop.org/article/10.1088/1742-6596/986/1/012005/meta.

[41] Steve T. Cho, Khalil Najafi, Kensall D. Wise, and Clark E. Lowman. "An Ultrasensitive Silicon Pressure-Based Microflow Sensor". In: *IEEE Transactions on Electron Devices* 39.4 (1992), pp. 825–835. ISSN: 15579646. DOI: 10.1109/16.127472.

[42] Craig S. Sander, James W. Knutti, and James D. Meindl. "A Monolithic Capacitive Pressure Sensor with Pulse-Period Output". In: *IEEE Transac-*

tions on Electron Devices 27.5 (1980), pp. 927–930. ISSN: 15579646. DOI: 10.1109/T-ED.1980.19958.

[43] Wen H. Ko, Min Hang Bao, and Yeun Ding Hong. "A High-Sensitivity Integrated-Circuit Capacitive Pressure Transducer". In: *IEEE Transactions on Electron Devices* 29.1 (1982), pp. 48–56. ISSN: 15579646. DOI: 10.1109/T-ED.1982.20657.

[44] Oliver Berberig, Kay Nottmeyer, Jim Mizuno, Yoshitaka Kanai, and Takashi Kobayashi. "The Prandtl micro flow sensor (PMFS): a novel silicon diaphragm capacitive sensor for flow-velocity measurement". In: *Sensors and Actuators A: Physical* 66.1-3 (1998), pp. 93–98. ISSN: 09244247. DOI: 10.1016/S0924-4247(97)01733-0. URL: https://linkinghub.elsevier.com/retrieve/pii/S0924424797017330.

[45] Dean R. Harrison and John Dimeff. "A diode-quad bridge circuit for use with capacitance transducers". In: *Review of Scientific Instruments* 44.10 (1973), pp. 1468–1472. ISSN: 00346748. DOI: 10.1063/1.1685975.

[46] Jaesung Jang and Steven T. Wereley. "A capacitive micro gas flow sensor based on slip flow". In: *Proceedings of the IEEE International Conference on Micro Electro Mechanical Systems (MEMS)* (2004), pp. 540–543. ISSN: 10846999. DOI: 10.1109/mems.2004.1290641.

[47] J. Van Baar, M. Dijkstra, R. Wiegerink, T. Lammerink, R. De Boer, and G. Krijnen. "Arrays of cricket-inspired sensory hairs with capacitive motion detection". In: *Proceedings of the IEEE International Conference on Micro Electro Mechanical Systems (MEMS)* (2005), pp. 646–649. ISSN: 10846999. DOI: 10.1109/memsys.2005.1454012.

[48] J. Haneveld, T. S.J. Lammerink, M. J. De Boer, and R. J. Wiegerink. "Micro coriolis mass flow sensor with integrated capacitive readout". In: *Proceedings of the IEEE International Conference on Micro Electro Mechanical Systems (MEMS)* (2009), pp. 463–466. ISSN: 10846999. DOI: 10.1109/MEMSYS.2009.4805419.

[49] Nicolas André, Bertrand Rue, Gilles Scheen, Denis Flandre, Laurent A. Francis, and Jean Pierre Raskin. "Out-of-plane MEMS-based mechanical airflow sensor co-integrated in SOI CMOS technology". In: *Sensors and Actuators, A: Physical* 206 (2014), pp. 67–74. ISSN: 09244247. DOI: 10.1016/j.sna.2013.11.017. URL: http://dx.doi.org/10.1016/j.sna.2013.11.017.

[50] Л. В Радушкевич and Лукьянович В. М. *О Структуре Углерода, Образующегося При Термическом Разложении Окиси Углерода На Железном Контакте*. 1952.

[51] Marc Monthioux and Vladimir L. Kuznetsov. "Who should be given the credit for the discovery of carbon nanotubes?" In: *Carbon* 44.9 (2006), pp. 1621–1623. ISSN: 00086223. DOI: 10.1016/j.carbon.2006.03.019. URL: www.elsevier.com/locate/carbon%20https://linkinghub.elsevier.com/retrieve/pii/S000862230600162X.

[52] Mats Hillert and Nils Lange. "The structure of graphite filaments". In: *Zeitschrift für Kristallographie - Crystalline Materials* 111.1-6 (1959), pp. 24–34. ISSN: 2196-7105. DOI: 10.1524/ZKRI.1959.111.16.24. URL: https://www.degruyter.com/document/doi/10.1524/zkri.1959.111.16.24/html.

[53] H. P. Boehm. "Carbon from carbon monoxide disproportionation on nickel and iron catalysts: Morphological studies and possible growth mechanisms". In: *Carbon* 11.6 (1973), pp. 583–590. ISSN: 0008-6223. DOI: 10.1016/0008-6223(73)90323-0.

[54] Sumio Iijima. "Helical microtubules of graphitic carbon". In: *Nature* 354.6348 (1991), pp. 56–58. DOI: 10.1038/354056a0.

[55] Sumio Iijima and Toshinari Ichihashi. "Single-shell carbon nanotubes of 1-nm diameter". In: *Nature 1993 363:6430* 363.6430 (1993), pp. 603–605. ISSN: 1476-4687. DOI: 10.1038/363603a0. URL: https://www.nature.com/articles/363603a0.

[56] D. S. Bethune, C. H. Klang, M. S. De Vries, G. Gorman, R. Savoy, J. Vazquez, and R. Beyers. "Cobalt-catalysed growth of carbon nanotubes with single-atomic-layer walls". In: *Nature 1993 363:6430* 363.6430 (1993), pp. 605–607. ISSN: 1476-4687. DOI: 10.1038/363605a0. URL: https://www.nature.com/articles/363605a0.

[57] M. S. Dresselhaus, G. Dresselhaus, J. C. Charlier, and E. Hernández. "Electronic, thermal and mechanical properties of carbon nanotubes". In: *Philosophical Transactions of the Royal Society A: Mathematical, Physical and Engineering Sciences* 362.1823 (2004), pp. 2065–2098. ISSN: 1364503X. DOI: 10.1098/rsta.2004.1430.

[58] Hongjie Dai. "Nanotube Growth and Characterization". In: *Carbon Nanotubes: Synthesis, Structure, Properties, and Applications*. Ed. by Mildred S. Dresselhaus, Gene Dresselhaus, and Phaedon Avouris. Berlin, Heidelberg: Springer Berlin Heidelberg, 2001, pp. 29–53. ISBN: 978-3-540-39947-6. DOI: 10.1007/3-540-39947-X_3. URL: https://doi.org/10.1007/3-540-39947-X_3.

[59] Andreas Thess, Roland Lee, Pavel Nikolaev, Hongjie Dai, Pierre Petit, Jerome Robert, Chunhui Xu, Young Hee Lee, Seong Gon Kim, Andrew G. Rinzler, Daniel T. Colbert, Gustavo E. Scuseria, David Tománek, John E. Fischer, and Richard E. Smalley. "Crystalline Ropes of Metallic Carbon Nanotubes". In: *Science* 273.5274 (1996), pp. 483–487. ISSN: 00368075. DOI: 10.1126/SCIENCE.273.5274.483. URL: https://www.science.org/doi/abs/10.1126/science.273.5274.483.

[60] Hongjie Dai. "Carbon Nanotubes : Synthesis , Integration , and Properties". In: (2002), pp. 1035–1044.

[61] Rufan Zhang, Yingying Zhang, Qiang Zhang, Huanhuan Xie, Weizhong Qian, and Fei Wei. "Growth of Half-Meter Long Carbon Nanotubes Based on Schulz–Flory Distribution". In: *ACS Nano* 7.7 (2013), pp. 6156–6161. ISSN: 1936-0851. DOI: 10.1021/nn401995z. URL: https://pubs.acs.org/doi/10.1021/nn401995z.

[62] Hisashi Sugime, Toshihiro Sato, Rei Nakagawa, Tatsuhiro Hayashi, Yoku Inoue, and Suguru Noda. "Ultra-long carbon nanotube forest via in situ supplements of iron and aluminum vapor sources". In: *Carbon* 172 (2021), pp. 772–780. ISSN: 00086223. DOI: 10.1016/j.carbon.2020.10.066. URL: https://doi.org/10.1016/j.carbon.2020.10.066.

[63] M. M. Shokrieh and R. Rafiee. "A review of the mechanical properties of isolated carbon nanotubes and carbon nanotube composites". In: *Mechanics of Composite Materials* 46.2 (2010), pp. 155–172. ISSN: 0191-5665. DOI: 10.1007/s11029-010-9135-0. URL: http://link.springer.com/10.1007/s11029-010-9135-0.

[64] Jean Paul Salvetat, G. Andrew D. Briggs, Jean Marc Bonard, Revathi R. Bacsa, Andrzej J. Kulik, Thomas Stöckli, Nancy A. Burnham, and László Forró. "Elastic and Shear Moduli of Single-Walled Carbon Nanotube Ropes". In: *Physical Review Letters* 82.5 (1999), p. 944. ISSN: 10797114.

DOI: 10.1103/PhysRevLett.82.944. URL: https://journals.aps.org/prl/abstract/10.1103/PhysRevLett.82.944.

[65] Min Feng Yu, Oleg Lourie, Mark J. Dyer, Katerina Moloni, Thomas F. Kelly, and Rodney S. Ruoff. "Strength and breaking mechanism of multiwalled carbon nanotubes under tensile load". In: *Science* 287.5453 (2000), pp. 637–640. ISSN: 00368075. DOI: 10.1126/SCIENCE.287.5453.637/SUPPL_FILE/1046083C1.GIF. URL: https://www.science.org/doi/abs/10.1126/science.287.5453.637.

[66] Thomas W. Tombler, Chongwu Zhou, Leo Alexseyev, Jing Kong, Hongjie Dai, Lei Liu, C. S. Jayanthi, Meijie Tang, and Shi Yu Wu. "Reversible electromechanical characteristics of carbon nanotubes underlocal-probe manipulation". In: *Nature 2000 405:6788* 405.6788 (2000), pp. 769–772. ISSN: 1476-4687. DOI: 10.1038/35015519. URL: https://www.nature.com/articles/35015519.

[67] Min-Feng Yu, Bradley S. Files, Sivaram Arepalli, and Rodney S. Ruoff. "Tensile Loading of Ropes of Single Wall Carbon Nanotubes and their Mechanical Properties". In: *Physical Review Letters* 84.24 (June 2000), pp. 5552–5555. ISSN: 0031-9007. DOI: 10.1103/PhysRevLett.84.5552. URL: https://journals.aps.org/prl/abstract/10.1103/PhysRevLett.84.5552%20https://link.aps.org/doi/10.1103/PhysRevLett.84.5552.

[68] M. M.J. Treacy, T. W. Ebbesen, and J. M. Gibson. "Exceptionally high Young's modulus observed for individual carbon nanotubes". In: *Nature 1996 381:6584* 381.6584 (1996), pp. 678–680. ISSN: 1476-4687. DOI: 10.1038/381678a0. URL: https://www.nature.com/articles/381678a0.

[69] A. Krishnan, E. Dujardin, T. W. Ebbesen, P. N. Yianilos, and M. M. J. Treacy. "Young's modulus of single-walled nanotubes". In: *Physical Review B* 58.20 (1998), p. 14013. ISSN: 1550235X. DOI: 10.1103/PhysRevB.58.14013. URL: https://journals.aps.org/prb/abstract/10.1103/PhysRevB.58.14013.

[70] O. Lourie, D. M. Cox, and H. D. Wagner. "Buckling and Collapse of Embedded Carbon Nanotubes". In: *Physical Review Letters* 81.8 (1998), p. 1638. ISSN: 10797114. DOI: 10.1103/PhysRevLett.81.1638. URL: https://journals.aps.org/prl/abstract/10.1103/PhysRevLett.81.1638.

[71] Qiang Lu and Baidurya Bhattacharya. "The role of atomistic simulations in probing the small-scale aspects of fracture—a case study on a single-walled carbon nanotube". In: *Engineering Fracture Mechanics* 72.13 (2005), pp. 2037–2071. ISSN: 0013-7944. DOI: 10.1016/J.ENGFRACMECH.2005.01.009.

[72] H. Rafii-Tabar. "Computational modelling of thermo-mechanical and transport properties of carbon nanotubes". In: *Physics Reports* 390.4-5 (2004), pp. 235–452. ISSN: 0370-1573. DOI: 10.1016/J.PHYSREP.2003.10.012.

[73] Zhan Chun Tu and Zhong Can Ou-Yang. "Single-walled and multiwalled carbon nanotubes viewed as elastic tubes with the effective Young's moduli dependent on layer number". In: *Physical Review B* 65.23 (2002), p. 233407. ISSN: 1550235X. DOI: 10.1103/PhysRevB.65.233407. URL: https://journals.aps.org/prb/abstract/10.1103/PhysRevB.65.233407.

[74] Gregory M. Odegard, Thomas S. Gates, Lee M. Nicholson, and Kristopher E. Wise. "Equivalent-continuum modeling of nano-structured materials". In: *Composites Science and Technology* 62.14 (2002), pp. 1869–1880. ISSN: 0266-3538. DOI: 10.1016/S0266-3538(02)00113-6.

[75] Noriaki Hamada, Shin Ichi Sawada, and Atsushi Oshiyama. "New one-dimensional conductors: Graphitic microtubules". In: *Physical Review Letters* 68.10 (1992), p. 1579. ISSN: 00319007. DOI: 10.1103/PhysRevLett.68.1579. URL: https://journals.aps.org/prl/abstract/10.1103/PhysRevLett.68.1579.

[76] Z. K. Tang, L. Zhang, N. Wang, X. X. Zhang, G. H. Wen, G. D. Li, J. N. Wang, C. T. Chan, and P. Sheng. "Superconductivity in 4 Angstrom Single-Walled Carbon Nanotubes". In: *Science* 292.5526 (2001), pp. 2462–2465. ISSN: 00368075. DOI: 10.1126/SCIENCE.1060470. URL: https://www.science.org/doi/abs/10.1126/science.1060470.

[77] Teri Wang Odom, Jin Lin Huang, Philip Kim, and Charles M. Lieber. "Atomic structure and electronic properties of single-walled carbon nanotubes". In: *Nature 1998 391:6662* 391.6662 (1998), pp. 62–64. ISSN: 1476-4687. DOI: 10.1038/34145. URL: https://www.nature.com/articles/34145.

[78] Jeroen W.G. Wildöer, Liesbeth C. Venema, Andrew G. Rinzler, Richard E. Smalley, and Cees Dekker. "Electronic structure of atomically resolved carbon nanotubes". In: *Nature 1998 391:6662* 391.6662 (1998), pp. 59–62.

ISSN: 1476-4687. DOI: 10.1038/34139. URL: https://www.nature.com/articles/34139.

[79] Ben Hsia, Julian Marschewski, Shuang Wang, Jung Bin In, Carlo Carraro, Dimos Poulikakos, Costas P. Grigoropoulos, and Roya Maboudian. "Highly flexible, all solid-state micro-supercapacitors from vertically aligned carbon nanotubes". In: *Nanotechnology* 25.5 (2014). ISSN: 09574484. DOI: 10.1088/0957-4484/25/5/055401.

[80] Anupama Arun, Helene Le Poche, Tonio Idda, Donatello Acquaviva, Montserrat Fernandez Bolanos Badia, Philippe Pantigny, Paul Salet, and Adrian Mihai Ionescu. "Tunable MEMS capacitors using vertical carbon nanotube arrays grown on metal lines". In: *Nanotechnology* 22.2 (2011). ISSN: 09574484. DOI: 10.1088/0957-4484/22/2/025203.

[81] Niklas Olofsson, Johan Ek-Weis, Anders Eriksson, Tonio Idda, and Eleanor E.B. Campbell. "Determination of the effective young's modulus of vertically aligned carbon nanotube arrays: A simple nanotube-based varactor". In: *Nanotechnology* 20.38 (2009). ISSN: 09574484. DOI: 10.1088/0957-4484/20/38/385710.

[82] Chunming Niu, Enid K Sichel, Robert Hoch, David Moy, and Howard Tennent. "High power electrochemical capacitors based on carbon nanotube electrodes electrodes". In: 1480.1997 (2012). DOI: 10.1063/1.118568.

[83] Chunsheng Du, Jeff Yeh, and Ning Pan. "High power density supercapacitors using locally aligned carbon nanotube electrodes". In: 350 (2005). DOI: 10.1088/0957-4484/16/4/003.

[84] Yutaka Maniwa, Ryuji Fujiwara, Hiroshi Kira, Hideki Tou, Hiromichi Kataura, Shinzo Suzuki, Yohji Achiba, Eiji Nishibori, Masaki Takata, Makoto Sakata, Akihiko Fujiwara, and Hiroyoshi Suematsu. "Thermal expansion of single-walled carbon nanotube (SWNT) bundles: X-ray diffraction studies". In: *Physical Review B* 64.24 (2001), p. 241402. ISSN: 0163-1829. DOI: 10.1103/PhysRevB.64.241402. URL: https://journals.aps.org/prb/abstract/10.1103/PhysRevB.64.241402%20https://link.aps.org/doi/10.1103/PhysRevB.64.241402.

[85] Morinobu Endo, Kenji Takeuchi, Susumu Igarashi, Kiyoharu Kobori, Minoru Shiraishi, and Harold W. Kroto. "The production and structure of pyrolytic carbon nanotubes (PCNTs)". In: *Journal of Physics and Chem-*

istry of Solids 54.12 (Dec. 1993), pp. 1841–1848. ISSN: 0022-3697. DOI: 10.1016/0022-3697(93)90297-5.

[86] W. Z. Li, S. S. Xie, L. X. Qian, B. H. Chang, B. S. Zou, W. Y. Zhou, R. A. Zhao, and G. Wang. "Nanotubes Large-Scale Synthesis of Aligned Carbon". In: *Science* 274.December (1996), pp. 1701–1703. DOI: 10.1126/science.274.5293.1701. URL: https://www.science.org/doi/abs/10.1126/science.274.5293.1701.

[87] Cheol Jin Lee, Jeunghee Park, Seung Youl Kang, and Jin Ho Lee. "Growth of well-aligned carbon nanotubes on a large area of Co-Ni co-deposited silicon oxide substrate by thermal chemical vapor deposition". In: *Chemical Physics Letters* 323.5-6 (2000), pp. 554–559. ISSN: 00092614. DOI: 10.1016/S0009-2614(00)00521-2.

[88] R. Andrews, D. Jacques, A. M. Rao, F. Derbyshire, D. Qian, X. Fan, E. C. Dickey, and J. Chen. "Continuous production of aligned carbon nanotubes: A step closer to commercial realization". In: *Chemical Physics Letters* 303.5-6 (1999), pp. 467–474. ISSN: 00092614. DOI: 10.1016/S0009-2614(99)00282-1.

[89] Shoushan Fan, Michael G. Chapline, Nathan R. Franklin, Thomas W. Tombler, Alan M. Cassell, and Hongjie Dai. "Self-oriented regular arrays of carbon nanotubes and their field emission properties". In: *Science* 283.5401 (1999), pp. 512–514. ISSN: 00368075. DOI: 10.1126/science.283.5401.512.

[90] Choon Ming Seah, Siang Piao Chai, and Abdul Rahman Mohamed. "Synthesis of aligned carbon nanotubes". In: *Carbon* 49.14 (2011), pp. 4613–4635. ISSN: 00086223. DOI: 10.1016/j.carbon.2011.06.090. URL: http://dx.doi.org/10.1016/j.carbon.2011.06.090.

[91] Chunxu Pan, Yueli Liu, Feng Cao, Jianbo Wang, and Yaoyao Ren. "Synthesis and growth mechanism of carbon nanotubes and nanofibers from ethanol flames". In: *Micron* 35.6 (Aug. 2004), pp. 461–468. ISSN: 0968-4328. DOI: 10.1016/J.MICRON.2004.01.009.

[92] Zhejuan Zhang, Maziar Shakerzadeh, Beng Kang Tay, Xiaocheng Li, Chongwei Tan, Li Feng Lin, Pingsheng Guo, Tao Feng, and Zhuo Sun. "Fabrication of aligned carbon nanotubes on Cu catalyst by dc plasma-enhanced catalytic decomposition". In: *Applied Surface Science* 255.12 (2009), pp. 6404–6407. ISSN: 01694332. DOI: 10.1016/j.apsusc.2009.02.025.

[93] Bin Zhao, Don N. Futaba, Satoshi Yasuda, Megumi Akoshima, Takeo Yamada, and Kenji Hata. "Exploring advantages of diverse carbon nanotube forests with tailored structures synthesized by supergrowth from engineered catalysts". In: *ACS Nano* 3.1 (2009), pp. 108–114. ISSN: 19360851. DOI: 10.1021/nn800648a.

[94] Ph Mauron, Ch Emmenegger, A. Züttel, Ch Nützenadel, P. Sudan, and L. Schlapbach. "Synthesis of oriented nanotube films by chemical vapor deposition". In: *Carbon* 40.8 (2002), pp. 1339–1344. ISSN: 00086223. DOI: 10.1016/S0008-6223(01)00295-0.

[95] Dongning Yuan, Lei Ding, Haibin Chu, Yiyu Feng, Thomas P. McNicholas, and Jie Liu. "Horizontally aligned single-walled carbon nanotube on quartz from a large variety of metal catalysts". In: *Nano Letters* 8.8 (Aug. 2008), pp. 2576–2579. ISSN: 15306984. DOI: 10.1021/NL801007R/SUPPL_FILE/NL801007R-FILE004.PDF. URL: https://pubs.acs.org/doi/abs/10.1021/nl801007r.

[96] A. V. Melechko, V. I. Merkulov, T. E. McKnight, M. A. Guillorn, K. L. Klein, D. H. Lowndes, and M. L. Simpson. "Vertically aligned carbon nanofibers and related structures: Controlled synthesis and directed assembly". In: *Journal of Applied Physics* 97.4 (Feb. 2005), p. 041301. ISSN: 0021-8979. DOI: 10.1063/1.1857591. URL: https://aip.scitation.org/doi/abs/10.1063/1.1857591.

[97] S. Hofmann, C. Ducati, J. Robertson, and B. Kleinsorge. "Low-temperature growth of carbon nanotubes by plasma-enhanced chemical vapor deposition". In: *Applied Physics Letters* 83.1 (June 2003), p. 135. ISSN: 0003-6951. DOI: 10.1063/1.1589187. URL: https://aip.scitation.org/doi/abs/10.1063/1.1589187.

[98] Kenji Hata, Don N. Futaba, Kohei Mizuno, Tatsunori Namai, Motoo Yumura, and Sumio Iijima. "Water-assisted highly efficient synthesis of impurity-free single-walled carbon nanotubes". In: *Science* 306.5700 (Nov. 2004), pp. 1362–1364. ISSN: 00368075. DOI: 10.1126/science.1104962. URL: http://science.sciencemag.org/.

[99] Takeo Yamada, Alan Maigne, Masako Yudasaka, Kouhei Mizuno, Don N. Futaba, Motoo Yumura, Sumio Iijima, and Kenji Hata. "Revealing the secret of water-assisted carbon nanotube synthesis by microscopic observation

of the interaction of water on the catalysts". In: *Nano Letters* 8.12 (2008), pp. 4288–4292. ISSN: 15306984. DOI: 10.1021/nl801981m.

[100] Don N. Futaba, Kenji Hata, Takeo Yamada, Kohei Mizuno, Motoo Yumura, and Sumio Iijima. "Kinetics of water-assisted single-walled carbon nanotube synthesis revealed by a time-evolution analysis". In: *Physical Review Letters* 95.5 (2005), pp. 1–4. ISSN: 00319007. DOI: 10.1103/PhysRevLett.95.056104.

[101] Hisashi Sugime, Toshihiro Sato, Rei Nakagawa, Cinzia Cepek, and Suguru Noda. "Gd-Enhanced Growth of Multi-Millimeter-Tall Forests of Single-Wall Carbon Nanotubes". In: *ACS Nano* 13.11 (Nov. 2019), pp. 13208–13216. ISSN: 1936-0851. DOI: 10.1021/acsnano.9b06181. URL: https://pubs.acs.org/doi/abs/10.1021/acsnano.9b06181%20https://pubs.acs.org/doi/10.1021/acsnano.9b06181.

[102] Mohab O. Hassan, Alireza Nojeh, and Kenichi Takahata. "A microcantilever of self-suspended carbon nanotube forest for material characterization and sensing applications". In: *Applied Physics Letters* 117.1 (2020). ISSN: 00036951. DOI: 10.1063/5.0012533.

[103] Davor Copic, Sei Jin Park, Sameh Tawfick, Michael De Volder, and A. John Hart. "Fabrication, densification, and replica molding of 3D carbon nanotube microstructures". In: *Journal of Visualized Experiments* 65 (July 2012). ISSN: 1940087X. DOI: 10.3791/3980. URL: /pmc/articles/PMC3471277/?report=abstract%20https://www.ncbi.nlm.nih.gov/pmc/articles/PMC3471277/.

[104] M. De Volder, S. Park, S. Tawfick, and A. J. Hart. "Strain-engineered manufacturing of freeform carbon nanotube microstructures". In: *Nature Communications* 5 (2014), pp. 1–9. ISSN: 20411723. DOI: 10.1038/ncomms5512.

[105] Sanha Kim, Hossein Sojoudi, Hangbo Zhao, Dhanushkodi Mariappan, Gareth H. McKinley, Karen K. Gleason, and A. John Hart. "Ultrathin high-resolution flexographic printing using nanoporous stamps". In: *Science Advances* 2.12 (2016). ISSN: 23752548. DOI: 10.1126/sciadv.1601660.

[106] Sanha Kim, Yijie Jiang, Kiera L.Thompson Towell, Michael S.H. Boutilier, Nigamaa Nayakanti, Changhong Cao, Chunxu Chen, Christine Jacob, Hangbo Zhao, Kevin T. Turner, and A. John Hart. "Soft nanocomposite electroadhesives for digital micro- And nanotransfer printing". In: *Science Advances* 5.10 (2019), pp. 1–9. ISSN: 23752548. DOI: 10.1126/sciadv.aax4790.

[107] Shankar Ghosh, A. K. Sood, and N. Kumar. "Carbon nanotube flow sensors". In: *Science* 299.5609 (2003), pp. 1042–1044. ISSN: 00368075. DOI: 10.1126/science.1079080.

[108] Bertrand Bourlon, Joyce Wong, Csilla Mikó, László Forró, and Marc Bockrath. "A nanoscale probe for fluidic and ionic transport". In: *Nature Nanotechnology* 2.2 (2007), pp. 104–107. ISSN: 17483395. DOI: 10.1038/nnano.2006.211.

[109] B. H. Son, Ji Yong Park, Soonil Lee, and Y. H. Ahn. "Suspended single-walled carbon nanotube fluidic sensors". In: *Nanoscale* 7.37 (2015), pp. 15421–15426. ISSN: 20403372. DOI: 10.1039/c5nr03215f.

[110] Jungwook Choi and Jongbaeg Kim. "Batch-processed carbon nanotube wall as pressure and flow sensor". In: *Nanotechnology* 21.10 (2010). ISSN: 09574484. DOI: 10.1088/0957-4484/21/10/105502.

[111] Thanh Nguyen, Toan Dinh, Van Thanh Dau, Canh Dung Tran, Hoang Phuong Phan, Tuan Khoa Nguyen, Hong Khac Nguyen, Foisal Abu Riduan, Pablo Guzman, Nam Trung Nguyen, and Dzung Viet Dao. "A Wearable, Bending-Insensitive Respiration Sensor Using Highly Oriented Carbon Nanotube Film". In: *IEEE Sensors Journal* 21.6 (2021), pp. 7308–7315. ISSN: 15581748. DOI: 10.1109/JSEN.2020.3048236.

[112] Gregory J. Ehlert, Matthew R. Maschmann, and Jeffery W. Baur. "Electromechanical behavior of aligned carbon nanotube arrays for bio-inspired fluid flow sensors". In: *Active and Passive Smart Structures and Integrated Systems 2011* 7977 (2011), p. 79771C. ISSN: 0277786X. DOI: 10.1117/12.880455.

[113] Matthew R. Maschmann, Ben Dickinson, Gregory J. Ehlert, and Jeffery W. Baur. "Force sensitive carbon nanotube arrays for biologically inspired airflow sensing". In: *Smart Materials and Structures* 21.9 (2012). ISSN: 09641726. DOI: 10.1088/0964-1726/21/9/094024.

[114] Jinjing Li, Mostafa Bedewy, Alvin Orbaek White, Erik S. Polsen, Sameh Tawfick, and A. John Hart. "Highly Consistent Atmospheric Pressure Synthesis of Carbon Nanotube Forests by Mitigation of Moisture Transients". In: *Journal of Physical Chemistry C* 120.20 (2016), pp. 11277–11287. ISSN: 19327455. DOI: 10.1021/acs.jpcc.6b02878.

[115] C. Ryan Oliver, Erik S. Polsen, Eric R. Meshot, Sameh Tawfick, Sei Jin Park, Mostafa Bedewy, and A. John Hart. "Statistical analysis of variation in laboratory growth of carbon nanotube forests and recommendations for improved consistency". In: *ACS Nano* 7.4 (2013), pp. 3565–3580. ISSN: 19360851. DOI: 10.1021/nn400507y.

[116] Frank P Incropera, T. L Bergman, David P DeWitt, Adrienne Lavine, and T. L Bergman. "Appendix A: Thermophysical Properties of Matter". English. In: *Principles of Heat and Mass Transfer*. OCLC: 1156427059. 2014. ISBN: 9788126542734.

[117] Frank P Incropera, T. L Bergman, David P DeWitt, Adrienne Lavine, and T. L Bergman. "Chapter 8: Internal Flow". English. In: *Principles of Heat and Mass Transfer*. OCLC: 1156427059. 2014. ISBN: 9788126542734.

[118] Çengel Yunus A. and John M. Cimbala. "Chapter 8: Flow in Pipes". In: *Fluid Mechanics: Fundamentals and Applications*. McGraw-Hill Higher Education, 2006, pp. 321–343.

[119] Frank P Incropera, T. L Bergman, David P DeWitt, Adrienne Lavine, and T. L Bergman. "Chapter 9: Free Convection". English. In: *Principles of Heat and Mass Transfer*. OCLC: 1156427059. 2014. ISBN: 9788126542734.

[120] J. Keith Nisbett and R G Budynas. *Shigley's Mechanical Engineering Design*. 10th ed. New York: McGraw Hill, 2015.

[121] Thomas Kugelstadt. *The RS-485 Design Guide*. Application Report SLLA272C. Texas Instruments Inc., Feb. 2008.

[122] David J. Griffiths. *Introduction to Electrodynamics*. 4th ed. Pearson Education Inc., 2013.

[123] Heinrich Blasius. *Grenzschichten in Flüssigkeiten mit kleiner Reibung*. Druck von BG Teubner, 1907.

[124] Alva Merle Jones. "Drag Coefficients for Flat Plates, Spheres, and Cylinders Moving at Low Reynolds Numbers in a Viscous Fluid". MA thesis. Oregon State College, 1958.

[125] R Fail, J. A. Lawford, and R. C. W. Eyre. *Low-Speed Experiments on the Wake Characteristics of Flat Plates Normal to an Air Stream*. Tech. rep. London: Aeronautical Research Council, 1957.

[126] Thomas Carmody. "Establishment of the Wake Behind a Disk". In: *Journal of Basic Engineering* 86.4 (Dec. 1964), pp. 869–880. ISSN: 0021-9223. DOI: 10.1115/1.3655980. URL: https://asmedigitalcollection.asme.org/fluidsengineering/article/86/4/869/398998/Establishment-of-the-Wake-Behind-a-Disk.

[127] J Nedić, B Ganapathisubramani, and J C Vassilicos. "Drag and near wake characteristics of flat plates normal to the flow with fractal edge geometries". In: *Fluid Dynamics Research* 45.6 (Dec. 2013), p. 061406. ISSN: 0169-5983. DOI: 10.1088/0169-5983/45/6/061406. URL: https://iopscience.iop.org/article/10.1088/0169-5983/45/6/061406.

[128] Çengel Yunus A. and John M. Cimbala. "Chapter 11: Flow Over Bodies: Drag and Lift". In: *Fluid Mechanics: Fundamentals and Applications*. McGraw-Hill Higher Education, 2006, pp. 561–610.

[129] Kai Liu, Peng Liu, Kaili Jiang, and Shoushan Fan. "Effect of carbon deposits on the reactor wall during the growth of multi-walled carbon nanotube arrays". In: *Carbon* 45.12 (Oct. 2007), pp. 2379–2387. ISSN: 00086223. DOI: 10.1016/J.CARBON.2007.07.008. URL: www.elsevier.com/locate/carbon.

[130] Ebru Devrim Sam, Gokce Kucukayan-Dogu, Beril Baykal, Zeynep Dalkilic, Kuldeep Rana, and Erman Bengu. "Simultaneous growth of self-patterned carbon nanotube forests with dual height scales". In: *Nanoscale* 4.12 (2012), p. 3746. ISSN: 2040-3364. DOI: 10.1039/c2nr30258f. URL: http://xlink.rsc.org/?DOI=c2nr30258f.

[131] Michael J. Bronikowski. "CVD growth of carbon nanotube bundle arrays". In: *Carbon* 44.13 (Nov. 2006), pp. 2822–2832. ISSN: 0008-6223. DOI: 10.1016/J.CARBON.2006.03.022.

[132] Goo Hwan Jeong, Niklas Olofsson, Lena K.L. Falk, and Eleanor E.B. Campbell. "Effect of catalyst pattern geometry on the growth of vertically aligned carbon nanotube arrays". In: *Carbon* 47.3 (Mar. 2009), pp. 696–704. ISSN: 00086223. DOI: 10.1016/J.CARBON.2008.11.003.

[133] C. Kleinstreuer. "Chapter 4: Internal Flow". In: *Modern Fluid Dynamics: Basic Theory and selected applications in macro- and micro-fluidics*. Springer, 2010, pp. 195–252.

Appendix A

List of Supplementary Content

A number of detailed engineering drawings were made during this work. The drawings use different page sizes or are highly detailed and were thus submitted as supplementary content. The filename and description for each supplementary file is provided in Table A.1.

Table A.1: List of supplementary files.

Description	**Filename**
CVD system assembly drawing	CVD_Assembly.pdf
Quartz sample holder	Sample_Holder.pdf
Catalyst photomask	Catalyst_Photomask.pdf
Trace photomask	Trace_Photomask.pdf
Sensor Mounting Plate Part Drawing	Mounting_Plate.pdf
Flow Channel Part Drawing	Flow_Channel.pdf

Appendix B

Capacitive Measurement

B.1 Overview of Capacitive Measurement System Requirements

This appendix outlines the design of two custom PCBs used for capacitive measurements during the AFM and flow experiments. The first custom PCB was responsible for reading the changing capacitance, converting it to a digital signal, and outputting that signal over a USB interface to be read by the computer. We refer to this PCB the measurement PCB. Since this PCB contained the most complex and expensive components, the measurement system was designed such that only one was required.

The second custom PCB was required for interfacing with the CNT flow sensors. Since the measurement PCB was relatively complex and costly, we did not want to glue or tape sensors directly to that board. A set of simple interface boards ensured the measurement board was not damaged and also provided quick and easy switching between devices.

B.2 Measurement PCB

B.2.1 Component Selection

Integrated Circuits

The Analogue Devices 7746 chip was selected to read the small capacitive input from the flow sensors. This integrated circuit (IC) is a high resolution capacitance to digital converter with a full scale capacitance of 4 pF, and an accuracy of 4 fF. The AD7746 chip supports two channels, allowing for simultaneous measurement of each of the two channels on a patterned CNT flow sensor by a single device.

The Teensy 4.0 micro-controller development system was selected to read the I^2C signal from the AD7746 chips. The Teensy 4.0 was chosen for its small size, high performance, wide range of I/O capabilities, and extensive integration with the Arduino development environment. The Teensy is provided with through-holes for mounting headers. Header sockets were installed on the PCB in order to plug the Teensy directly into the board for a secure connection.

The 8-channel TCA9548A I^2C multiplexer was selected in order to communicate with the four AD7746 chips using a single I^2C channel on the Teensy 4.0. The AD7746 chips are produced with static addresses, meaning they must all operate on separate buses. The Teensy 4.0 has only two I^2C interfaces accessible from the top of the board, necessitating the use of a multiplexer. The multiplexer has a configurable address, and supports 3.3 V and 5 V logic.

Passive Components

10 µF capacitors were used for decoupling of the power delivery to all ICs as per the provided data sheets. Status LEDs were added to the I^2C serial clock lines to each of the AD7746 ICs in order to visually indicate activity on the bus to facilitate potential debugging in the future. Green LEDs in the 0603 SMT package size were chosen as they were large enough to be easily seen and de-soldered if necessary, while being small enough to limit their impact on the I^2C serial clock line. The selected LEDs have a forward voltage and current of 3.3 V and 20 mA respectively. Because the idle state of the serial clock line is high, the LED circuit was designed

to sink current. When the serial clock line goes low, the LED turns on.

A 33-pin flexible printed circuit (FPC) cable was selected for connecting the measurement PCB to the interface PCB. With four sensors requiring three electrical connections each, a cable with a minimum of 12 conductors was required. A 33-pin FPC cable was ultimately selected based on availability in the JLCPCB catalogue and to allow for ground conductors to be placed between each of the signal wires to prevent cross-talk between channels.

B.2.2 Board Stack-up

A 1.6 mm thick four-layer board was selected to simplify the routing of signals and to allow for large ground planes to contain the electromagnetic fields from AC signals and prevent potential issues with electromagnetic interference (EMI) later in the experiment. A four-layer stack-up was selected that provides large uninterrupted ground planes on layers 1 and 4 with the signals and power routed on the internal layers (Figure B.1). The selected copper thickness was the default thickness JLCPCB uses.

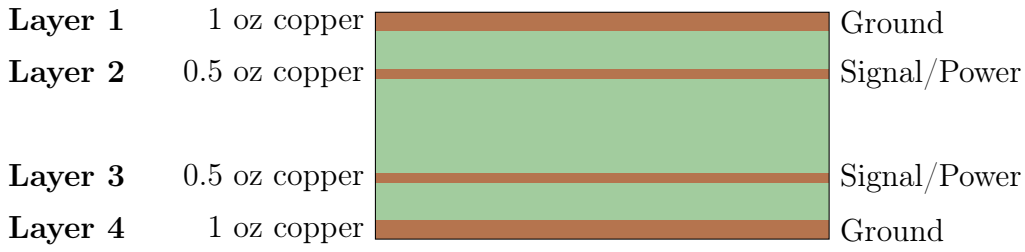

Figure B.1: Measurement board PCB stackup.

B.2.3 Board Layout

The overall board dimensions are 50 mm in width and 100 mm in length. Grounded M4 mounting holes were provided at the four corners of the board. The board is roughly divided into three sections, with the sensitive electronics for capacitance to digital conversion and the power electronics seperated by the Teensy microcontroller in the middle. The AD7746 chips were placed as close to the ribbon connector as possible to keep the traces for the sensitive analogue signals as short as possible and minimize potential EMI problems.

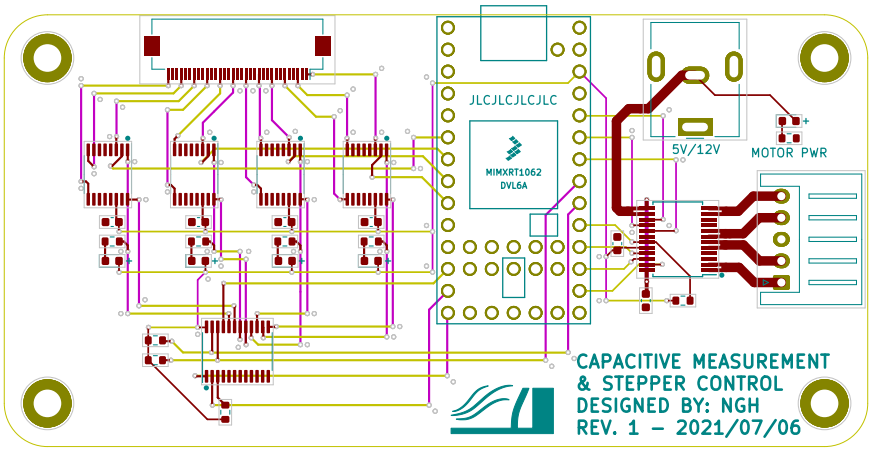

Figure B.2: Detailed layout of the measurement board. Top copper is shown in red, bottom copper is shown in green, and the internal copper layers are shown in purple and yellow.

The measurement PCB was designed to sit upside down, underneath the flow sensor. The ribbon cable connector, microcontroller, and power connector are oriented toward the same edge of the board for easy access. Figure B.2 shows a detailed layout of the board.

B.2.4 Routing

Since this board carries sensitive analogue signals along with digital signals, care was taken to route the signals in such a way as to contain the electromagnetic fields and prevent problems with EMI. It is unlikely that EMI would have caused signal integrity problems with the digital communications over the I^2C interface, however the analogue signals to the flow sensors were very sensitive, and the application of best practices in routing all signals reduced the noise picked up by the AD7746 ICs.

An effort was made to keep all signals on layers 2 and 3 as much as possible to keep the electromagnetic fields within the board. Vias were placed adjacent to signal pins on IC packages in order to route the signals into the board as promptly as possible. Signals were routed in perpendicular directions on layers 2 and 3 to keep routing clean. Where signals transitioned between layers 2 and 3, a ground via was included as close by as possible to allow for the electromagnetic waves to transition from the dielectric between layers 1 and 2, to the dielectric between layers 3 and 4 without spreading out unnecessarily.

B.3 Interface PCB

B.3.1 Board Requirements

The interface PCB provides a means for connecting a set of four CNT flow sensors on a 10 mm by 10 mm silicon die both mechanically and electrically. The PCB is low-profile, with only the ribbon cable connector protruding from the surface, allowing it to sit tightly against the flow channel. Use of a 3D printed spacer raises the silicon die up off the board surface so that it sits flush with the inside wall of the flow channel.

B.3.2 Board Stack-up and Routing

The interface PCB needs very little circuitry and no components apart from a 33-pin FPC connector. As such, a two-layer PCB was used. The FPC connector was placed along the bottom edge of the board. Four grounded M3 mounting holes were included for securing the interface board to a 3D printed bracket that clipped onto the flow channel.

A square region is provided for mounting the flow sensor to the board. The region is outlined on the front silkscreen layer, and the flow direction indicated. Copper pads identical in size and spacing to those provided on the die were positioned just outside the mounting region for connecting to the silicon die using copper tape. These pads included a hole in the solder mask but not the application of solder paste an SMD pad would typically have. A detailed board layout is shown in Figure B.3.

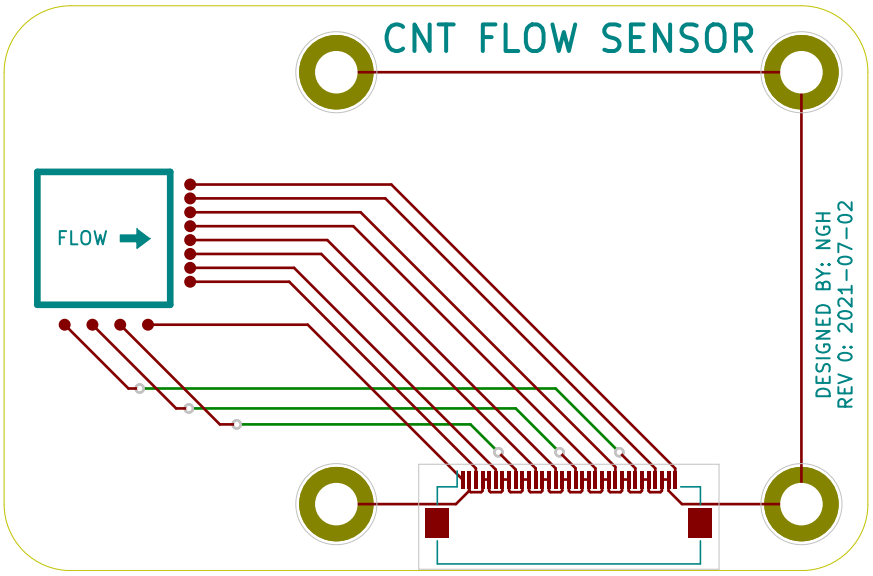

Figure B.3: Interface PCB layout. Top copper is shown in red, bottom copper is shown in green.

Appendix C

CVD System Photographs

Figure C.1: Photograph of the assembled CVD system. The system fits into a fumehood and is controlled from the computer on the right.

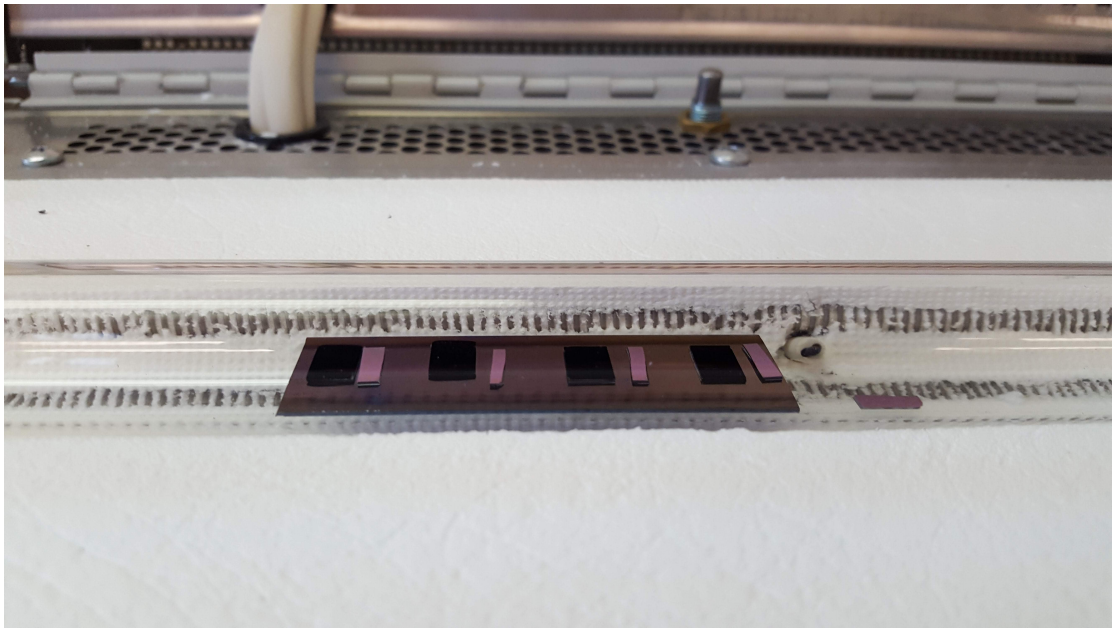

Figure C.2: A picture of samples on the silicon slide in the reactor post-growth. The visibly blackened wafers are the blanket samples that grew a uniform coating of CNTs.

Appendix D

Flow Experiment Photographs

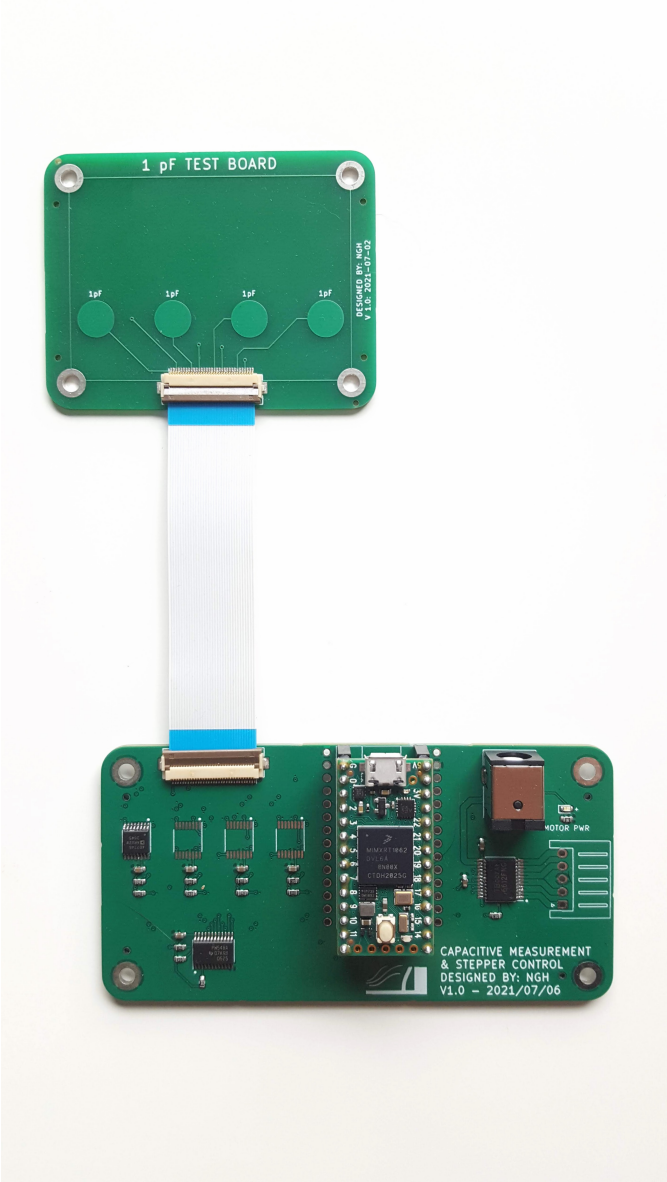

Figure D.1: Photograph of the capacitive measurement system. Connected to the measurement board is a test board with integrated PCB capacitors.

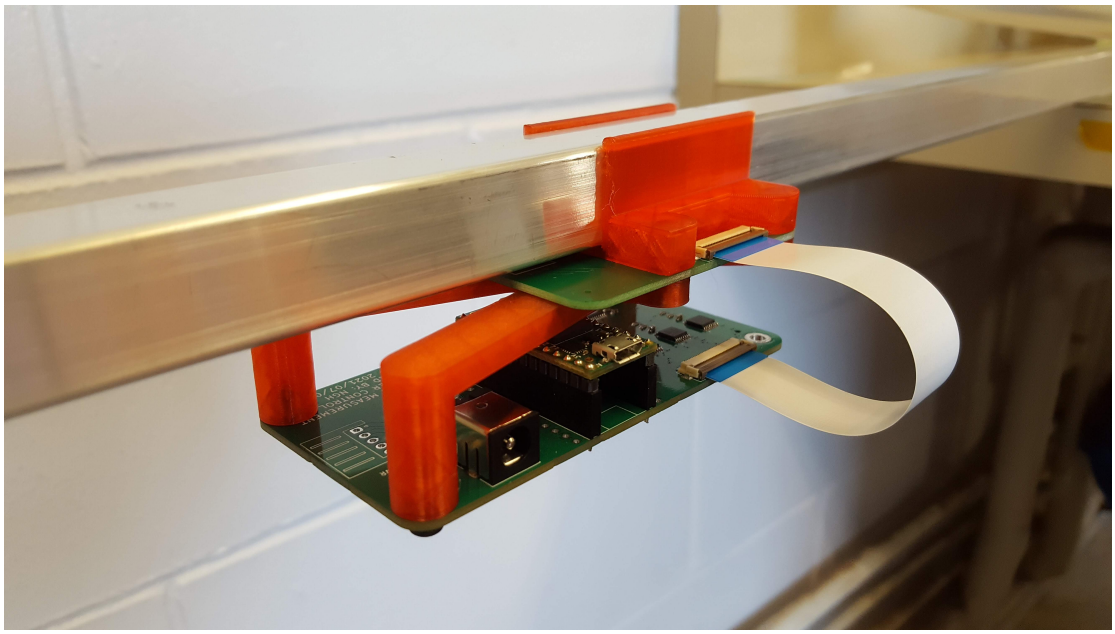

Figure D.2: Photograph of the flow sensor installed in the flow channel and connected to the capactive measurement system.

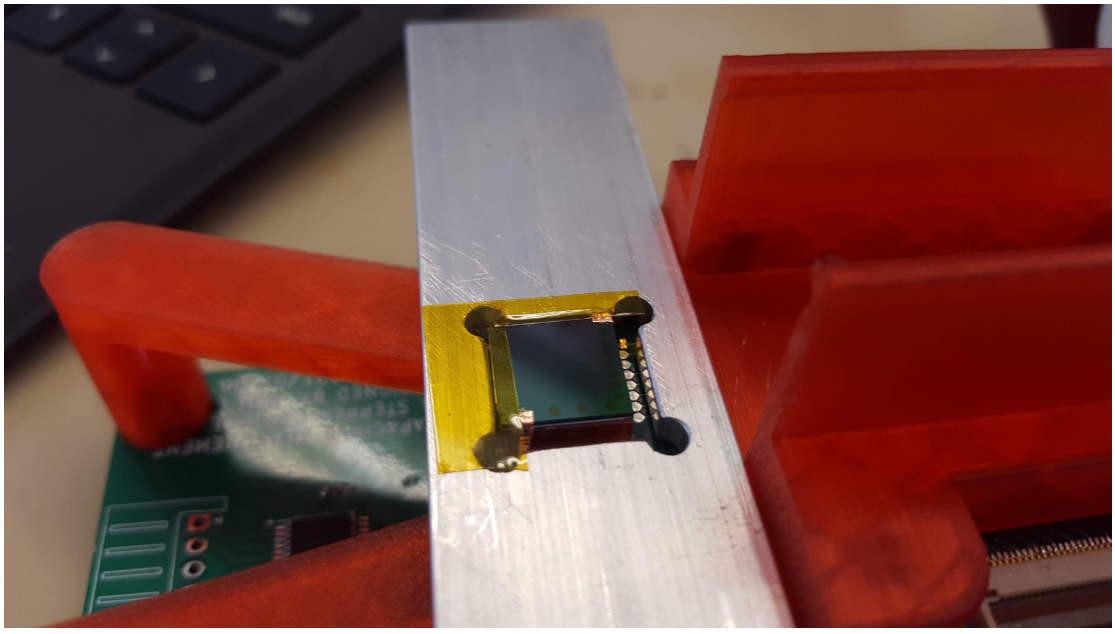

Figure D.3: Photograph of the installation of the sensor into the mounting plate and onto the interface PCB. The copper tape used for electrical connection and the Kapton tape used to seal the gaps are visible.

Curriculum Vitae

Name:	Nathaniel G. Holmes
Post-secondary Education and Degrees:	The University of Western Ontario London, Ontario, Canada 2013-2019 B.E.Sc. The University of Western Ontario London, Ontario, Canada 2019-2022 M.E.Sc.
Honours and Awards:	Donald D.C. McGeachy Award for Materials Engineering 2018 Queen Elizabeth II Graduate Scholarship in Science and Technology 2020-2021
Related Work Experience:	Teaching Assistant The University of Western Ontario 2019-2021 Laboratory Assistant - Summer Coop The University of Western Ontario 2015